Transmission Electron Microscopy of Organic Crystalline Material and Zeolites

James Elliot Cattle

Submitted in accordance with the requirements for the degree of Doctor of Philosophy

The University of Leeds

School of Chemical and Process Engineering

September 2019

Acknowledgements

Abstract

Understanding and controlling the polymorphic form and microstructure of pharmaceutical and zeolitic materials is key to their ongoing application in the food, medical, and chemical industries. Bulk techniques traditionally used to characterise the properties of these materials are limited when it comes to the analysis of the fine atomic structure. In this work electron microscopy has been utilised for the characterisation of a model organic compound (theophylline form II) and a model zeolite (Sn-beta), both of which are highly sensitive to damage when irradiated by a high-energy electron beam (80 – 300 kV).

Transmission electron microscope diffraction pattern analysis was used to determine the lifetime of theophylline form II under a number of controlled microscope and specimen conditions. Values of the characteristic electron fluence for damage varied from 11 ± 5 e$^-$Å^{-2} to 42 ± 5 e$^-$Å^{-2}, with the longest lifetime observed at 300 kV accelerating voltage, at liquid nitrogen specimen temperature, and with a graphene specimen support substrate.

Within this dose budget (*i.e.* the total dose required to locate, align, focus, and record an image of a specimen), atomic lattice information for theophylline form II was obtained by the use of scanning moiré fringes in bright-field scanning transmission electron microscopy. Resolution of the atomic lattice was less readily resolved by bright-field conventional transmission electron microscopy with a direct electron detector. Key to these results is the use of a workflow involving lowering the electron beam flux as much as possible, using 300 kV accelerating voltage (if the sample is >50 – 100 nm thick), and on-specimen focussing using the Ronchigram. Further improvements could be achieved by cooling the sample to liquid nitrogen temperatures, using a conductive specimen support substrate, and using a pixelated

direct electron-counting detector where possible.

A characteristic electron fluence for damage was determined for Sn-beta zeolites of 17000 ± 8000 e$^-$Å^{-2} at 300 kV. Integrated differential phase contrast, scanning transmission electron microscopy revealed the projected atomic positions of the zeolite in the [100]/[010] directions. The use of high-angle annular dark-field scanning transmission electron microscopy in conjunction with integrated differential phase contrast imaging highlighted excess Sn in the form of SnO_2 and identified potential, individual Sn atomic sites. The Sn could be in a number of different tetrahedral Si sites of the beta zeolite structure and image simulation was used to explore likely sites.

Overall, recent improvements to transmission electron microscope characterisation of pharmaceuticals, zeolites, and similarly beam-sensitive inorganics have been discussed and this work demonstrates the potential for bright-field scanning transmission electron microscope techniques in this field.

Table of Contents

List of Figures

as well as the herringbone structure of this crystal. Through typically an ABAB type structure, the marked column is incorrectly oriented. Image from Kobayashi *et al.* (1993).

Fig.2.22: (a) LAADF-STEM image of a thin film of chlorinated copper phthalocyanine. Areas of different contrast are indicative of different film thicknesses and defects. Arrows indicate stacking faults. (b) Schematic of the region shown in (a), highlighting the grain boundaries by dashed-lines, misaligned molecules along the XY grain boundary (blue ellipses) and region C shows the area of stacking faults. Image from Haruta & Kurata (2012).

Fig.2.23: Silver nanoparticles produced at (a) 300 keV and (b) 80 keV. Imaging areas and other beam conditions in both images are identical. Images from Abellán *et al.* (2014).

Fig.2.24: Table comparing four beam sensitive materials by their critical fluences, techniques used to characterise them, and the information obtained from these studies.

Fig.3.1: Schematic of a TEM column showing the path of the electron beam as well as the CLs, OLs, and the EDS and EELS detectors. Image from Bell & Erdman (2012).

Fig.3.2: Calcite nanoparticles imaged with 1 pA probe in the Titan^3 Themis 300. A 1.6 Å calcite (122) d-spacing is resolved. Image from R Hooley, University of Leeds.

Fig.3.3: Flow chart outlining the process of diffraction pattern series acquisition using the FEI Tecnai TF20 electron microscope. The time after initial beam exposure for acquisition of the first diffraction pattern was usually between 10 and 30 seconds.

Fig.3.4: Flow chart detailing the acquisition of iDPC and HAADF STEM micrographs, starting from sample area identification in BF-TEM.

Fig.3.5: Table demonstrating the parameter-space of each of the techniques used for characterisation of zeolite samples.

Fig.4.1: Simulated powder XRD data of the four stable anhydrous forms of theophylline. Data simulated using CrystalMaker software and .cif files. The CCDC references for the .cif files used and the structures they describe are listed in section 3.2.1.

Fig.4.2: XRD patterns of simulated theophylline form II and experimentally acquired patterns for as-bought and recrystallised theophylline.

Fig.4.3: Secondary electron SEM micrographs of (a-b) crystals of as-bought theophylline form II, and (c-d) crystals of recrystallised theophylline form II. Micrographs are from samples mounted on aluminium sample stubs. Images acquired with a 1 kV beam acceleration in deceleration mode.

Fig.4.4: Schematic of a recrystallised theophylline form II crystal observed down the

[100] axis. Based on experimental observations, crystals are typically many tens to hundreds of micrometres long in the [001] and [010] directions, but only up to several hundred nanometres thickness in the [100] direction.

Fig.4.5: Secondary electron SEM micrographs of recrystallised theophylline form II crystals, showing (a) a crystal observed side-on, (b) a crystal region with multiple fractures, and (c) a thin crystal which has conformed to the shape of the aluminium substrate and fractured in multiple areas. Images acquired using a 1 kV beam acceleration in deceleration mode.

Fig.4.6: (a) BF-TEM micrograph of several theophylline crystals, oriented with the (100) plane perpendicular to the beam direction. (b) BF-TEM micrograph of several theophylline crystals, showing bend contours. Micrograph acquired before several minutes of beam exposure, or roughly 60 e$^-$Å^{-2} total fluence. (c) BF-TEM of the same crystals as shown in (b). The bend contours have disappeared after several minutes of beam exposure. Images acquired at 200 kV beam acceleration and at ambient temperatures.

Fig.4.7: BF-TEM micrographs of theophylline form II crystals, showing (a) high densities of bend contours, (b) several large bend contours, and (c) several large, fractured bend contours. The circled areas in (b) and (c) highlight regions of high defect density. Images acquired at 200 kV beam acceleration and at ambient temperatures.

Fig.4.8: (a) An experimentally acquired [100] DP of theophylline form II, in comparison to (b) a simulated theophylline form II [100] DP showing both diffraction spots and systematic absences. The CrystalMaker software was used to produce the simulated pattern, along with the .cif file for theophylline form II, (CCDC reference 878133). The blue arrows in (a) highlight systematic absences with spots barely visible in positions (012), (010), and (014) respectively, while the red arrows highlight two {011} spots with different intensities. Acquired using 200 kV beam acceleration and a 40 µm diameter selected area aperture.

Fig.4.9: A series of [100] DPs taken from the same area of a theophylline form II crystal at different times after the start of beam exposure. Series taken at 300 kV with a 40 µm diameter selected area aperture. The arrows in the first pattern denote two of the {011} spots whose intensities were measured to determine C_F.

Fig.4.10: Graphs of normalised spot intensity versus total electron fluence for a (011) diffraction spot from a [100] DP series of theophylline form II at 300 kV. The C_F is measured off at 1/e of the initial spot intensity, which in these cases is about 40 e$^-$Å^2.

Fig.4.11: Graph of CFs for theophylline form II arranged in order from lowest to highest (least stable to most stable). CFs also shown in the table to the right. Values with units kV refer to electron beam accelerating voltages, while values with units K refer to

produced with a line width of 5 pixels. The peak ratio between the column representing the suspected Sn occupancy and its nearest neighbour are 2.7 for (a), 5.6 for (b), and 1.8 for (c). The ratio between the highest peak and its nearest neighbour for (d) is 1.2.

Fig.6.20: A false-coloured HAADF-STEM micrograph of Si-beta zeolite. Highlighted regions (a) and (b) correspond to the intensity line profiles opposite. Peak ratios between the central two peaks in each profile were 1.1 and 1.05 respectively.

Fig.6.21: A simulated HAADF-STEM micrograph of Si-beta zeolite, observed down the [010] direction. The model has a thickness of 5 unit cells. Also shown is a line profile of the area highlighted in the simulated HAADF-STEM micrograph. Peak ratios are 1.1 and 1.05 respective to the left and right peak pairs.

Fig.6.22: (a – c) Simulated false-colour HAADF-STEM micrographs of Sn-beta zeolite observed down the [010] direction. The Sn occupies the T3 site. The simulations are 2, 5, and 10 unit cells thick respectively. (d – f) Line profiles for each simulation of an area as highlighted in (a). Peak ratios are 3.1, 1.8, and 1.4 respectively.

Fig.6.23: Simulated false-colour HAADF-STEM micrographs of Sn-beta zeolite observed down the [010] direction. These simulations are 2 unit cells thick. In (a) Sn occupies the T-3 at the top of the atomic stack. In (b) Sn occupies a T-1 site roughly ¼ of the way down the atomic stack. The Sn also occupies a T-1 site in (c) though ¾ of the way down the atomic stack in this case. In (d) Sn occupies the T-3 site at the bottom of the atomic stack. Line profiles for each (not shown) were measured from the highlighted areas and the peak ratios measured.

Appendix 5.1: The first 148 lattice spacing measurements for anhydrous theophylline form I and their corresponding Miller indices.

Appendix 5.2: The first 148 lattice spacing measurements for anhydrous theophylline form II and their corresponding Miller indices.

Appendix 5.3: The first 148 lattice spacing measurements for anhydrous theophylline form IV and their corresponding Miller indices.

Appendix 5.4: The first 148 lattice spacings measurements for anhydrous theophylline form IV and their corresponding Miller indices.

Acronyms and Alphabetisations

3D	Three-Dimensional
AFM	Atomic Force Microscopy/Microscope
API	Active Pharmaceutical Ingredient
BF	Bright-Field
BSE	Backscattered Electron
CCD	Charge-Couple Device
C_F	Critical Fluence
CL	Condenser Lens
CMOS	Complimentary Metal-Oxide-Semiconductor
CTEM	Conventional Transmission Electron Microscopy/Microscope
DED	Direct Electron Detection
DFT	Density Functional Theory
DLR	Dose-Limited Resolution
DP	Diffraction Pattern
DPC	Differential Phase Contrast
ED	Electron Diffraction
EDS	Electron Dispersive Spectroscopy
EDX	Energy Dispersive X-ray
EELS	Electron Energy Loss Spectroscopy
EM	Electron Microscopy/Microscope
EXAFS	Extended X-ray Absorption Fine Structure
FFT	Fast Fourier Transform
FWHM	Full-Width Half-Maximum
HAADF	High-Angle Annular Dark-Field
HR	High-Resolution
HS	Hydrothermal Synthesis
iDPC	Integrated Differential Phase Contrast
NA	Numerical Aperture
NMR	Nuclear Magnetic Resonance
OL	Objective Lens
SAXS	Small-Angle X-ray Scattering
SE	Secondary Electron
SEM	Scanning Electron Microscopy/Microscope

SMF	Scanning Moiré Fringe
SNR	Signal-to-Noise Ratio
SPM	Scanning Probe Microscopy/Microscope
SSIE	Solid-State Ion Exchange
STEM	Scanning Transmission Electron Microscopy/Microscope
STM	Scanning Tunnelling Microscopy/Microscope
TEM	Transmission Electron Microscopy/Microscope
WPO	Weak Phase Object
XRD	X-ray Diffraction
LAADF	Low-Angle Annular Dark-Field

Publications

First Author Publications

Cattle, J, S'ari, M, Hondow, N, Abellán, P, Brown, AP, Brydson, RMD, *Journal of Physics: Conference Series*, **644**, 'Transmission electron microscopy of a model crystalline organic, theophylline', 2015, 012030

Cattle, J, S'ari, M, Wilkinson, N, Hondow, N, Brown, A, Brydson, R, *Microscopy and Microanalysis*, **21**, 'Prospects for High-resolution Analytical Electron Microscopy of Organic Crystalline Particles', 2015, 397-398

Cattle, J, S'ari, M, Abellán, P, Ramasse, Q, Hondow, N, Brown, A, Brydson, R, *European Microscopy Congress 2016: Proceedings*, 'Quantitative analysis of a model pharmaceutical materials, theophylline, by transmission electron microscopy', 2016, 752-753

Collaborative Publications

The outputs of the above work have been used in the work referenced here:

S'ari, M, Cattle, J, Hondow, N, Blade, H, Cosgrove, S, Brydson, RM, Brown, AP, *Journal of Physics: Conference Series*, **644**, 'Analysis of electron beam damage of crystalline pharmaceutical materials by transmission electron microscopy', 2015, 1-5

S'ari, M, Cattle, J, Brown, A, Brydson, R, Hondow, N, Blade, H, Cosgrove, S, Hughes, L, *European Microscopy Congress 2016: Proceedings*, 'Transmission Electron Microscopy of a Poorly Soluble Drug, Felodipine', 2016, 720-721

S'ari, M, Cattle, J, Hondow, N, Brydson, R, Brown, A, *Micron*, **120**, 'Low dose scanning transmission electron microscopy of organic crystal scanning moiré fringes', 2019, 1-9

Chapter 1 – Introduction

1.1 – Background

Organic crystalline materials are utilised in a vast number of industrial scale applications, from food to pharmaceuticals. In all cases, understanding and control of the polymorphic form and microstructure of the material is key. Bulk techniques traditionally used to characterise these properties are limited when it comes to the analysis of the fine structure of organics. While high-resolution techniques like electron microscopy (EM) can be utilised for such characterisation, organic materials are infamous for their high sensitivity to damage when irradiated by an electron beam (Jones, 1976). Strategies exist to mitigate the effects of this damage, although they tend to be applied to isolated examples. There is a need for consistent workflows and methods for the analysis of beam-sensitive organic specimens by EM.

Zeolites are highly porous inorganic materials prized and widely used for their catalytic activity, which is activated upon inclusion of a variety of metal dopants into the structure. Changes in dopants and synthesis techniques result in final products with different catalytic efficiencies related to the atomic and crystal structures. As such, understanding of these structures and the mechanics associated with their formation is key to the production of an ideal catalyst for a given reaction. EM techniques are ideally positioned to provide the characterisation needed for these samples, but a major challenge is the sensitivity of zeolite samples to the electron beam (Treacy & Newsam, 1987). While generally more stable than most organic specimens, this sensitivity is a major hinderance to the characterisation of the pristine atomic structure of zeolites.

This thesis addresses some of the challenges for robust analysis of beam-sensitive

materials by EM, by looking at a model organic compound and a model zeolite.

1.2 – Aims and Objectives

The aim of this thesis is to demonstrate that EM techniques can be applied to characterise the structure of organic compounds and samples of similar sensitivity to alteration under electron irradiation.

In this work, two materials, an organic crystalline material (theophylline form II) and an inorganic crystalline material (Sn-beta zeolite), will be used as model materials to explore low-dose EM. This then gives three specific research objectives:

1: Measurement of lifetime of theophylline form II under high-energy electron irradiation plus identification of operating and specimen conditions that may extend lifetimes.

2: Determination of appropriate EM methods to image the atomic lattice of theophylline form II.

3: Determination of appropriate EM methods for the characterisation of Sn-beta zeolite structure and chemistry.

1.3 – Experimental Approaches

All research approaches are described in detail in Chapter 3. A brief overview is given in this section to highlight the novelty of the approaches used in this thesis.

Scanning electron microscopy (SEM) and energy dispersive X-ray (EDX) spectroscopy are used initially to confirm the polymorphic form of theophylline as the anhydrous form II. Low-dose transmission electron microscope (TEM) electron

diffraction (ED) is then used to measure the lifetime of theophylline form II under electron beam irradiation. Specimen and microscope conditions are changed to extend the lifetime, identify beneficial conditions, and develop a methodology for consistent imaging of similar materials in future.

Based on what was learned from the above experimentation, various TEM imaging methods are then used to attempt high-resolution imaging of the crystal lattice of theophylline form II. A new direct electron detection (DED) camera is used with low-dose bright-field (BF) TEM and compared to the results of low-dose BF scanning transmission electron microscopy (STEM), both by direct lattice imaging by BF-STEM imaging and by observation of scanning moiré fringes (SMFs).

STEM methods are also used for the characterisation of the atomic structure of Si and Sn-beta zeolites, with EDX also being used to confirm the elemental content of both. STEM integrated differential phase contrast (iDPC) imaging is used to acquire atomic resolution electron micrographs of the zeolites with enhanced phase contrast. High-angle annular dark-field (HAADF) STEM is used to attempt to pinpoint the location of individual Sn dopant atoms within the structure of the two Sn-beta zeolite samples synthesised by different methods. Multislice (Bloch-wave) simulation of HAADF-STEM micrographs are produced as a point of comparison to the experimental results.

1.4 – Thesis Outline

This thesis consists of seven chapters. This first chapter is followed by a chapter which gives an overview of the literature surrounding electron microscopy of electron beam sensitive materials and related analytical techniques.

Chapter 3 contains a description of all experimental and analytical methods used.

This is followed by three results chapters, with chapter 4 covering the initial characterisation and critical fluence determination of theophylline form II. Chapter 5 reports on the attempts to resolve the lattice structure of theophylline by several low-dose electron microscope techniques. Chapter 6 covers the high-resolution characterisation of a model zeolite and attempts to locate individual metal dopant atoms within the porous structure.

Finally, the results from chapters 4 to 6 are summarised in chapter 7 and discussed in relation to future work.

Chapter 2 – Literature Review

2.1 – Crystalline Organics

2.1.1 – Structures and Properties

Whilst inorganic crystals are typified by a continuous lattice of covalently or ionically bound atoms or ions, organic crystals are formed from numerous molecules (typically carbon-based) which are held together in a continuous lattice by weaker intermolecular forces, namely van der Waals forces, hydrogen bonds, dipole interactions *etc*. As a result, organic crystals are more susceptible to damage than their inorganic counterparts, have lower melting points, and are relatively easily dissolved by numerous solvents, though specimen stability varies heavily based on the compound under analysis.

There are many areas of application of organic crystals, each of which requires precise control over the exact crystalline structure and morphology of the products. In foods, many items rely on organic crystals to impart a required flavour and/or texture. For example, in chocolates, the crystallisation of cocoa butter and fats must be controlled to produce cocoa butter crystals of uniform size and fat crystals of the correct polymorph (Schenk *et al.*, 2004). With both of these conditions met, chocolate of a smooth consistency which melts at body temperature will be formed, rather than chocolate that crumbles and melts at much lower temperatures.

Polymorphic forms of organic crystals are of critical importance to the pharmaceutical industry. Different polymorphs of a material have a number of different properties. Most notable, when considering pharmaceuticals, are changes that occur in crystal morphology and lattice energies. Changes in these properties in turn change the solubility of the material, which is a key factor in determining bioavailability.

Sometimes, polymorph changes also result in stereoisomer changes, which can heavily reduce the effectiveness of a drug (since biological systems generally only interact with one stereoisomer of a molecule) (Craven & Lenki, 2012). Being able to predict the uptake of a pharmaceutical into the human body is a key part of applying the correct dose of a drug. As such, all stages of large-scale pharmaceutical development must be designed in such a way as to produce and retain the correct polymorph.

Many organic materials form numerous crystalline polymorphs depending on the conditions used to produce them. Because of the weak intermolecular bonding, the energies of these polymorphs are often very similar, meaning that phase transformations between polymorphic variants can readily occur in solution or even in the solid state. Physical properties of a material can vary depending on the polymorph of the material produced, with solubility, melting temperature, crystal morphology and purity all potentially being affected (Vippagunta *et al.*, 2001). For example, theophylline is a pharmaceutical material known to display at least six polymorphs, one hydrated, the rest anhydrous (Eddleston *et al.*, 2013; Seton *et al.*, 2010). Figure 2.1 shows scanning electron microscope (SEM) images of the crystal morphologies of two different polymorphs of theophylline. There are clear differences in crystal morphology between these two forms. Additionally, many physical properties between polymorphs will alter. The melting point and enthalpy of fusion values for form I of theophylline are 273.4 ± 1.0 °C and 26.4 ± 0.3 kJ/mol respectively. The same values for form II of theophylline are 269.1 ± 0.4 °C and 28.2 ± 1.1 kJ/mol respectively (Suzuki *et al.*, 1989). Though these differences may seem slight, such changes may be significant enough to disrupt a pharmaceutical product's activity entirely.
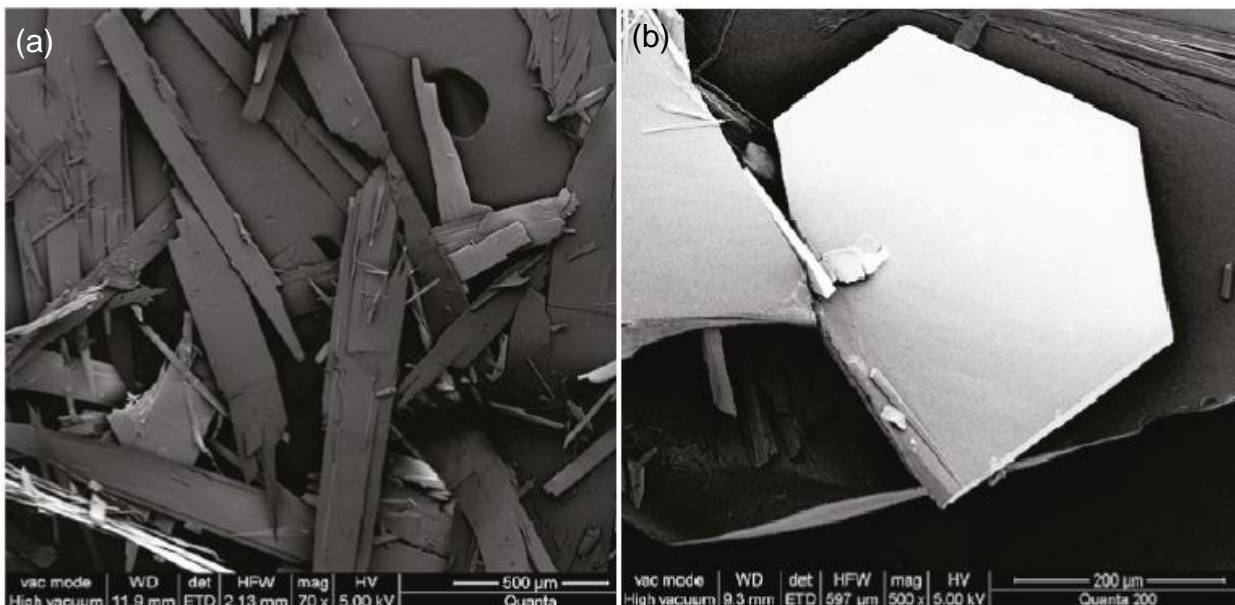
Fig.2.1: SEM micrographs of crystals of (a) form M, the hydrated polymorph of theophylline, and (b) form IV, one of theophylline's anhydrous polymorphs. Where the hydrated polymorph forms long, flat, needle-like crystals, form IV forms large, polyhedral, plate-like crystals. Images from Seton *et al.* (2010).

Given that the energetic differences between organic polymorphs of a material tend to be small, conversion between two polymorphs can occur quickly or over longer periods of time, which can be troublesome for analysis of new materials, as predicting a material's behaviour is not straightforward. In several cases, it becomes difficult to isolate specific polymorphs of a material before it suddenly and irreversibly converts to a different form. There are many reported cases of a polymorph of a material being isolated, before it is lost and unable to be re-isolated for many years to come. Such occurrences have come to be known as 'disappearing polymorph' events (Bučar *et al.*, 2015).

Additionally, there are many cases of crystal formations resulting from the mixture and crystallisation of two or more different organic materials. Such structures are known as cocrystals and display properties that differ from any of their constituent

compounds. Cocrystals can also display polymorphism, adding further variety to the number of possible structures that organic crystals can display (Aitipamula *et al.*, 2009). Theophylline can form numerous cocrystals with materials such as caffeine, citric acid, oxalic acid, maleic acid, and glutaric acid (Schultheiss & Newman, 2009). A study of a hydrated theophylline tablet system mixed with citric acid (as a pH stabiliser) found that, at an atmospheric temperature of 40 $^\circ$C, the theophylline became dehydrated and formed a cocrystal with the citric acid in the tablet (Arora *et al.*, 2013). SEM micrographs of the theophylline crystals before and after this change are displayed in figure 2.2. The morphological and chemical changes that occur in this system would undoubtedly cause changes to the way this tablet interacted with the human body if ingested in this state. Such studies highlight the importance of considering polymorphism and cocrystallisation when formulating pharmaceuticals and when considering their post-synthesis storage conditions.
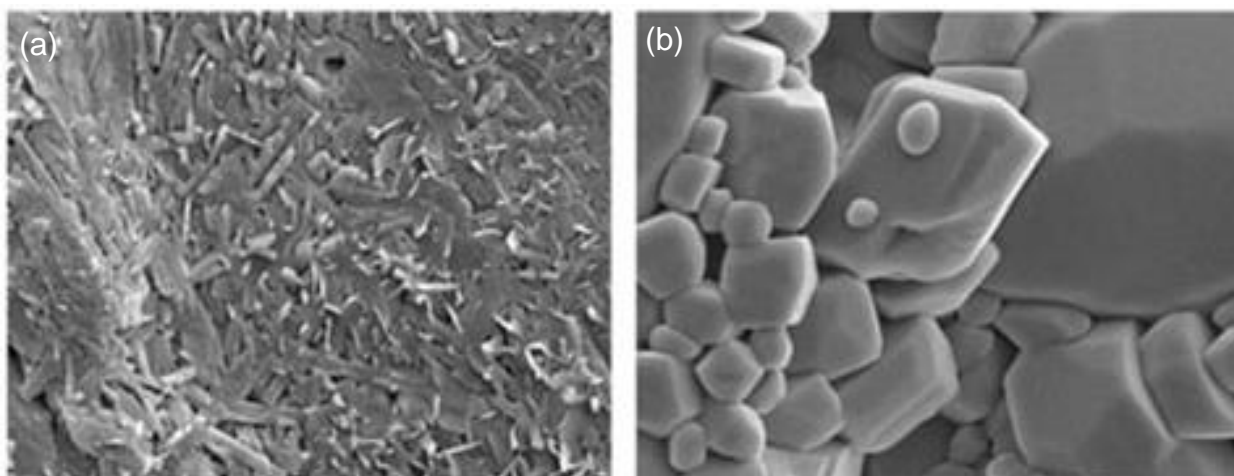
Fig.2.2: SEM micrographs of contents of theophylline/citric acid tablets (a) before heating to 40 °C and (b) 28 days later. Images from Arora *et al.* (2013).

8

2.1.2 - Theophylline

Theophylline is a xanthine derivative that has a molecular structure similar to caffeine. Figure 2.3 shows the molecular structures of both theophylline and caffeine. Discovered in 1888 by Kossel, it is used as a treatment for sleep apnea, asthma (Schultze-Werninghaus & Meier-Sydow, 1982), and chronic obstructive pulmonary disease (Barnes, 2006). There are many crystalline polymorphs of theophylline, with more still being discovered (a seventh has been characterised most recently by Eddleston *et al.*, 2015), as well as great number of cocrystals.
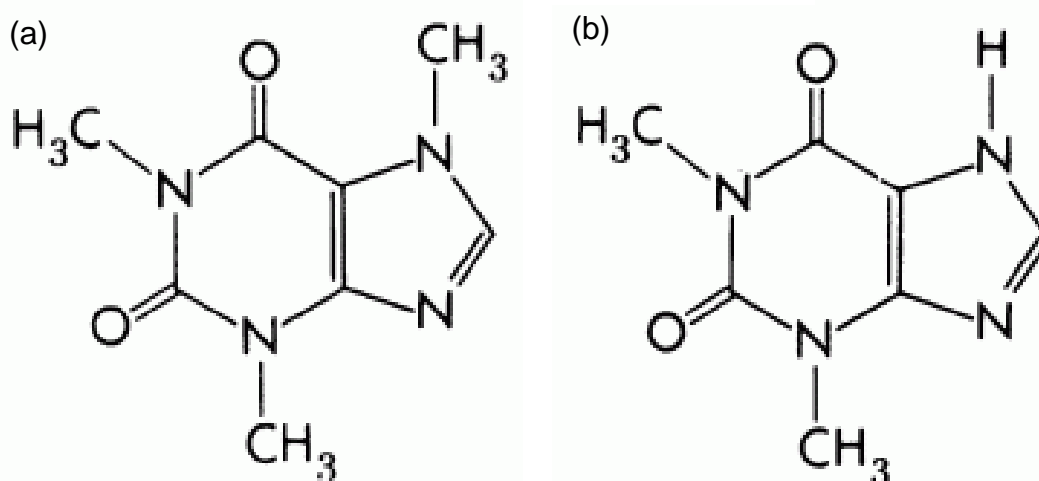
Fig.2.3: Molecular structures of (a) caffeine and (b) theophylline. The only difference between the two molecules is the presence of an extra methyl group on the 7-position nitrogen in caffeine.

The structure of form I was first presented by Suzuki *et al.* (1989). This form is typified by needle-like crystals several micrometres long and thick and was produced by heating form II at close to its melting point (heated at ~260 °C, melting point of form II is ~270 °C). It can also be formed by evaporation of an aqueous theophylline solution at temperatures above 90 °C over an extended time period (>24 hours).

Form II, also reported by Suzuki *et al.* (1989), can either be formed by dehydration of

9

the hydrated form M (by heating at ~100 °C at reduced pressure) or by recrystallisation of theophylline from nitromethane, ethyl acetate or other hydrophobic solvents (Eddleston, 2015). Form II crystals formed by dehydration of form M retain the original shape of the crystals, though appear as agglomerates of smaller particles. Form II crystals formed by recrystallisation however exhibit large, thin, triangular, plate-like crystals several micrometres in length and width, though only hundreds of nanometres thick (Eddleston, 2011). As will be shown, these are ideal for TEM study. Figure 2.4 shows a unit cell of theophylline form II along with its unit cell parameters. Its crystal system is orthorhombic with a Pna2$_1$ space group.
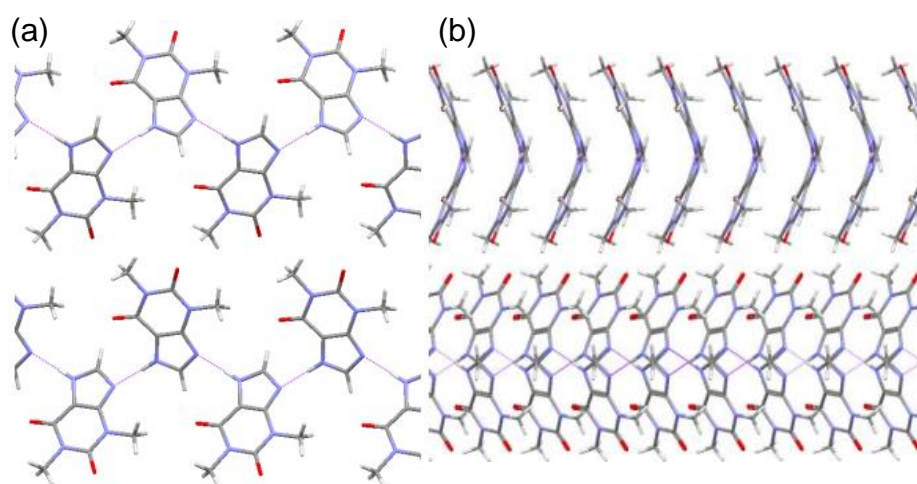
Fig.2.4: Crystal structures of form II of theophylline showing (a) the hydrogen-bonding chains of molecules and (b) a <110> zone axis view showing two layers of molecules arranged in stacks of hydrogen-bonded chains. Images from Eddleston, 2013.

Form III, first observed by Phadnis and Suryanarayanan (1997), can be prepared by vacuum dehydration of form M crystals. This form is highly metastable and rapidly converts to form II, dependent on atmospheric humidity (increased humidity causes faster conversion). As a result, its complete structure has yet to be fully characterised.

Form IV was first produced and characterised by Seton *et al.* (2010). Based on its solubility and the interconversion processes that occur, it was suggested that this form

is the most stable anhydrous polymorph of theophylline currently known. Forms I and II, if left in suspension in methanol for long enough (2 – 30 days) will convert to form IV, although they do remain stable in solid state environments.

Form V is produced by supercritical antisolvent precipitation of theophylline using CO_2 and was first produced by Roy *et al.* (2007). Crystals produced in this way were shown to display exceptional purity, making them a potential option for theophylline's pharmaceutical applications.
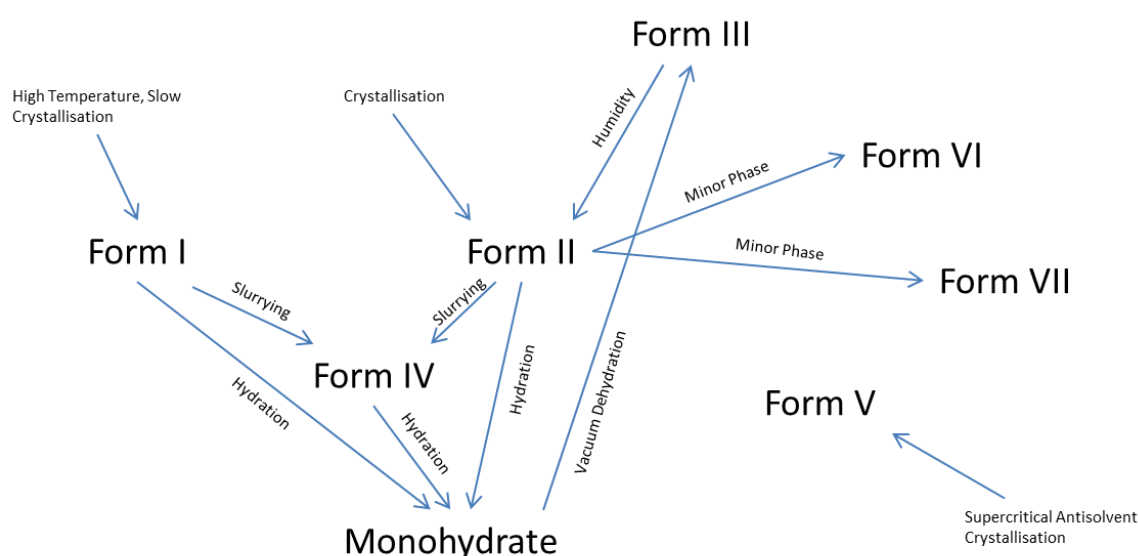
Fig.2.5: Theophylline polymorphs and their interconversion mechanisms.

Form VI was characterised by Eddleston *et al.* (2013). This form is present as a minor phase (<1 %) of form II crystallised from nitromethane. As such, this polymorph would go undetected by powder XRD. A combined TEM and crystal structure prediction approach was used, comparing diffraction patterns acquired from form VI crystals with global lattice energy minimisation calculations.

This same technique was used by Eddleston *et al.* (2015) to characterise the seventh anhydrous polymorph of theophylline (form VII). Similar to form VI, crystals of form VII are produced rarely when form II is produced by crystallisation from nitromethane or

ethyl acetate.
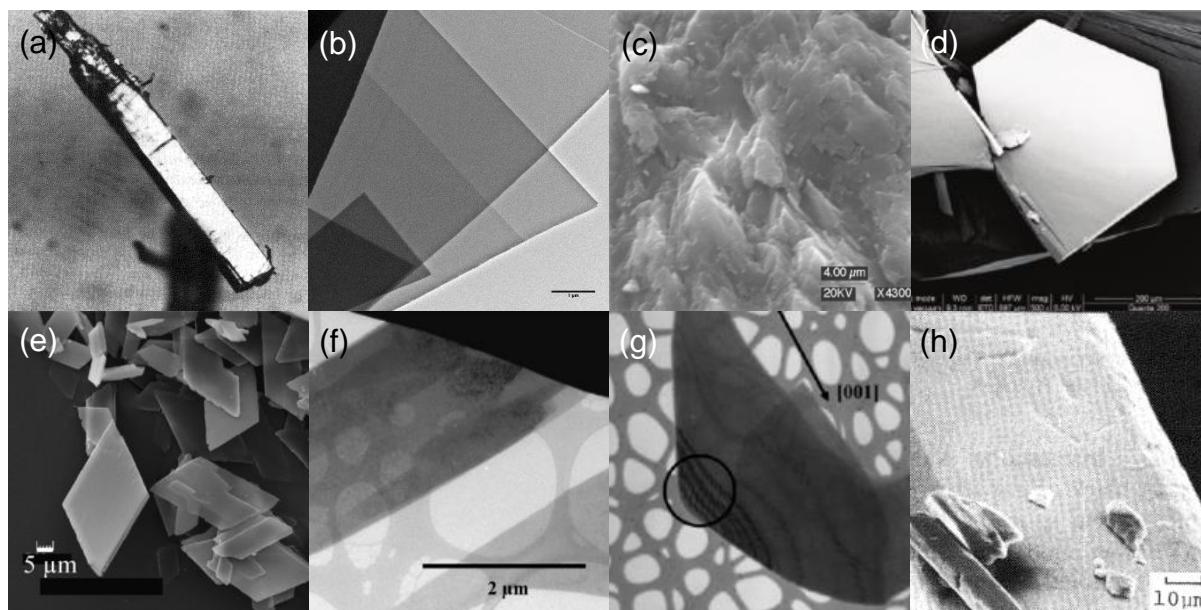
Fig.2.6: (a) Optical micrograph of theophylline form I (Suzuki *et al.*, 1989). (b) Transmission electron micrograph of form II. (c) Scanning electron micrograph of form III (Phadnis & Suryanarayanan, 1997). (d) Scanning electron micrograph of form I (Seton *et al.*, 2010). (e) Scanning electron micrograph of form V (Roy *et al.*, 2007). (f) Transmission electron micrograph of form VI (Eddleston *et al.*, 2013). (g) Transmission electron micrograph of form VII (Eddleston *et al.*, 2015). (h) Scanning electron micrograph of form M.

Figure 2.5 shows an overview of the theophylline polymorphs so far discovered and their interconversion pathways. Figure 2.6 shows a collection of optical, scanning electron and transmission electron micrographs representing each of the seven anhydrous polymorphs of theophylline as well as the hydrated form. Though these images represent the typical structures of each polymorphs, depending on the crystallisation route, many of these polymorphs can display a multitude of crystal morphologies. Form II, notably, displays a wide range of crystal morphologies based on the solvent used to synthesise it (Eddleston *et al.*, 2015), implying that crystal shape can be a somewhat unreliable parameter.

Form	M	I	II	IV	VI	VII
Crystal System	Monoclinic	Orthorhombic	Orthorhombic	Monoclinic	Orthorhombic	Orthorhombic
Space Group	$P2_1/n$	$Pna2_1$	$Pna2_1$	$P2_1/c$	$Pbca$	$Pna2_1$
a (Å)	4.4605	13.087	24.330	7.7055	9.749	26.579
b (Å)	15.3207	15.579	3.7707	13.0010	6.908	8.707
c (Å)	13.0529	3.8629	8.4850	15.7794	25.688	3.876
α (°)	90	90	90	90	90	90
β (°)	97.511	90	90	103.224	90	90
γ (°)	90	90	90	90	90	90

Fig.2.7: Table of various crystallographic parameters for theophylline polymorphs (excluding forms III and V, for which such data is unavailable). Data from Fucke et al, 2012 (forms M, I, and II), Khamar, 2011 (form IV), Eddleston, 2013 (form VI), and Eddleston, 2015 (form VII).

Theophylline form II was chosen as the model organic crystalline material for our experiments, owing to its well characterised structure, ease of synthesis, solid state stability and crystal morphology. The large, flat crystals produced are ideal for TEM analysis, owing to their electron transparency. Other forms would either be too unstable for consistent analysis (form III), too thick (form I) or are only present as minor phases of form II (forms VI and VII).

2.2 – Zeolites

Zeolites are microporous aluminosilicate materials with well-defined and controllable pore sizes that are widely used for their catalytic properties. Their inherent porosity gives them high surface areas and allows for the incorporation of other reactive ionic species which aid in or activate catalytic activity and selectivity (Bhatia, 1989). They were first named in 1756 by AF Cronstedt based on his observations of large quantities of steam being expelled from heated samples, 'zeo' meaning 'to boil' in Greek and 'líthos' meaning 'stone'. These observations arose as a result of the large amounts of water that had been adsorbed into the stone's porous structure boiling and being expelled from the structure as steam.

The typical atomic form of zeolites is that of TO_4 tetrahedra, where T = Si/Al in varying ratios. Purely siliceous zeolite, *i.e.* silica base tetrahedra, lacks a net charge. With the incorporation of Al and its +3 valence charge, the overall structure becomes negatively charged, and requires additional cations to balance the structure. The porous structure of zeolite allows cations such as Ti, Sn, Pb *etc.* to be introduced into the structure by various methods, activating their catalytic capabilities (Auerbach *et al.*, 2003).

Several hundred zeolite structures, both natural and synthetic, are currently known, and their complexity demands rigorous characterisation in order to understand the mechanics of their chemical activity.

2.2.1 – Beta Zeolites

The material of interest to this study is a dealuminated Si-beta zeolite doped with Sn, which has been shown to be a promising catalyst for a wide range of industrial-scale reactions (Corma *et al.*, 2002; Holm *et al.*, 2010; Moliner *et al.*, 2010). By

dealuminating the base beta-zeolite (as per methods described in section 3.5.1) a purely siliceous structure is produced which maintains the tetrahedral form of SiO_4. Post-processing steps can then be performed to dope this material with a variety of metals, such as Sn, Ti, Fe, and Cu to name but a few.

The development of beta zeolite was first described in the patent application by Wadlinger *et al.* (1964) for the then Mobil Oil Corporation, though due to its complex structure, was not characterised fully until 1988 (Newsam *et al.*, 1988). Through a combination of EM, ED, computer modelling, and XRD they found it to be a highly faulted structure comprising the intergrowth of two polymorphs, thereafter named polymorphs A and B. The extreme faulting and polymorph disorder are given as the reasons for the difficulty in fully characterising beta zeolite even up to this point.

2.3 – Analytical Techniques

Typically, organic crystalline materials are characterised by a number of different techniques. Powder X-ray diffraction (XRD) is one such technique and has been widely used over the last century to characterise the crystalline structure of numerous materials. It operates by firing a monochromatic beam of X-rays at a sample. Constructive interference between X-rays which satisfy Bragg's law ($n\lambda = 2dsin\theta$) is detected and collated. The Bragg angles, *2θ*, at which these rays are diffracted are directly related to d-spacings in the sample. By scanning across the full *2θ* range, all d-spacings of a sample can be determined and compared to a database to determine the identity of the sample.
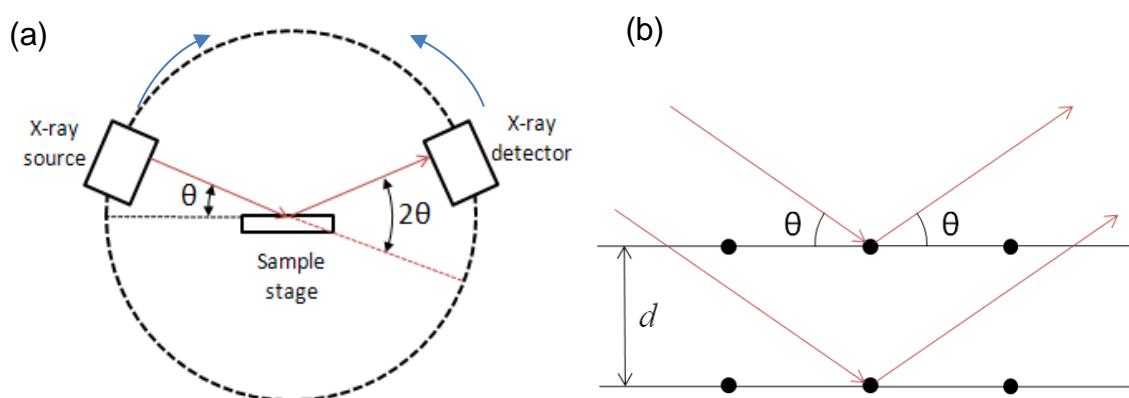
Fig.2.8: (a) Schematic diagram of X-ray diffractometry, showing the relative positions of the X-ray source and detector such that those X-rays which are diffracted and fulfil Bragg's Law (b) are detected.

Figure 2.8 shows schematics of a typical X-ray diffractometer setup and an example of diffracted X-rays which fulfil Bragg's Law. From the scattering angles and the intensities of the scattered beams it is possible to produce an electron density map of the sample from which the atomic positions can be reconstructed. XRD can also be used to characterise the purity of samples, whereby impurities in a sample cause

scattering peak broadening or introduce entirely new peaks. When attempting to catalogue the crystal structure of a new material however, purity is essential for producing a clean pattern. (Chung & Smith, 2000).

Single-crystal XRD is a technique which specialises in the analysis of single particles of a crystalline material. With a pure enough sample, this technique is regularly used to measure the position of atoms in the unit cell to within fractions of an angstrom (Bennett, 2010). In recent years this approach has also been shown to be feasible for electron diffraction (ED) (albeit with precession and rotation) (Gemmi *et al.*, 2019).

XRD techniques have some limitations. For one, powder XRD requires that at least 10 mg of a sample be produced for analysis. Amorphous materials or those with small grain sizes (<10 nm) cause scattering peak broadening. Additionally, if a sample has a second polymorph present as a minor component (<5 % of the total mass), it is likely to not be detected by XRD, as the scattering peaks will be masked by those of the major component or the background. Single-crystal XRD requires that a single high-quality crystal of a material can be grown to at least a size of 0.1 mm in each dimension. Depending on the material/polymorph, this may not be possible (Bennett, 2010). 3D ED can lower this size limit (albeit with a change in scattering factor from X-rays to electrons) (Gemmi *et al.*, 2019).

There are also other X-ray techniques beyond powder XRD. Small-angle X-ray scattering (SAXS) is a technique which detects low-angle (<10°) elastically scattered X-rays and is useful for analysis of large macromolecules such as proteins. It is advantageous in this regard in that samples do not need to be crystalline in order for SAXS analysis to be carried out (Feigin & Svergun, 1987).

Another common technique for the analysis of organic crystalline materials is Raman

spectroscopy. This technique proceeds by illumination of a sample by a laser of visible, near-infrared, or near-ultraviolet light. There is a small chance (~1 in 10^6) that a photon of the incident light will interact with phonons in the sample, scattering and shifting the energy of the incident photon. Different molecules will display different Raman shifts depending on the type of bond (atomic masses, bond lengths, and bond "stiffness"). This allows for molecular and polymorph identification (O'Brien *et al.*, 2004), contamination detection (Hardy *et al.*, 2014), and strain analysis (Ni *et al.*, 2008). Raman spectroscopy is advantageous in that samples need no special preparation beforehand. Aqueous samples can be analysed by this method too, as water is a weak scatterer of light. Raman spectroscopy is also non-destructive in most cases. However, depending on the incident beam frequency used and the absorption energies of the sample, it is possible to burn the sample. There can be problems acquiring significant scattered beam intensities, due to the rarity with which Raman scattering occurs, particularly in organic samples where there is little difference in mass between atoms in the molecules (larger mass differences between two bound atoms result in more Raman scattering events). There are variants of Raman spectroscopy (Lewis *et al.*, 2001) aimed at maximising the usable signal, although these add to the complexity of the technique.

Optical microscopy (OM) can be used to directly observe the morphology of crystals of a material and has many variants specialised at analysing particular features and properties (Herman & Lemasters, 1993). Whilst a good tool for macroscale materials analysis, due to the inherent resolution limit of light, analysis of nanoscale properties and materials is impossible for conventional OM. Typically, OM has a resolution of a few hundred nanometres based on the Rayleigh resolution criterion:

$$(2.1) \quad \delta = \frac{0.61\lambda}{NA}$$

δ represents the smallest resolvable distance, based on λ, the wavelength of the light being used for the observation, and NA, the numerical aperture of the microscope. The NA itself is determined by the refractive index of the medium surrounding the sample and the collection semi-angle of the lens. Generally, the minimum possible resolved distance is equal to roughly half the wavelength of the light used for imaging (typically ~500 nm). More modern techniques have pushed the resolution limit of OM below 100 nm (with specific sampling strategies) (Betzig *et al.*, 2006), though this is still insufficient for analysis of many nanoscale features and materials (Hao *et al.*, 2013).

Scanning probe microscopy (SPM) techniques such as atomic force microscopy (AFM) and scanning tunnelling microscopy (STM) can also be used for analysis of organics. Both operate similarly; AFM makes use of a reflective piezoelectric cantilever with an atomically thin tip which is then moved across the surface of a small section of a sample. A laser is reflected off the back of the cantilever into a detector. There are several imaging modes used in AFM, though the most general one sees the cantilever scanned across the surface of a material and allowed to freely change height, causing a change in the deflection angle of the laser. These deflection changes can be mapped into false-colour images of the scanned area (Eaton & West, 2010). STM operates similarly, but instead relies on the tunnelling effect of electrons from a conducting, atomic tip to the sample. The intensity of the detected current depends on the distance of the tip from the sample surface and the electron density in the sample (Chen, 2008). STM of organics is limited to highly conducting samples such as conducting polymers.

Advantages of these SPM techniques is the relative ease with which atomic resolution images can be achieved, in a non-destructive manner and from a wide variety of samples, be they organic, inorganic, submersed in water or oil, in a specific gaseous environment or at high/low temperatures. Some disadvantages include the relatively small scanning area (maximum of 150 μm^2 for AFM and ~20 μm^2 in STM) and limited height adjustability of the cantilevers (20 μm for AFM and >1 μm for STM), which somewhat limits the morphology of samples that can be accurately analysed by these techniques (Eaton & West, 2010; Chen, 2008).

Characterisation of zeolites comes with its own challenges, even though these materials are generally more stable under electron irradiation than organic specimens. Due to the complex structure of beta zeolite and difficulty associated with characterisation, determining the exact position of dopants within the atomic structure is a complicated task. In the case of Sn-beta, there has yet to be conclusive evidence acquired which identifies the specific tetrahedral atomic site (T-site) or sites which Sn occupies upon inclusion into the zeolite structure (there are 9 independent T-sites in the beta structure). Numerous studies have previously been carried out in attempts to determine this. Shetty *et al.* (2005) and Yang *et al.* (2013) used density functional theory (DFT) to determine the most energetically preferential site for Sn occupancy and both found that the T2 site was preferable. DFT is a versatile and widely utilised computational method used to model the ground-state electron structure of materials, based on functions of electron density. Bare *et al.* (2005), using multishell fit modelling of extended X-ray absorption fine structure (EXAFS), found that Sn was substituted as pairs into the T1 and T2 sites on opposite sides of a pore. While each of these studies considered closed atomic sites (*i.e.* a stable, charge balanced structure), Josephson *et al.* (2017) studied open sites (*i.e.* ionised sites) also using DFT. They

found that the T1 and T9 sites were preferential for Sn occupancy. More recently, Kolyagin *et al.* (2018) used magic-angle spinning nuclear magnetic resonance (NMR) analysis on Sn-beta samples, and found the T5, T6, and T7 sites to be the most populated by Sn.

Atomic resolution EM has the capability to identify Sn in the beta structure and potentially determine the exact T-site location. More generally, EM is the major characterisation technique which this thesis will explore for pharmaceutical compounds and zeolite materials.

2.3.1 – Electron Microscopy

There are a number of analytical electron microscopy (EM) techniques. Each one uses a focussed beam of high-energy electrons incident on a sample, and form image contrast based on various scattering effects and interactions between the two. Electrons are used because their wavelengths are much shorter than that of light when accelerated, allowing for much improved resolution limits. Said limits can be estimated from the electrons' accelerating voltage, V, by this non-relativistic expression derived from the de Broglie equation:

$$(2.2) \quad \lambda\,(nm) = \frac{1.22}{V^{\frac{1}{2}}}$$

For typical electron voltages in the TEM (80 – 300 kV), this results in a resolution limit of ~0.001 nm, well below that needed for resolution of individual atoms. Hardware imperfections are generally the limiting factor for resolution in modern EMs, with the lenses being the primary sources of spherical and chromatic aberrations (although electron sources also contribute). Sample movement and vibration caused by heat,

charging, and acoustic/electronic noise also cause a loss of resolution (Williams & Carter, 2009).

2.3.2 – Transmission Electron Microscopy

In TEM, a high energy beam of electrons (80 – 300 keV) is focussed through a thin sample (typically <500 nm) and the numerous scattered beams and interaction products can be detected in order to analyse a sample in a number of different ways. The main advantage of TEM over many other techniques is its potential for incredibly high-resolution imaging and analysis, with atomic resolution regularly achievable for many samples and materials. Additionally, TEM can be applied across a wide range of magnifications, allowing for characterisation of both microscale and nanoscale properties in quick succession. Contrast in TEM images is formed by mass difference, thickness difference, diffraction scattering, and phase differences (Egerton, 2008).

TEM is widely used for observation of inorganic materials and is also commonly utilised for analysis of biological materials. Due to the high vacuum conditions of the electron beam column, biological samples dry out and deform, with cellular samples rupturing. To counter this, such samples are regularly chemically immobilised, resin embedded, or frozen by plunging into liquid ethane, allowing biological materials to retain their structures and resist damage from the vacuum. These methods do not allow for *in situ* observations however. Low fluence conditions must also be used for analysis of frozen biological material, as the electron beam is easily capable of damaging biological samples or the stabilisation media (Williams & Carter, 2009). Low fluence conditions in TEM typically involve limiting the number of electrons per unit area per second (electron flux) that pass through a sample in order to limit sample

damage. A number of other factors, such as accelerating voltage, temperature, specimen thickness, and conductivity affect damage as well and will be outlined in section 2.4.

Observation of organic materials in TEM is similarly affected by the electron beam. Many interactions between the electron beam and the sample transfer a lot of energy between the two. Inorganic materials generally form through either ionic or covalent bonding of all the atoms in a crystal, making them stronger than most organic materials. Organic crystals and compounds are molecular crystals bonded by weak Van der Waals and often hydrogen bonding, thus are generally poor conductors. Interactions between the beam and sample cause various excitation and charging effects which cannot be easily balanced or conductively screened by organic materials, so damage is the result.

2.3.3 – Scanning Electron Microscopy

SEM is a materials characterisation technique primarily used for analysis of sample surfaces. It utilises a beam of electrons accelerated and focused through a number of electromagnetic lenses which is scanned across a sample. Electrons interact with the sample in a number of ways; most are absorbed into the sample itself, but many others are reflected back out of the sample via high-angle incoherent elastic scattering from the nucleus of atoms in the sample. These are known as high-energy backscattered electrons (BSE) and have energies similar to the incident beam energy.
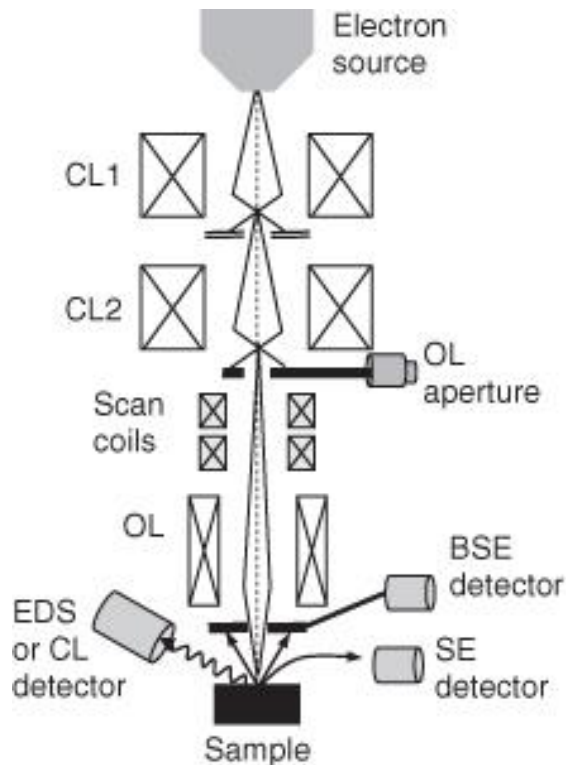
Fig.2.9: Schematic of an SEM column showing the path of the electron beam as well as the positions of the condenser lenses (CLs), objective lenses (OLs), scan coils, BSE, SE, and electron dispersive spectroscopy (EDS) detectors. Image from Bell & Erdman (2012).

Other electrons are displaced from the sample itself and are known as low-energy ($\lesssim$50 eV) secondary electrons (SE), and are produced as a result of ionisation processes. Each of the above can be used for image formation. BSE images are useful for observation of areas of different elemental composition, since heavier elements are more likely to scatter electrons to the high-angles required to direct them back out of the sample. SE imaging is a more general imaging mode, and gives detailed topographical information, as these low-energy electrons can only escape from the top ~10 nm of the specimen surface. However, similar to TEM, biological samples and crystalline organics are still susceptible to damage by the electron beam. Illumination of the sample is also inherently different between TEM and SEM. Where TEM uses parallel illumination of a sample area, SEM uses a converged beam which is then

24

scanned over a selected area, in a similar way to an AFM or STM probe (Reimer, 2013). Figure 2.9 shows a schematic of an SEM column, showing the path of the electrons, lenses, sample location, and detectors.

Though the maximum resolution of SEM is much more limited compared to TEM due to the spreading of the electron beam in the bulk of the specimen, there are still many uses for SEM when it comes to analysis of organic materials. It is particularly useful for morphological characterisation of surface defects, both of bulk materials and dispersions of particles. Surface properties are important in tabletted pharmaceuticals in determining the dissolution properties (and by extension, their bioavailability) of the active pharmaceutical ingredient (API). An SEM may also be equipped with EDX and STEM detectors, though these operate at a lower electron accelerating voltage range than in TEM or dedicated STEM equipment and so require a thinner sample.

2.3.4 – Scanning Transmission Electron Microscopy

STEM is a TEM imaging mode wherein the usual parallel illumination used in conventional TEM (CTEM) is condensed to a converged probe and scanned across a sample in a similar manner to SEM (Herman & Lemasters, 1993). This technique allows for slightly higher maximum resolution than TEM and also prevents the effects of chromatic aberration, since the imaging lenses used to magnify the TEM image are not used by STEM (magnification comes from difference in size between the scanned area and the camera dimensions). Many other aberration mechanisms still take effect however and are the limiting factors determining maximum resolution in STEM. Modern dedicated STEM may have spherical aberration correctors, which significantly improves the size and current control of the probe. This allows for extreme imaging

clarity at ultra-high magnifications (Brydson, 2011). Figure 2.10 shows a comparison of beam propagation in STEM and TEM modes.

STEM has similar issues to other EM techniques when it comes to imaging biological and organic materials, namely the high vacuum conditions which destroy exposed biological samples, and beam damage. There is currently no clear distinction as to whether STEM imaging reduces beam damage when compared to TEM. It has been suggested that, due to the scanned nature of STEM, a sample is potentially given time to recover between scans even though the current density in the focussed beam is many times higher than in TEM. Another suggestion is that the beam in STEM is focussed to such a degree that a sample is damaged heavily with every pass and accumulates as the beam progresses, faster than it otherwise would in TEM. More experimentation is required to determine which, if either of these, is the case. It may be that both are applicable depending on the sample. Egerton *et al.* (2015) suggest that STEM may be useful for analysis of samples that display inverse dose-rate effects, whereby damage sensitivity decreases with increased dose rate up to a certain threshold. This effect occurs as a result of diffusion of damage in the specimen being outpaced by the arrival of new electrons. Above a certain dose threshold however, heating damage will take over.

Another consideration is that HR STEM of organic and biological materials is particularly susceptible to hydrocarbon contamination. The beam will rapidly induce the polymerisation of free hydrocarbon species, causing sample thickening, making focus with STEM difficult. Additionally, for sensitive materials, low fluence STEM conditions can be used which involves reducing the probe current, increasing scan speed, and lowering magnification. However, as with TEM, it is possible that these conditions lower the signal-to-noise ratio (SNR) to such a point that limited usable data

can be gathered (Sader *et al.*, 2010).

STEM does have one notable advantage over CTEM in terms of sample exposure. The parallel illumination of the sample in CTEM often means that a large area outside the region being observed is exposed to the beam and therefore damaged. For beam sensitive materials this usually means that very few observations or measurements can be made per crystal. With STEM, the observed area and the beam exposed area are one and the same. As such, many high magnification observations can be made per sample crystal. Less sample is wasted during focus in STEM as well, since focussing is done by bringing the Ronchigram (the point of diffraction pattern convergence) into focus on the sample at high magnification.
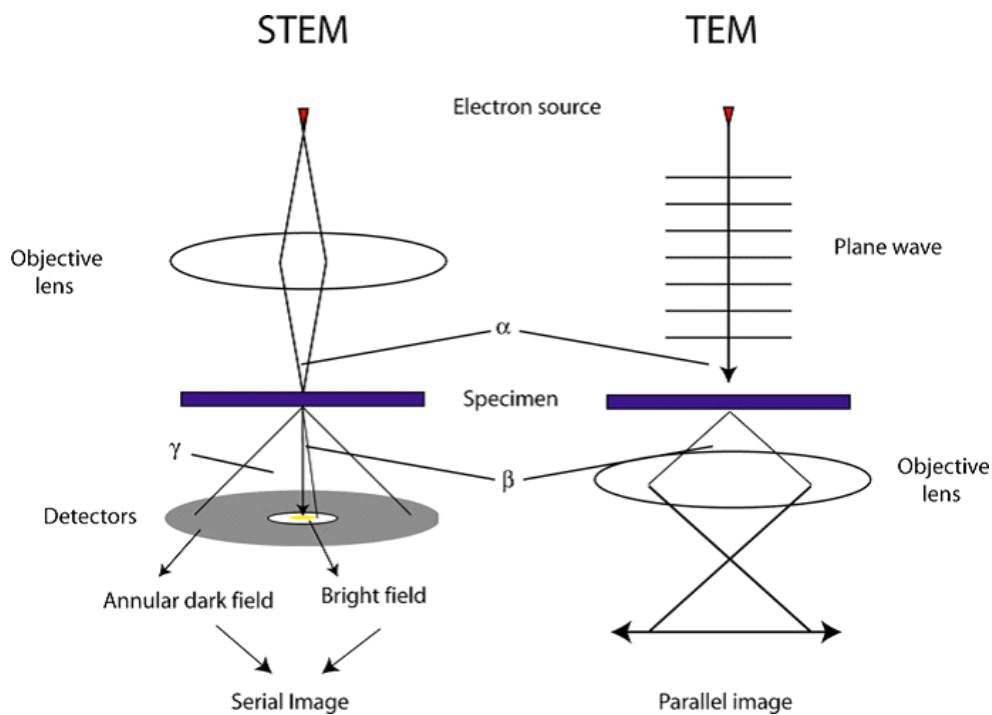
Fig.2.10: Beam propagation in STEM and TEM modes. Angles α, β, and γ respectively represent the electron beam focus, bright-field and dark-field semi-angles. Image from Sader *et al.* (2010).

2.3.5 – STEM High-Angle Annular Dark-field

High-angle annular dark-field (HAADF) imaging is a STEM-based transmission technique that allows for high-resolution analysis of a sample based on the mass of the atoms in the sample. This is done by only sampling from transmitted electrons scattered to high angles (>50 mrads). In doing so, electrons scattered by Bragg diffraction are not collected, removing phase contrast from the resulting images. Electrons scattered to such high degrees are only scattered by incoherent Rutherford scattering around the nucleus of the atoms in the sample, hence higher atomic number (Z) elements will be responsible for more scattering events. When collected, these high Z elements will appear brighter in the image compared to their lower Z-number counterparts. Additionally, more densely packed atomic columns will also be responsible for more scattering events. Therefore, if true Z-contrast is desired, incredibly thin samples (<10 nm) are required (Williams & Carter, 2009).

2.3.6 – Phase Contrast and Lattice Resolution

Bright-field phase contrast arises from phase changes applied to electrons which have been diffracted by atoms in the specimen ($\frac{\pi}{2}$ in the case of Bragg diffraction). Samples that are thin enough such that transmitted electrons undergo at most one diffraction event are called phase-objects. In cases where the sample is so thin that the transmitted and incident electron beams are nearly identical in intensity, the specimen is called a weak phase object (WPO) (Goodhew *et al.*, 2008). Collection and superposition of both the unscattered and phase-shifted electrons produces contrast based on the phase differences between the two and is the principle behind the formation of atomic lattices in BF-TEM images. Phase contrast in BF-STEM is

technically an approximation to phase contrast in BF-TEM by reciprocity. While it is not as efficient in terms of electron collection, it has other advantages in terms of detection, focussing efficiency, and dose-rate sensitivity (Sader *et al.*, 2010).

2.3.7 – STEM Differential Phase Contrast
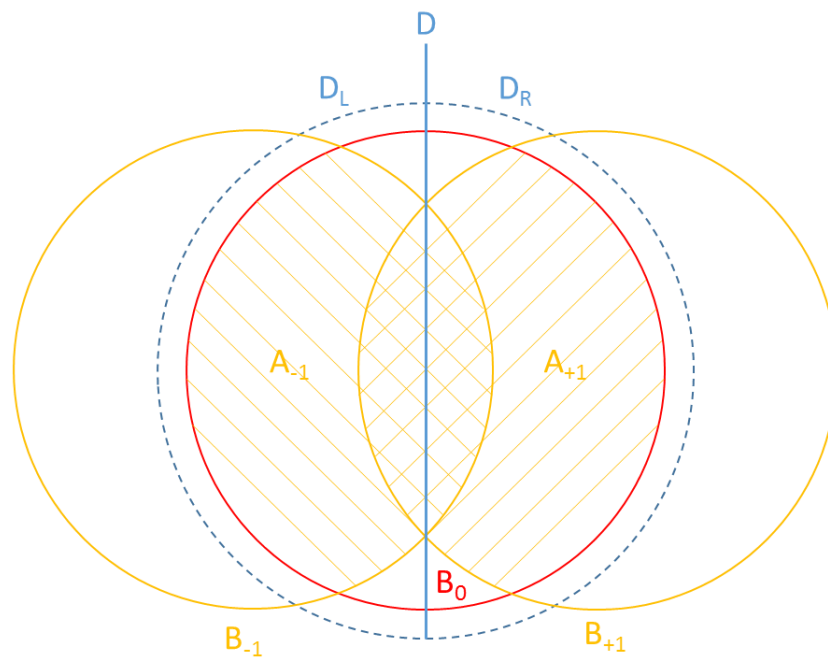
Fig.2.11: Schematic of the STEM detection plane with a WPO. The incident beam B_0 produces the diffracted beams B_{-1} and B_{+1}. Interference in the regions A_{-1} and A_{+1} is picked up by the two halves of the detector D (D_L and D_R). Reproduced from Dekkers and de Lang (1974).

STEM differential phase contrast (DPC) is an imaging method designed to remove amplitude contrast (incoherent scattering of electrons around the nucleus of atoms in the specimen) in favour of enhanced phase contrast. The original theoretical groundwork for this technique was described by Dekkers and de Lang (1974). In their work they outlined details of a detector split into two equal halves where the signal from each would be subtracted, a schematic of which is shown in figure 2.11. This has the effect of cancelling out the signal from the zero-order beam, but enhancing the contrast resulting from the overlap of the diffracted beams. This is a useful technique

for characterisation of WPOs. This technique can be taken further, by splitting the detector into quadrants to produce a pair of perpendicular DPC images and integrating them, a technique called integrated DPC (iDPC), the basis of which is laid out in Lazić *et al.* (2016). This reduces the contrast between light and heavy elements but boosts the signal to allow simultaneous imaging of both.

2.3.8 – Scanning Moiré Fringes

An alternative to attempting to directly resolve the crystal lattices of sensitive samples presents itself in the form of scanning moiré fringes (SMF). These fringes are the result of constructive interference between real lattice spacings in the sample, and the scanned 'lattice' produced by the raster motion of the beam and camera. The resultant moiré fringes are larger in size than either of the base lattices but in principle maintain information about the real lattice of the sample, such as defects. Additionally, if the orientation between the scanned lattice and the real lattice is known, the d-spacing of the real crystal lattice can be determined.

The size of the produced general SMFs (d_{gm}) depend upon the magnification used (which determines the scanned pixel size and therefore the size of the scanned lattice (d_s)), the size of the base crystal lattice (d_l), and the offset angle between these two lattices (β). These factors are related by the following equation:

$$(2.3) \quad d_{gm} = \frac{d_l d_s}{\sqrt{(d_l - d_s)^2 + d_l d_s \beta^2}}$$

In the straightforward of circumstances, the angle between the two lattices will be 0°, and a simplified equation can be used to determine d_{tm} (translational moirés):

$$(2.4) \quad d_l = \frac{d_{tm}d_s}{d_{tm} + d_s}$$

Figure 2.12 shows schematics for the formation of translational and general moiré fringes.
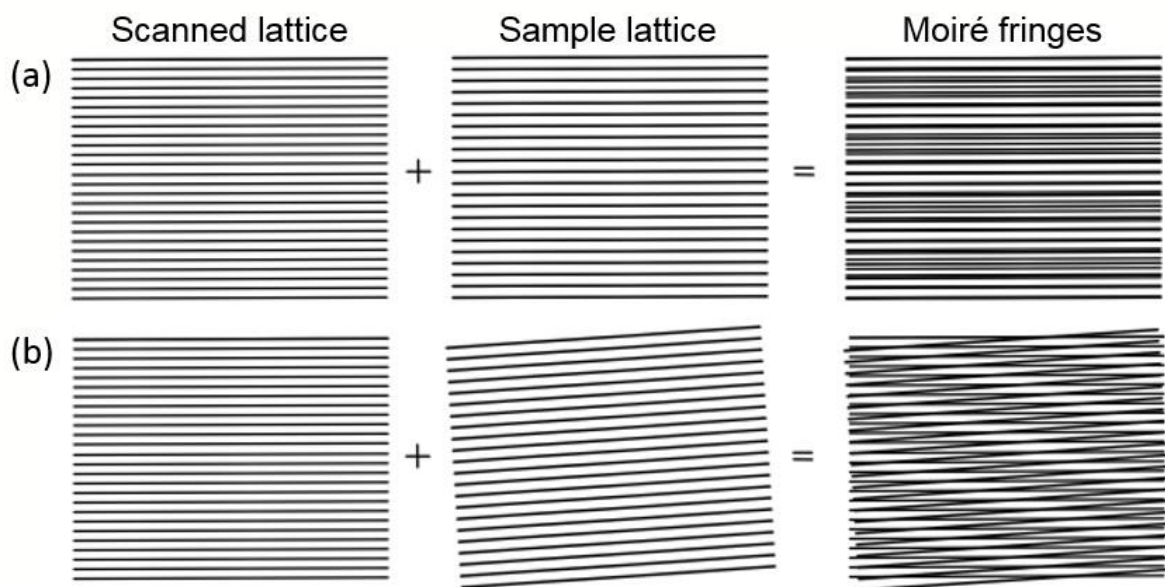
Fig.2.12: Schematics of (a) translational and (b) general moiré fringe formation by the interference of a scanned lattice of known orientation and size, and a sample lattice.

SMFs have been used successfully to analyse beam sensitive organic crystalline materials such as in S'ari *et al.*, 2019, which includes the successful analysis of SMFs in theophylline, furosemide, and felodipine, two highly beam sensitive organic crystalline materials with pharmaceutical properties. Multiple defects were identified in both of these samples, highlighting a potential use of SMF analysis in understanding the effects of pharmaceutical formulation methods on pharmaceutical materials.

2.3.8 – Energy Dispersive X-ray Spectroscopy

When the electron beam interacts with the sample, there is a probability that electrons orbiting atoms in the sample are ionised. If the electron was ionised from an inner

orbital, an electron from a higher energy orbital will expel energy and transition to the lower energy orbital to take its place. In doing so, an X-ray may be produced. These X-rays carry energy equal to the difference in energies of the orbitals of the atomic electron transitions between and is therefore characteristic for a given element and given energy levels. As such, EDX is the method by which the X-rays are collected and their energies dispersed, such that the elements they originated from can be identified (Garratt-Red & Bell, 2005). This technique is primarily used to assess the stoichiometric ratio of atoms within a sample, though it can also be used during EM analysis to check for specimen alteration. Additionally, elemental maps can be constructed that show the distribution of elements in the imaged area. Such maps are useful for separating phases and their boundaries in multi-phase systems and are also useful for the analysis of homogeneity in continuous samples. EDX analysis of sensitive materials can be complicated. A suitable EDX map or spectrum requires a high SNR, which would be achieved through high beam current. As such, depending on a material's sensitivity, it may only be possible to acquire EDX data of an organic compound that has already been subjected to significant electron beam damage. Whether or not this will have had an effect on the elemental composition of a sample will depend heavily on the sample itself and its resistance to mass loss (Egerton *et al.*, 2004).

2.3.9 – Electron Energy-Loss Spectroscopy

EELS produces a spectrum of electron energies from the electrons transmitted through the sample, the peaks of which are specific to certain elements and their bonds. When an incident electron interacts with a specimen, some of its energy will be transferred into the specimen. Electrons which did not interact with the specimen

will have retained all of their initial energy (zero-loss electrons). The amount of energy an interacting electron loses is dependent on the interaction mechanism and EEL spectra can be compared to databases to identify these core-edge interactions (Brydson, 2001). Like EDX, EELS needs a high SNR in order to resolve a clear peak in a spectrum. In the case of sensitive organics, this proves difficult to achieve, as highlighted by Brydson *et al.* (2014), and their attempts to acquire EELS spectra of theophylline and paracetamol. Due to the low SNR, limited information could be obtained from the spectra (essentially just the elemental composition). However, with further optimisation of detector collection efficiency, sample stabilisation by cooling, and the use of STEM EELS (which has previously been used for the analysis of sensitive materials (Haruta & Kurata, 2012)), such spectra could be highly useful for polymorph analysis in the future.

2.3.10 – Summary

Bright-field transmission imaging methods could be regarded as the most efficient approaches to low fluence imaging of structure as they collect the majority of scattered electrons. Thus, BF-TEM and BF-STEM are the most obvious techniques to explore in this work for the analysis of beam sensitive pharmaceutical compounds. However, beam damage will always be present and an awareness of damage mechanisms and mitigating strategies is required.

2.4 – Electron Beam Induced Damage

Beam damage is the main factor which limits high-resolution analysis of many inorganic and organic materials using EM. There are a number of different damage mechanisms and for each EM technique, different mechanisms will dominate (Egerton *et al.*, 2004).

2.4.1 – Radiolysis
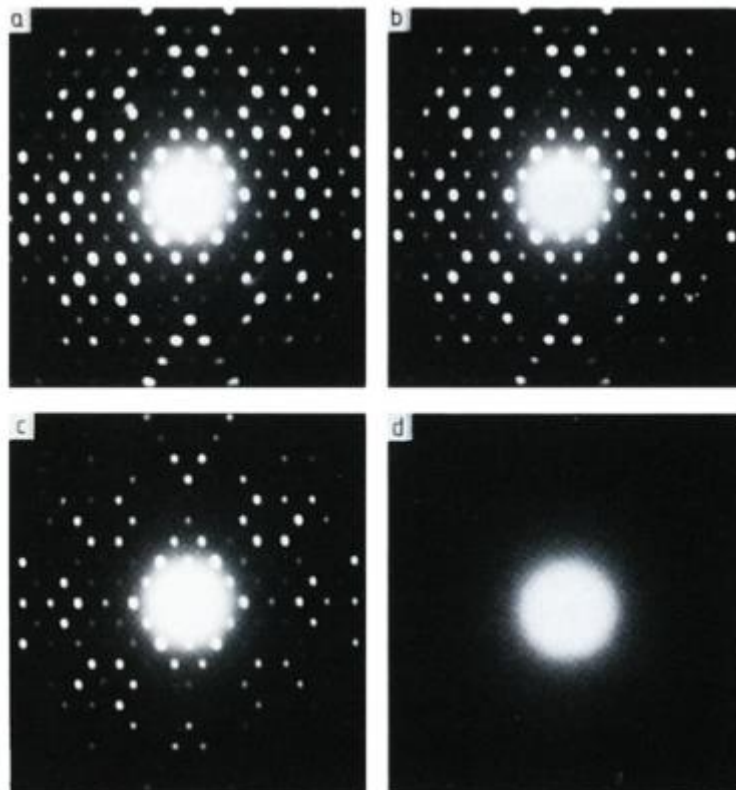
Fig.2.13: Diffraction pattern intensity decay for a chloro-copper phthalocyanine specimen under electron beam irradiation. Total electron fluences at which each pattern was captured were 625, 3000, 9062, and 15625 e$^-$Å^{-2} for patterns a-d respectively. From Clark *et al.* (1980).

Radiolysis is the primary mechanism responsible for damage in organic materials in TEM (Egerton *et al.*, 2004). It occurs for a given dose through the inelastic transfer of energy from the electron beam to molecules in the sample, resulting in excited electron

states. Since crystalline organic materials have limited conduction capabilities, these excited states cannot be easily de-excited and cause the breakage of both intermolecular and interatomic bonds. As this happens, atoms and molecules shift positions, leading to gradual loss of crystallinity. The speed with which this occurs relies heavily on the material's bond strengths and conductivity, with aromatic compounds being relatively resistant to this type of damage, likely due to the delocalisation of electrons within the rings.
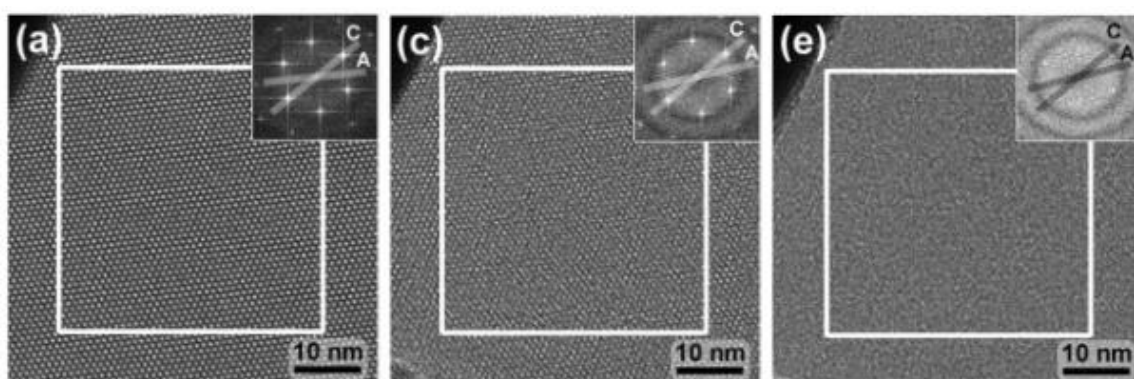
Fig.2.14: TEM images of a zeolite with inset FFTs at (a) 25 s, (c) 85 s and (e) 220 s after the start of beam exposure. Images from Ugurlu *et al.* (2011).

Figure 2.13 shows the effect of radiolysis on a chloro-copper phthalocyanine specimen (Clark *et al.*, 1980). The dimming and disappearance of the spots is typical for radiolytic decay of an organic material and shows many of the outermost spots fading before certain inner spots. This is indicative of the loss of short-range order (interatomic positions) before the eventual loss also of long-range order (molecular positions). Figure 2.14 shows the effects of radiolytic damage in an inorganic aluminosilicate zeolite resolved to the atomic scale. It can be seen that, over time, the images become distorted as the crystalline structure is gradually lost, and the fading of spots and increasing intensity of the amorphous rings in the fast Fourier transforms (FFT) also highlight the progression of the damage.

2.4.2 – Heating

Similar to radiolysis, the inelastic interactions between the beam and the sample causes the build-up of heat in a sample, as a result of energy transferred to atomic electrons in the sample. The decay of excited states within the sample can also result in heat production. This damage depends on the beam current and the size of the probe, as well as sample properties, with more conductive samples able to dissipate heat build-up more effectively than insulators. This type of damage can be significant in some non-crystalline organics, such as polymers, but for crystalline organics, radiolysis causes degradation of the crystal structure long before heating effects become a problem (Grubb, 1974).

2.4.3 – Charging

There are two types of electrostatic charging that can occur in samples in EM. In SEM, the bulk samples typically observed are particularly prone to both types (Reimer *et al.*, 1992). Depending on the conductivity of the sample and the electron beam energy used, either positive or negative charging will occur. For negative charging, electrons from the incident beam penetrate deep into the sample and are absorbed. Many SEs produced will also be absorbed. This increase in electrons in the sample cause a net negative build-up of charge. If the beam energy is lowered, the beam electrons do not penetrate as far, so are more likely to be scattered back out without being absorbed. SEs produced are more likely to escape the sample surface as well. In cases where the number of electrons escaping the sample is greater than the number being absorbed, positive charging can occur. In thin samples in the TEM, charging can also occur, though at a generally reduced intensity as much of the beam will be transmitted

straight through the sample (Egerton *et al.*, 2004). In organic crystalline materials, it is unlikely the damaging effects of charge build-up will be seen before crystallinity has already been destroyed by radiolysis. Charging is much more a problem for non-crystalline organics, like polymers, as charging effects can cause them to deform, tear and move. Conductive coatings are useful for such materials, as these effectively disperse the charge before a damage build-up can form.

2.4.4 – Atomic Displacement

Material	E_d (eV)	E_t (keV)
Graphite	30	140
Diamond	80	330
Aluminium	17	180
Copper	20	420
Gold	34	1320

Fig.2.15: Displacement energies (E_d) and threshold incident energies (E_t) required to cause atomic displacement of atoms in a number of different materials. Values from Hobbs (1987).

Also called knock-on damage, atomic displacement is the elastic transfer of energy between beam electrons and atomic nuclei in the sample. The energy transferred is dependent on the accelerating voltage applied to the electron beam and the recoil angle of the electron, with maximum energy transfer occurring at 180° recoil angle. If the energy transfer is sufficient, atoms can shift position to a different site, creating vacancies and interstitial Frenkel pair defects. As more of these events occur, the

crystallinity of the sample is degraded. This damage type is more a worry for conducting inorganic materials; radiolysis and other mechanisms cause crystallinity degradation much faster in organic samples (Hobbs, 1987). Figure 2.15 shows some experimentally derived displacement and electron beam energies (energy required to displace an atom and beam energy required to transfer this amount of energy in one interaction respectively) required to cause this effect, noting particularly the difference in energy required to displace carbon atoms in graphite compared to carbon atoms in diamond.

2.4.5 – Sputtering

Similar to atomic displacement, sputtering refers to the knock-on damage that occurs on the surface of samples, usually the electron beam exit surface of a sample in TEM (Egerton *et al.*, 2004). Atoms on the surfaces of samples, instead of shifting position to an interstitial site, can instead be ejected entirely from the sample. Since surface atoms have fewer neighbouring atoms and interactions thereof, less energy is required to knock them out of the sample. Both atomic displacement damage and sputtering damage depend heavily on the atomic mass of the ejected atom and the energy of the beam. There will be a threshold energy for each atom, above which energy it may be possible that an incident electron could cause a displacement. This threshold energy will be lower than for atomic displacement in the bulk, owing to the sputtered atoms being located at surface, so are less energetically bound in the sample.

2.4.6 – Hydrocarbon Contamination

Hydrocarbon contamination occurs when hydrocarbons in the vacuum or from the

surface of the sample itself diffuse into the area illuminated by the electron beam, move across the surface of the sample and polymerise. The result is an increasingly dark spot in bright-field imaging which can usually only be observed upon reducing magnification to observe a larger area (Egerton *et al.*, 2004). Improved vacuum systems in modern EM machines work to reduce this effect, but in organic samples that act as a source of hydrocarbons, contamination is difficult to avoid, particularly at higher magnifications. Contamination can be a hindrance to analysis, particularly for analysis which requires that a sample remain clean or as thin as possible, such as STEM-EDX or EELS. EELS itself can be useful in this regard, as it can be used to estimate the increase in sample thickness caused by hydrocarbon contamination (Brydson, 2001). One upside to carbon contamination is that it can be used to prevent atomic sputtering, particularly if present on the exit surface of a specimen.

2.4.7 – Mitigating Damage

When using TEM, organic materials are particularly susceptible to radiolysis, heating, charging, and hydrocarbon contamination. Sputtering and knock-on damage will have less of an effect on samples, as the threshold energies needed to cause these damage mechanisms are generally higher than for radiolysis *etc*. The degree to which a material is affected by each of these is reliant upon the properties of the material itself. For example, many polymers are particularly susceptible to damage by overheating, due to their poor thermal conduction, particularly those not coated or otherwise incorporating metals (Han & Fina, 2011). Though observation of organic crystalline materials under EM may be difficult, it is far from impossible, however it does require a greater degree of preparation and consideration of the exact beam and sample conditions one will use. The simplest strategy for limiting beam induced damage is to

limit the current density in the electron beam. This can be achieved in conventional TEM by using smaller spot sizes and spreading the beam, and in STEM by reducing the beam current. Though effective at preventing cumulative damage mechanisms like heating and charging, this method does not halt radiolytic (or knock-on) damage and sensitive samples will degrade, albeit at a slower rate. Additionally, there are many samples that are so beam sensitive that, even when a low beam current density is used, they will still damage completely and degrade before useful data can be acquired. At such low current densities, the SNR becomes so low that just being able to see the sample or detect a signal becomes a challenge (Egerton, 2013).

Changing the accelerating voltage applied to the electron beam has multiple effects. For TEM ranges (80 – 300 kV is typical), increasing accelerating voltage decreases both the elastic and inelastic cross-sections of the beam. These cross-sections determine how likely it is that an electron will interact with atoms in the sample. Increasing accelerating voltage reduces radiolytic damage by decreasing the number of interactions between the beam and the sample, allowing sensitive materials longer lifetimes while exposed. The downside to this is that by decreasing the number of interactions the SNR is also decreased, since fewer interactions give fewer scattered electrons that can be used for contrast formation. Thus, a balance between damage reduction and signal generation must be struck for optimal imaging (Williams & Carter, 2009) (see section 5.1 for discussion of this concept, dose-limited resolution). This holds true for radiolytic damage, but for knock-on damage lowering the kV below the displacement threshold does inhibit damage. For radiolytic materials, there is a suggestion that increasing the kV for thicker specimens does in fact improve the signal to damage ratio (Egerton, 2014).

Contamination is a serious issue for high-resolution analysis of organic materials,

especially in STEM. Since the vast majority of organics are carbon based, they can act as a source of hydrocarbons, which can result in contamination build-up even in the cleanest of electron beam columns. Baking samples can mitigate this to some degree. Heating a sample to below its melting point (typically 100 – 200 °C) under vacuum and leaving it for several hours, has the effect of causing absorbed contaminants on sample surfaces to be removed.

A popular technique for EM analysis of biological samples is cryo-EM, wherein samples are plunge frozen in liquid ethane to promote the formation of vitreous ice and then analysed in a TEM whilst cooled to liquid nitrogen temperatures (-180 °C) (Jensen, 2010). For biological samples, this technique is often a necessity, as it allows the observation of biological materials without staining or fixation, which can cause changes to samples. For biological and other sensitive samples, cryo-EM also provides a certain amount of protection from damage caused by the electron beam. This is due to a reduction in ambient thermal energy while at such low temperatures, meaning that more energy must be imparted by the beam electrons in order to break bonds or knock atoms out of place. Furthermore, it slows down both diffusion and reaction rates.

Charging effects are particularly prevalent in non-conductive samples when imaged with SEM. Enough charging can cause severe damage to samples, even in samples that are normally quite beam resistant. As such, non-conductive samples require coatings of conductive materials, usually gold or graphitised carbon before being analysed. Such coatings provide a low energy pathway for electrons absorbed by the sample to escape, reducing their potential to cause damage. Since charging effects in TEM are more limited, such coatings are often unnecessary, though this can depend on the morphology of the specimen (block of material versus a powder). Using highly

conductive TEM grid substrates has been shown to have some improvements to sample stability however, as well as reducing sample drift (Egerton, 2013).

2.4.8 – Monitoring Damage

A commonly used method for quantifying a material's sensitivity to the electron beam is the measurement of a critical fluence (C_F), assuming an exponential decay of structural features. This can be done in several ways (image diffraction or elemental/chemical signal), but the method used in this work will be to measure diffraction pattern spot intensities with respect to increasing beam exposure, graphing the results, and determining the total electron fluence at the point that the spot intensity falls to 1/e of its highest value. The units used here to express C_F are $e^-\text{Å}^{-2}$.

Material	Critical Fluence ($e^-\text{Å}^{-2}$)
C_{26} Paraffin	4
Anthracene	6
Phthalocyanine	125
Cu-Phthalocyanine	1560
Chlorinated Cu-Phthalocyanine	18750

Fig.2.16: Five values of C_F measured by electron diffraction spot intensity loss at 100 kV accelerating voltage. Reproduced from Egerton (2013) and with critical fluence values converted from $C\text{cm}^{-2}$ to $e^-\text{Å}^{-2}$. Original values from Reimer (1975).

Figure 2.16 shows a selection of C_F values determined for a variety of radiolytically sensitive organic materials. The larger, more complex molecule phthalocyanine has a much higher C_F than the comparatively simple C_{26} paraffin and anthracene, and its C_F can be increased further through metal doping and chlorination. This highlights the

great degree of variance in stability of these kinds of organics (and radiolytically sensitive inorganics, like zeolites, which can have C_F values ranging from several thousand to several tens of thousands of e$^-$Å^{-2} (Wang *et al.*, 2000)). Hence, the acquisition of a consistent C_F is a key starting point for EM work on such materials.

2.5 – Electron Microscopy of Beam Sensitive Crystalline Materials

2.5.1 – Theophylline

As discussed in section 2.1.2, TEM characterisation of individual theophylline crystals was key to the discovery of anhydrous polymorphs VI and VII (Eddleston, 2013 & 2015), a feat which would not have been possible for traditional bulk analysis techniques owing to the very low concentrations of these forms. Theophylline and other pharmaceutical materials were also investigated by Eddleston *et al.* (2010) with the aim of highlighting simple techniques for acquiring useable data from these notoriously beam-sensitive samples. EELS experiments on theophylline and other samples by Brydson *et al.* (2014) also showed that useable data can be obtained from these materials, but the analysis ran into the typical damage problems associated with beam sensitive materials. The sensitivity of theophylline requires that the electron flux is reduced significantly to prevent sample destruction, but this reduces SNR in the process, both for imaging and chemical analysis using EELS and EDX.

Little else in the way of EM analysis of theophylline has been performed, likely due to a combination of its sensitivity and lack of commercial interest, though the studies by Eddleston *et al.* (2010) did show that diffraction-based defect analysis of theophylline was possible. EM of sensitive organics is an expanding field owing to the improvements in equipment control and sensitivity, such as DED cameras and monochromators.

2.5.2 – Zeolites

EM of zeolites is a more widely explored area than organics, owing to the higher stability of zeolites under the electron beam. While still considered beam sensitive

when compared to typical inorganic materials, their C_F values are several orders of magnitude higher than those of most organics. Early experiments include those by Bursill *et al.* (1980) which investigated the effects of electron beam damage on the synthetic A-type zeolite. Defects and structural damage caused by the beam were successfully identified. Figure 2.17 shows some of the TEM micrographs obtained by Bursill *et al.* (1980), with defected areas and facets highlighted. Though electron flux was not stated, the authors noted that only one or two micrographs could be acquired before complete sample amorphisation, suggesting a relatively high flux for analysis of such beam sensitive materials.
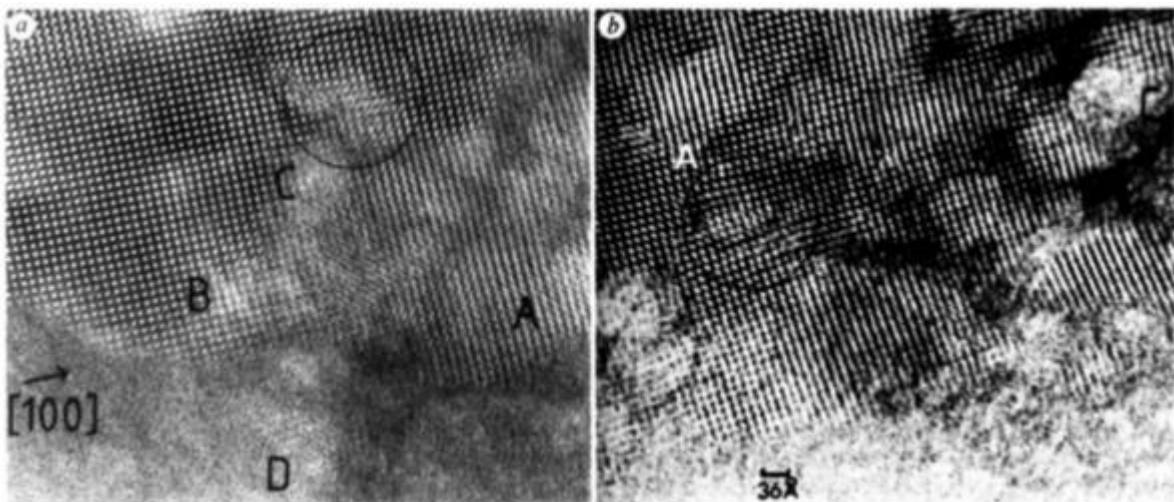
Fig.2.17: TEM micrographs of A-type zeolite showing defected areas (circled) and varying qualities of {100} fringes, where A denotes strong contrast in the fringes, B denotes weaker contrast, C denotes a complete lack of contrast, and D displays an island of fringes surrounded by amorphous material. Images from Bursill *et al.* (1980).

Treacy and Newsam (1987) investigated the sensitivity of zeolite L under the electron beam and outlined damage mechanisms for this zeolite in line with past observations on other materials, whereby the water content in the sample induced ionising damage to the atomic structure of the zeolite via radiolysis. Unlike beta zeolite, zeolite L still contains Al, and it is suggested that the overall negative charge of the structure due

to the presence of Al exacerbate damage effects.

Mayoral *et al.* (2015) used low fluence techniques to acquire atomic resolution images of a TiO_6 – SiO_4 zeolites. Figure 2.18 shows a schematic model of this zeolite crystal alongside a HAADF-STEM image of a TiO_6 – SiO_4 zeolite, again highlighting the possibility for high-resolution STEM imaging even at relatively low electron fluences. The electron fluence the specimens in this study were exposed to was ~1,000 $e^-Å^{-2}$, well below the C_F on most zeolites, though many times greater than the fluence needed to destroy most organics.
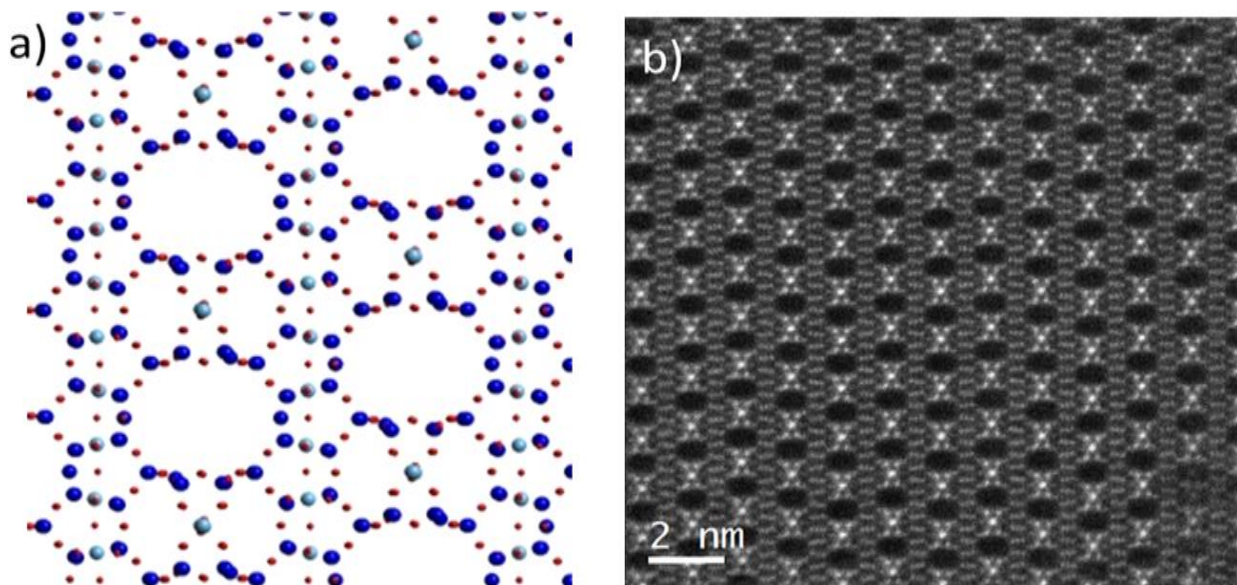
Fig.2.18: (a) Simulated atomic packing structure of the TiO_6 – SiO_4 zeolite. (b) HAADF-STEM image of the TiO_6 – SiO_4 zeolite. Some stacking faults are visible in the bottom right of the image. Images from Mayoral *et al.* (2015).

Electron microscopy was extensively used by Newsam *et al.* (1988) for the first EM analysis and detailed structural characterisation of beta zeolite. This uncovered the structure of beta zeolite as the intergrowth of the A and B polymorphs and shed light on the reasons for the difficulty in characterisation of this material by bulk techniques like XRD.

Wang *et al.* (2000) looked at three different zeolites to compare damage mechanisms in EM and found that pore size related to the C_F values of the materials, with the zeolites with larger pores being more stable (amorphisation fluence of 34,000 e$^-$Å^{-2} for zeolite-Y) compared to those with smaller pores (amorphisation fluence of 7,000 e$^-$Å^{-2} for analcime). This is explained as an effect of the radiolysis of the water held in the porous structure. In the systems with large pores, the water is able to quickly move and escape the irradiated area along with any radicals formed by interactions with the beam. This reduces the likelihood of a damaging interaction with the atomic structure of the zeolite. Based on these observations, in beta zeolite, for which the intergrowth of the polymorphs A and B causes a reduction in the size of the pores, damage could be expected to progress quicker in areas of higher polymorph intergrowth and defect concentration. Although the beta zeolite samples used in the experiments in this study are dried after synthesis, over time water could be readily reabsorbed back into the samples.

Much recent work that incorporates beta zeolite and EM techniques make use of EM as a simple way of characterising morphology following synthesis and post-synthesis experiments. Some groups have used EM techniques for the successful identification of single atoms incorporated into beta zeolite structures, such as Chai *et al.* (2018) who located Pb atoms in beta zeolite by HAADF-STEM. In combination with ultraviolet-visible spectroscopy, X-ray photoelectron spectroscopy, and NMR spectroscopy, they were also able to determine the ionic state of the Pb as Pb^{2+}, present as an open tetrahedral site within the zeolite structure, though the exact T-site occupancy of the Pb was not determined.

2.5.3 – Other Materials

There have been a number of previous TEM experiments performed on a wide variety of organic crystalline materials, including theophylline and its polymorphs and cocrystals. Cryo-EM has long been used for the analysis of biological materials and many of these studies have included the analysis of crystallised biological proteins. Early examples of such studies include the works of Taylor and Glaeser (1974,1976), and Unwin and Henderson (1975) who used electron microscopy to produce diffraction patterns (DP) of crystallised catalase and purple membrane respectively. These examples highlighted the great potential for EM to be used for high-resolution ED analysis (<10 Å) of beam sensitive materials. They also highlighted many of the limiting factors and extra sample preparation steps that needed to be undertaken in order to achieve such resolutions.
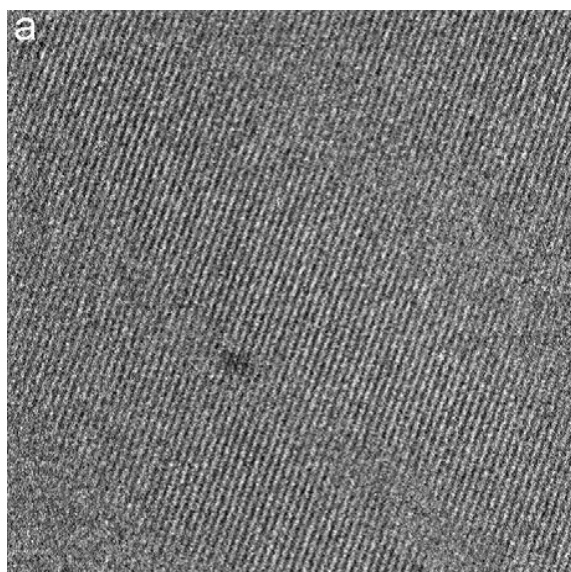
Fig.2.19: Lattice image of a paraffin crystal acquired using low fluence, aberration-corrected cryo-EM. Spacings measured at 0.2 nm. Image under-focussed by 36 nm in order to improve phase contrast. Image from Evans *et al.* (2008).

Cryo-EM has since evolved and is now regularly used for the 3D reconstruction of large protein complexes (Armache *et al.*, 2010; Chang *et al.*, 2006). Cryo-EM also

48

sees use during analysis of other beam sensitive materials, as it improves damage resistance in such samples. Evans *et al.* (2008) used cryo-TEM in order to improve the stability of the paraffin sample they were analysing just enough to acquire lattice images (figure 2.19). The paraffin displayed critical fluences (total electron fluence needed to cause reduction in diffraction spot intensity to fall to $\frac{1}{e}$ the initial intensity) of 5 – 10 e⁻Å^{-2} at room temperature, or 20 e⁻Å^{-2} at liquid nitrogen temperature. Though successful in their attempts, the authors did note that successfully captured lattice images were difficult to obtain, owing to the sensitivity of their experimental parameters and samples.
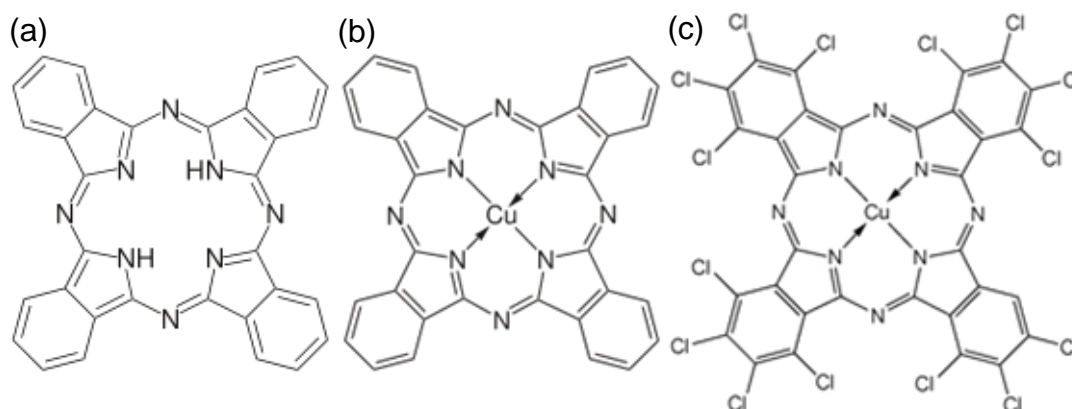
Fig.2.20: Molecular structures of (a) phthalocyanine, (b) copper(II) phthalocyanine, and (c) chlorinated copper(II) phthalocyanine.

Though a great many organic crystalline materials are highly sensitive to the electron beam, there are a few examples of materials which are much more resistant to damage than most. Examples of such materials include the phthalocyanine family. Phthalocyanines are discotic liquid crystals which can form coordination complexes with many elements. These complexes are commonly used as dyes owing to their vibrant colours and high stabilities. Figure 2.20 shows the molecular structures of phthalocyanine and two of its variants.

There are a great number of phthalocyanine polymorphs, with thin crystals being easily produced by multiple methods (Lewis *et al.*, 2001). Phthalocyanines are notable for their high stability under the electron beam compared to other organic materials, so much so that lattice images of metal phthalocyanines were being produced in the 1980s (Kobayashi *et al.*, 1982). Stability experiments from around the same time provide critical fluence values for certain phthalocyanine complexes (copper phthalocyanine in this case) as well as its chlorinated variant.
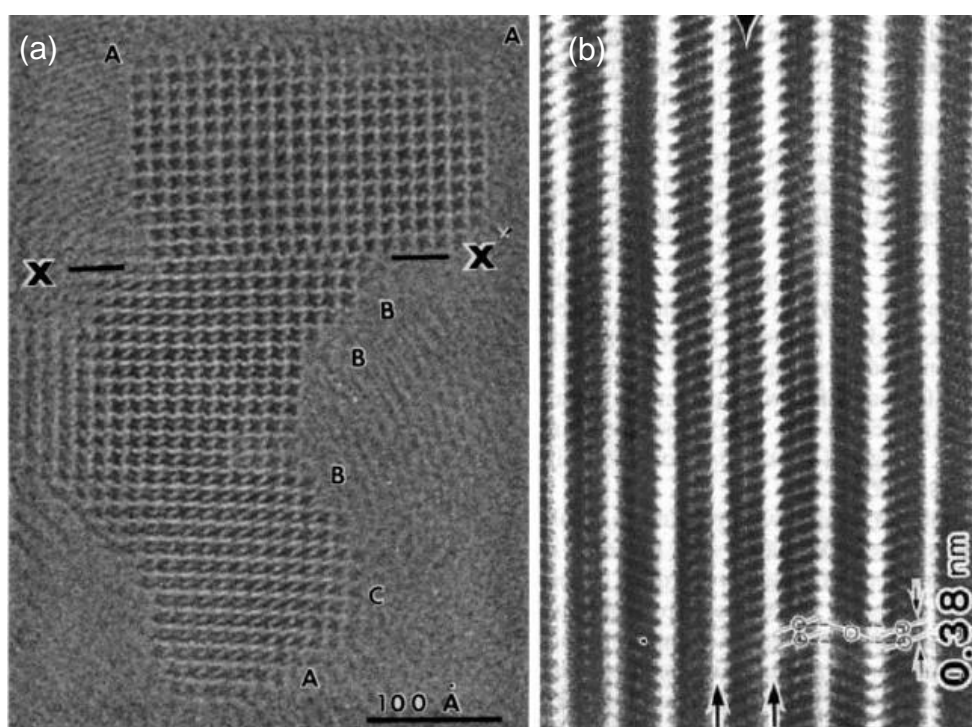
Fig.2.21: (a) Lattice image of platinum phthalocyanine. The dark X-like structures are individual molecular stacks. Region XX' is a grain boundary, hence the lattice mismatch. Regions marked A, B, and C highlight regions of low contrast due to molecules having been ejected. This occurs mostly at corners (A), kink defect sites (B), and crystal edges (C) where molecules are only weakly bound to the bulk. Image from Kobayashi *et al.* (1982). (b) Lattice image of zinc phthalocyanine. Individual molecular stacks are visible, as well as the herringbone structure of this crystal. Through typically an ABAB type structure, the marked column is incorrectly oriented. Image from Kobayashi *et al.* (1993).

Clark *et al.* (1980) performed stability tests on copper phthalocyanine and its

chlorinated derivatives and compared its stability to other studies of the time. A typical value for the C_F of diffraction spots of copper phthalocyanine was ~940 $e^-Å^{-2}$. Already many times higher than the C_F values for paraffin (Evans *et al.*, 2008), the C_F is heightened further when the chlorinated copper phthalocyanine is analysed, with diffraction spots fading after ~15,000 $e^-Å^{-2}$. Other papers reported C_F values more than double this value, depending on the material form and experimental conditions (Clark *et al.*, 1980).

Such is the stability of metal phthalocyanines that lattice images are relatively easily obtained. Figure 2.21 shows lattice images of platinum phthalocyanine and zinc phthalocyanine. Though useful materials to investigate (potentially as a model material for analysis of defects in other organic materials, due to their relatively high extinction fluences) phthalocyanines are not representative of the majority of organic crystalline materials and their interactions with an electron beam. Figure 2.21 also shows high-resolution TEM micrographs of platinum phthalocyanine, allowing for defect analysis of the crystalline lattice (observation of stacking faults and mass loss).

STEM has seen increased use in recent years for the analysis of sensitive organic materials. Sader *et al.* (2010) compared low fluence TEM and STEM imaging performances on samples of vermiculite (a relatively beam sensitive silicious mineral). Although the STEM used in this case was not optimised for low fluence analysis, it was found that the image contrast was improved compared to TEM, but at the cost of SNR. The authors go on to suggest that, with both optimisation of collection criteria and cameras, and with the addition of aberration correctors, STEM may yet prove to be an important method for beam sensitive materials analysis. They also suggest that, due to the smaller scanning areas usually used for STEM, sample drift will be minimised, owing to the smaller damaged area and surrounding pristine sample acting

as a physical barrier to movement.

Low fluence STEM techniques have only recently been properly investigated, owing to the complexity of applying low fluence beam conditions. Initial studies, such as those by Buban et $al.$ (2010), showed low fluence STEM as capable of imaging at ~15 $e^-Å^{-2}$ while obtaining a resolution of 2.8 Å. However, the authors note that many imaging artefacts were also introduced as a result of the imaging conditions and variable scan speeds, including scan line smearing and offset. Additionally, these investigations were performed on beam damage resistant $SrTiO_3$, so the effects of sample damage would not be readily apparent in these studies.
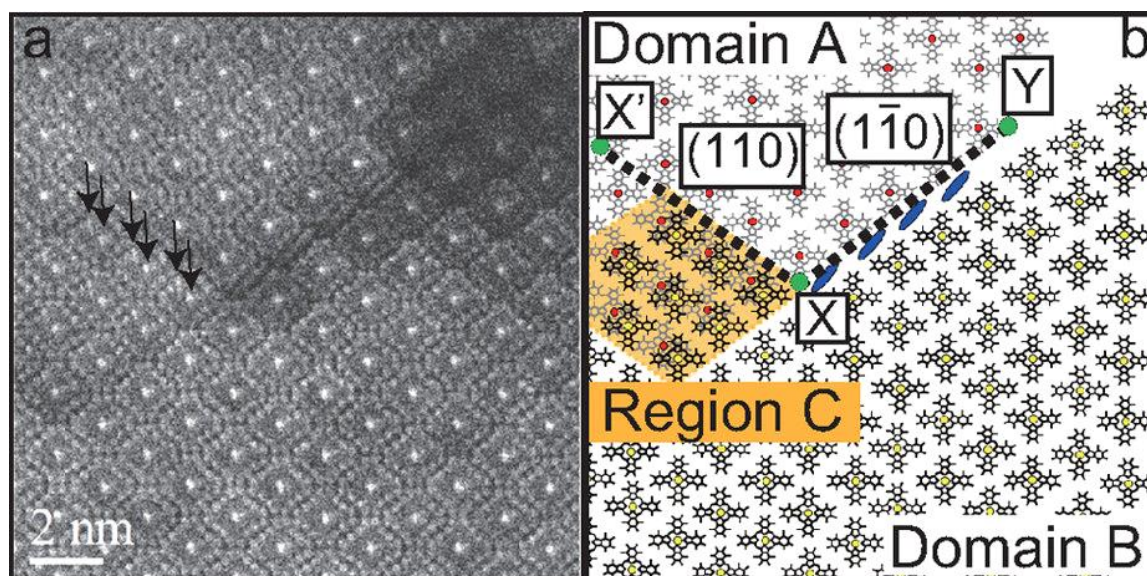
Fig.2.22: (a) LAADF-STEM image of a thin film of chlorinated copper phthalocyanine. Areas of different contrast are indicative of different film thicknesses and defects. Arrows indicate stacking faults. (b) Schematic of the region shown in (a), highlighting the grain boundaries by dashed-lines, misaligned molecules along the XY grain boundary (blue ellipses) and region C shows the area of stacking faults. Image from Haruta & Kurata (2012).

Haruta and Kurata (2012) used an optimised STEM setup combined with low fluence imaging methods to acquire high-resolution, low-angle annular dark-field images (LAADF) of a chlorinated copper phthalocyanine thin film. Figure 2.22 shows one of

these images as well as a schematic diagram of the same area, highlighting lattice defects and molecular stacks. Such observations are the ideal goal for our own studies, though in this case, the critical fluence of the sample is many times higher than the critical doses (~10 e$^-$Å^{-2} for a compound like theophylline compared to ~15,000 e$^-$Å^{-2} for the chlorinated copper phthalocyanine), so achieving lower fluences in STEM may still present a challenge.
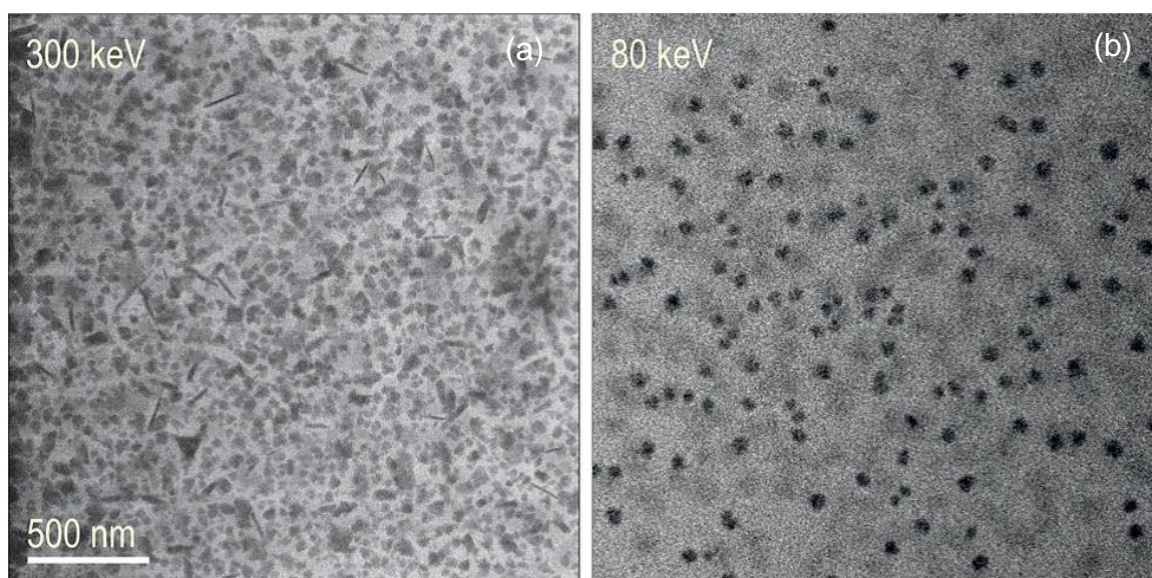
Fig.2.23: Silver nanoparticles produced at (a) 300 keV and (b) 80 keV. Imaging areas and other beam conditions in both images are identical. Images from Abellán *et al.* (2014).

Liquid cell TEM is inherently beam sensitive owing to the radiolytic sensitivity of water to ionisation. Abellán *et al.* (2014) used low fluence STEM techniques to analyse liquid samples and *in situ* growth of silver nanoparticles, silica nanoparticles, and zeolites. The low fluence conditions they used allowed them to achieve fluence rates of ~0.2 e$^-$Å^{-2} per frame. Their results showed the effects of damage and particle nucleation as well as their relationships with various experimental parameters, such as fluence rate, scan rate, imaging mode, beam voltage, and beam spread. One such set of results are shown in figure 2.23, which shows the difference between silver nanoparticles grown *in situ* using both a 300 keV and an 80 keV electron beam. The nanoparticle

53

morphologies in each experiment are distinctly different, with needles, triangular plates and cubes produced at 300 keV and denser, spherical particles which are fewer in number produced at 80 keV. The authors suggest this may be due to increased radical production in the aqueous solvent at 80 keV causing inhibition of crystal nucleation and growth, although they highlight the need for further investigation into these effects. While the exact damage and growth effects will not directly translate between liquid and solid samples, this study highlights the importance of beam conditions in both STEM and TEM.

2.6 – Summary and Going Forwards

Material	Critical Fluence / e⁻Å⁻²	Method	Conditions	Information obtained	Source
Efavirenz	0.3	BF-TEM	200 kV, low flux	Diffraction patterns	S'ari *et al*, 2015
Paraffin	4	Cryo-EM	200 kV, low flux, thin single crystals, aberration correction, liquid N temperature, micrograph post-processing	Diffraction patterns, lattice images	Evans *et al*, 2008
Copper phthalocyanine	940	BF-TEM	100 kV, low flux	Diffraction patterns	Clark *et al*, 1980
Analcime	7,000	HAADF-STEM	300 kV, aberration correction, 16 nA beam current	Diffraction patterns, lattice images	Mayoral *et al*, 2015

Fig.2.24: Table comparing four beam sensitive materials by their critical fluences, techniques used to characterise them, and the information obtained from these studies.

The literature presented highlights the difficulties facing EM characterisation of electron beam sensitive organic and inorganic specimens, but also shows that such characterisation is possible even to atomic resolution. There remains a need to develop consistent low fluence techniques for high-resolution EM analysis of highly beam sensitive organic materials, as well as beam sensitive inorganic materials like zeolites. Figure 2.24 shows a table comparing four beam sensitive materials, the

information that has been acquired from them, and the conditions used to obtain that information. To summarize the table's contents in general terms, the more sensitive a material the more time consuming and complex methods and conditions will need to be used to acquire the same information as from a less sensitive sample. In the cases of paraffin and analcime, more stringent conditions were implemented to obtain the lattice images, while for efavirenz and copper-phthalocyanine, relatively simple conditions were utilised for acquisition of diffraction patterns primarily. The difficulty of characterising these materials with EM means that even with the more in-depth experimental conditions as with paraffin, there is no guarantee that a lattice image of efavirenz could be acquired this way.

The literature available suggests that BF-EM is likely to yield the most successful imaging at low fluence given the efficiency of electron collection for this technique. There is a suggestion that BF-STEM may be equal to or even outperform BF-TEM. The main aim of this thesis therefore is to demonstrate that BF-TEM and STEM techniques can be applied to characterise the structure of organic compounds and other samples sensitive to radiolytic damage.

Key to this will be an overall experimental approach that will follow these guidelines:

1. Concentrate BF techniques that make efficient collection of scattered electrons.

2. Lower the intensity of the electron flux, which requires control of the electron source.

3. If further stabilisation is required, increase the accelerating voltage, especially if the sample is thick.

4. Cool the specimen to mitigate damage progression.

5. Use a conductive specimen substrate to mitigate charge build-up and

associated damage effects.

Two materials, an organic crystalline material, theophylline form II, and an inorganic crystalline material, Sn-beta zeolite, will be used as model materials to explore low fluence EM. This then gives three specific research objectives:

1. Measurement of lifetime of theophylline form II under high-energy electron irradiation plus identification of operating and specimen conditions that may extend lifetimes.

2. Determination of appropriate electron microscopy methods to image the atomic lattice of theophylline form II.

3. Determination of appropriate electron microscopy methods for the characterisation of Sn-beta zeolite structure and chemistry.

Chapter 3 – Materials and Methods

3.1 – Material Sources and Sample Preparation

Raw theophylline form II powder (≥99 % purity) was sourced from Sigma-Aldrich Co. Crystals presented needle-like morphologies. To acquire the large, flat, triangular crystal morphologies desired, a saturated solution was produced by slowly adding theophylline to continuously stirred and heated (~50 °C) nitromethane until saturation was achieved. The solution was then allowed to cool. Depositing a droplet of this solution on to a substrate surface and allowing the nitromethane to evaporate causes the crystallisation of the desired morphology of theophylline form II crystals.

Zeolite samples were provided by Haldor Topsøe A/S researchers Søren Tolborg, Esben Taarning, and Stig Helveg. These included one Si-beta and two Sn-beta samples, with the Sn-beta samples differing in their synthesis methodology. The synthesis procedures for the Si-beta and the first Sn-beta sample (prepared via hydrothermal synthesis) are outlined in Tolborg *et al.* (2014). The synthesis method for the second Sn-beta sample (via solid-state ion-exchange) is outlined in Tolborg *et al.* (2015).

Individual samples were kept in labelled glass and plastic bottles. These were kept in a sealed plastic container placed in a cupboard in a sample preparation laboratory when not in use. This laboratory was maintained at room temperature (~20 °C) and pressure was assumed to be ~1 atm.

Solvents nitromethane (≥95 % purity) and ethanol (96 % purity) were purchased from Sigma-Aldrich Co and VWR International respectively and used as provided. These were stored in a solvent locker located in the same laboratory as the above samples.

3.2 – Characterisation Techniques and Sample Preparations

3.2.1 – X-ray Diffraction

Experimental X-ray diffraction (XRD) patterns were acquired using a PANalytical XPERT diffractometer using copper Kα radiation (λ = 1.541 Å). Powder samples were flattened into a plastic sample plate and scanned at a step size of 0.0025° 2θ, in the 5 to 30° 2θ angle range over 10 minutes.

Simulated XRD patterns were created using the CrystalMaker and CrystalDiffract software packages (*http://crystalmaker.com*). Crystallographic information files (.cif) containing structural information for various forms of theophylline were obtained from the Cambridge Structural Database (CCDC) for use in conjunction with the software. The CCDC references for the cif files used and the structures they describe are as follows: theophylline monohydrate (CCDC reference: 1270454), theophylline anhydrous form I (CCDC reference: 862238), theophylline anhydrous form II (CCDC reference: 878133), theophylline anhydrous form IV (CCDC reference: 862237).

3.2.2 – Scanning Electron Microscopy

SEM was carried out on a Hitachi SU8230 cold field emission microscope, operated with a 1 kV beam voltage, and with the detector in low-energy secondary electron detection mode. The low beam voltage was attained using the microscope's deceleration mode, wherein a negative bias is applied to the sample stage, causing electrons exiting the microscope column to be decelerated before they reach the sample. This has multiple effects. The decelerating field between the end of the column and the sample acts as an immersion converging lens, further focussing the beam before it reaches the sample, resulting in improved resolution. Signal electrons

escaping the sample are accelerated towards grounded regions of the specimen chamber (*i.e.* the detectors). This effect increases signal collection efficiency (Phifer *et al.*, 2009).

SEM samples were prepared by drop casting a theophylline saturated nitromethane solution directly onto aluminium stubs. The stubs were heated to ~70 $^{\circ}$C to accelerate evaporation of the nitromethane. Form II theophylline crystals formed as this occurred. Once dry, a Quorum Technologies Ltd. QT150E carbon coater was used to apply an amorphous carbon coat roughly 5 nm thick to each sample stub. This coating reduces the effects of charge build-up in the specimen by conducting away electrons captured by the specimen.

3.2.3 – Conventional Transmission Electron Microscopy

CTEM is a material characterisation method similar to SEM but utilising a higher energy electron beam, typically 100 – 300 keV. As such, the electron beam has sufficient energy to penetrate the entirety of thin samples, producing electron micrographs that represent the sample microstructure as a 2D projection. Additionally, the electron beam is spread to illuminate the target sample area in its entirety and with a near-parallel beam, rather than through the use of a highly focused and converged rastered beam. Direct atomic imaging is commonplace using modern TEM systems, though the magnification range in most microscopes is wide enough that low magnification images of large specimen areas can be acquired alongside ultra high-resolution images. Figure 3.1 shows a schematic of a CTEM column showing the electron beam path, lenses, sample location, and detectors.

The resolution of any microscope is fundamentally limited by the wavelength of the

waves used, be they light or sub-atomic particles. This limit is approximated by the Abbe equation: $d = \frac{\lambda}{2nsin\theta}$, where d is the size of the smallest resolvable feature, λ is the wavelength of the beam components, n is the refractive index of the medium the beam travels through (1 for vacuum), and θ is the lens collection semi-angle. The quantity $nsin\theta$ is also known as the numerical aperture (NA). For a collection semi-angle of 10 mrads, the NA is 0.01. The relationship between λ and d is such that *d* is roughly $\frac{\lambda}{2}$. For comparison, using OM (light wavelengths between ~400 nm and ~700 nm), results in a maximum possible resolution of about 200 nm, well below the resolution needed to observe individual atoms.

The wavelength of electrons depends on their energy, *E*. These are related by the de Broglie equation: $\lambda = \frac{1.22}{E^{1/2}}$. So, for a TEM operating at 100 keV accelerating voltage, the wavelength of the electrons would be ~0.0038 nm, and the maximum possible resolution therefore being ~0.0019 nm, well below the resolution needed to observe individual atoms. (Williams & Carter, 2009). In practice, resolution is limited by lens aberration effects.

CTEM was primarily carried out on an FEI Tecnai TF20 field emission gun microscope, with an attached Gatan Orius SC600A CCD camera. This was operated between 80 and 200 kV accelerating voltage as required, with a tip extraction voltage of 4.5 kV. Electron fluence rates were maintained in the region of 0.05 to 0.1 e$^-$Å^{-2}s^{-1} by manipulating beam spread and C1 lens excitation. For the theophylline critical fluence experiments, initial 300 kV CTEM was carried out at the University of Sheffield on a JEOL R005 cold field emission gun microscope with an attached Gatan Orius SC200 CCD camera. All other 300 kV CTEM experiments were carried out on a Titan[3] Themis 300 field emission gun microscope at the University of Leeds. The Titan[3] Themis 300

has a super-twin objective lens with a C_s of 1.3 mm and a quoted point resolution of ≤0.2 nm and an information limit at or better than 0.1 nm. The STEM resolution has been checked by an installation engineer to be 0.136 nm and was done by measuring a particular spacing in silicon by STEM HAADF imaging.
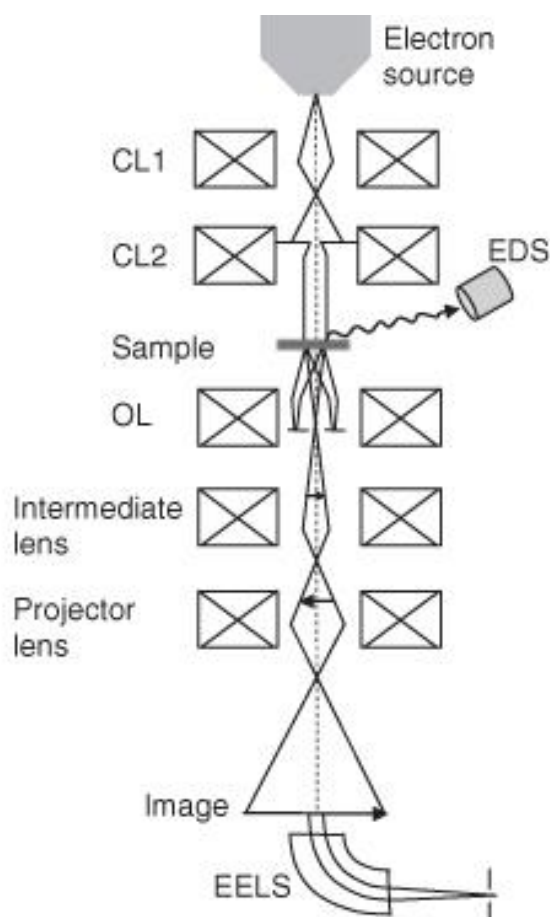
Fig.3.1: Schematic of a TEM column showing the path of the electron beam as well as the CLs, OLs, and the EDS and EELS detectors. Image from Bell & Erdman (2012).

Samples were prepared by drop casting a theophylline saturated nitromethane solution directly onto carbon coated copper TEM sample grids placed on a glass slide. The grids were heated to ~70 °C to accelerate evaporation of the nitromethane. Form II theophylline crystals formed as this occurred.

A number of different TEM sample grids were used. For most experiments, lacey carbon film copper grids were used (Agar Scientific, AGS166-4). Other grids used

include chemical vapour deposited graphene on lacey carbon (Graphene Supermarket, SKU-TEM-CLC-025), C-flat holey carbon film (Protochips, Inc., CF242), continuous carbon, and ultrathin (<3 nm) carbon (Agar Scientific, AG01824G).

3.2.4 – Energy Dispersive X-ray Spectroscopy

EDX spectroscopy is a material characterisation technique used for spatially resolved elemental analysis. In electron microscopy, X-rays are a by-product of interactions between the electron beam and the sample. In the production of secondary electrons, whereby incident electrons ionise electrons from the inner shells of atoms in the sample, holes are left where ionised electrons are ejected. Of the two major mechanisms that can occur to fill the hole, one is that an electron from a higher energy state decreases in energy to take the position of the ejected electron, expelling the excess energy in the form of a fluorescent X-ray. This X-ray has energy characteristic of the energetic states involved in this event and hence the specific element. Through collection and energetic or wavelength analysis of these X-rays, it is possible to determine the elemental composition of a sample area.

An alternative de-excitation mechanism is Auger electron emission, whereby the energy expelled by the electron filling a vacancy is transferred to another electron which is subsequently ejected. These electrons also have discrete energies characteristic of the type of atom and chemical environment they were produced from and can also be used for spectroscopy. This mechanism is more common in low Z elements.

EDX spectroscopy was carried out during TEM and SEM experiments. The Titan[3] Themis 300, used for CTEM and STEM experiments, came with an attached FEI

Super-X 4-detector EDX system. The Hitachi SU8230 SEM utilises a Oxford Instruments Aztec Energy EDX system with 80mm X-Max SDD detector. No special sample preparation techniques were used specifically with EDX in mind (see sections 3.2.2 and 3.2.3 for SEM and CTEM sample preparation techniques respectively).

3.2.5 – Scanning Transmission Electron Microscopy (STEM)

The imaging modes utilised for STEM analysis were bright-field (BF), high-angle annular dark-field (HAADF), and integrated differential phase contrast (iDPC). The conditions used for BF-STEM imaging were 300 kV accelerating voltage, 20 μs dwell time, 5 pA beam current, and 10 mrad probe convergence semi-angle (α). The convergence semi-angle gives a probe size of 1.4 Å. With a BF collection semi-angle (β) of 7 mrad and at a camera length of 460 mm, conditions are met for good phase contrast collection efficiency for an uncorrected STEM, as given in the literature (Sader *et al.*, 2010). Ideally, β would be equal to half of α, but as β is tied to camera length, which has set values, a β of 7 mrad is as close as could be achieved. These conditions were also utilised for HAADF and iDPC imaging, with the exception of camera length, for which a setting of 90 mm was used for HAADF imaging.

STEM was carried out on a Titan[3] Themis 300 field emission gun microscope, operated at 300 kV accelerating voltage. A monochromator was used to maintain beam current in the region of 1 to 5 pA.

An illustration of what is possible with the Titan using STEM at a low beam current (1 pA) is demonstrated by BF-STEM imaging of a calcite nanoparticle (figure 3.2). 1.6 Å fringes are resolved by FFT at a total electron fluence of 170 e$^-$Å^{-2} (data supplied by Robert Hooley, PhD student, University of Leeds). The STEM has been demonstrated

to resolve 1.4 Å spacings by HAADF imaging with a 70 pA probe.
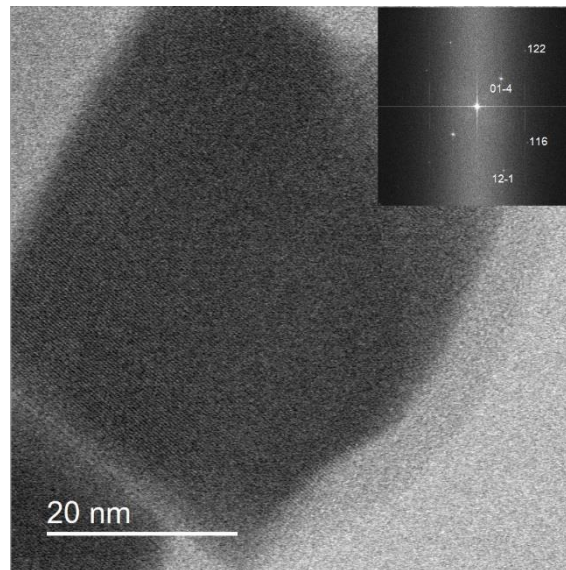
Fig.3.2: Calcite nanoparticles imaged with 1 pA probe in the Titan[3] Themis 300. A 1.6 Å calcite (122) d-spacing is resolved. Image from R Hooley, University of Leeds.

3.3 – Measurements of Critical Fluences of Theophylline Form II as a Function of Electron Beam and Sample Conditions

3.3.1 – Measuring Critical Fluence from Time Resolved Diffraction Pattern Series

Critical fluence was measured using the [100] diffraction pattern of theophylline form II. The intensities of {011} spots in this pattern were measured as a function of time exposed to the electron beam *i.e.* accumulated electron fluence. Figure 3.3 shows a flow chart of the process used to acquire these diffraction pattern series in a consistent manner using the FEI Tecnai TF20 electron microscope.
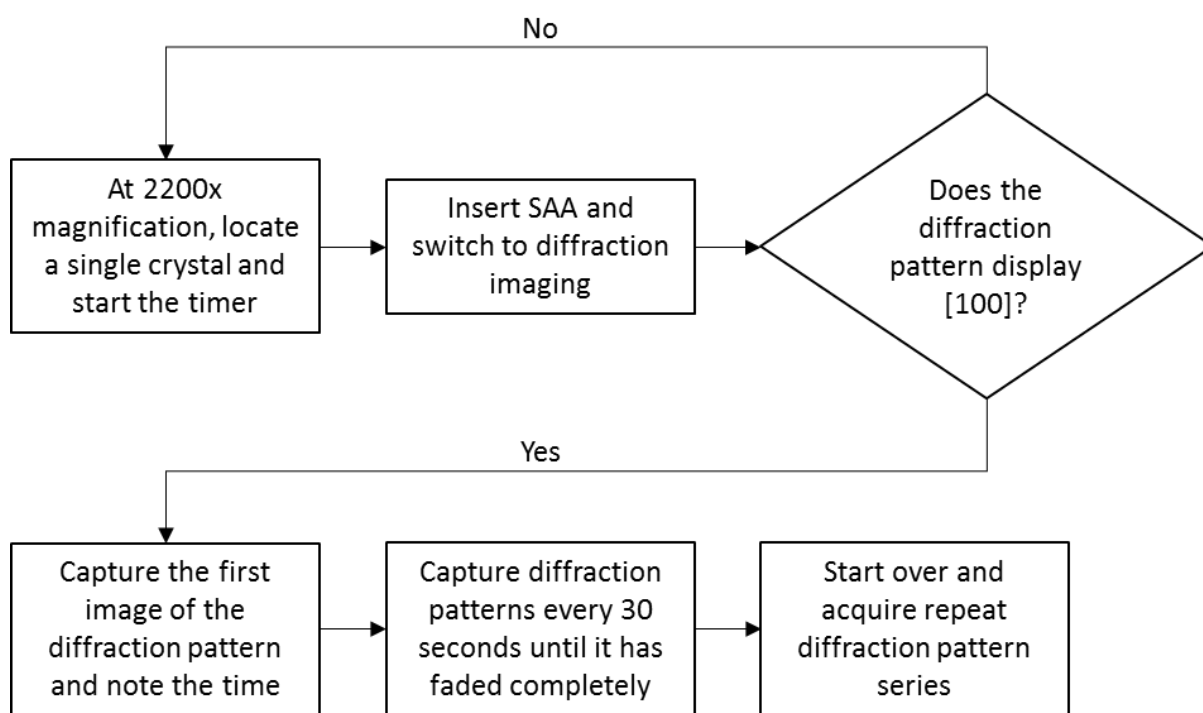
Fig.3.3: Flow chart outlining the process of diffraction pattern series acquisition using the FEI Tecnai TF20 electron microscope. The time after initial beam exposure for acquisition of the first diffraction pattern was usually between 10 and 30 seconds.

The repeats of these measurements were mean averaged and plotted against total accumulated electron fluence. A critical fluence was read off these plots at $\frac{1}{e}$ (37 %) of the maximum normalised spot intensity. This was done for theophylline form II under

66

each of the conditions noted in section 3.3.2, such that critical fluences could be compared, and the effects of changing conditions on the stability of theophylline form II under the electron beam analysed.

3.3.2 – Standard CTEM Conditions and Electron Fluence Calculations

Diffraction patterns acquired during TEM experiments were used to determine the critical fluence values of theophylline form II under a number of microscope and sample conditions. The standard conditions used were as follows: 200 kV accelerating voltage, room temperature, and with samples supported on continuous carbon film substrate grids. Variations to these conditions were made to investigate their impact on critical fluence, and were as follows: 80 kV accelerating voltage, 300 kV accelerating voltage, 93 K temperature, 173 K temperature, 423 K temperature, and use of graphene film substrate grids.

The units used to measure electron fluence are $e^-Å^{-2}$ *i.e.* the number of electrons that have passed through a unit area of the sample. Adding a time dependency to fluence gives electron flux ($e^-Å^{-2}s^{-1}$).

Variables that affect fluence and flux include (standard settings given in parentheses):

- Emission current (~80 µA) and field emission extraction voltage (4.125 kV)
- Spot size *i.e.* condenser 1 (setting 5)
- Specimen illumination area *i.e.* condenser 2 (diameter of 4,200 µm^2)
- Second condenser aperture size (150 µm diameter)

Each of these variables affects the flux in the following ways:

- Altering extraction voltage in turn affects emission current, which alters the raw

number of electrons being extracted from the tip in a given time. Increasing either parameter will increase electron flux.

- Spot size determines the degree of demagnification the source beam undergoes as it passes through the first condenser lens in the microscope column. A larger spot size will let more electrons through, providing more signal and a brighter image *i.e.* higher electron flux.

- Illumination area (second condenser lens effectiveness) determines how widely the beam is spread over the sample. A smaller illumination area will improve SNR but will also increase electron flux in the illuminated area.

- The size of the second condenser aperture determines the convergence angle for electrons being directed down the microscope column. A larger aperture will allow more electrons through, increasing image brightness at the cost of SNR and increased electron flux.

Changing electron flux can have an effect on damage mechanisms in beam sensitive materials. For consistency in these experiments, all of the above variables were kept constant. Though beyond the scope of this work, the effects of changing electron flux are known to affect the decay rate of certain materials, so could be investigated further in future.

Though these variables were kept constant, the flux itself was not constant. The age of the electron source and how long it has been since it has been replaced or flashed to remove contaminants can greatly affect the electron flux. As such, flux and fluence needed to be calculated for each session during which DP series were acquired. This was achieved by monitoring the exposure time (t_e) reading of the microscope's fluorescent screen and the use of the calibration measurement. The following equations were used to do this for the Tecnai-F20 microscope (equations provided by

FEI). Initially, the electron density, I, must be calculated:

$$(3.1) \quad I(e^-s^{-1}) = \frac{1875 \times 10^{-12} \times BSD \times \varepsilon}{t_e \times C_s \times 1.6 \times 10^{-19}}$$

In this equation, the BSD factor is dependent on the accelerating voltage (1.3 for 200 kV or 1.1 for 80 kV). ε represents the emulsion setting of the fluorescent screen (set to 2 while operating the TEM). t_e is the exposure time as determined by the fluorescent screen. C_s is the fluorescent screen correction factor (≡ 1.2 for TF20 microscope used).

From the electron density value, the electron flux, J, can be calculated by the following equation:

$$(3.2) \quad J(e^-m^{-2}s^{-1}) = \frac{I}{\pi r^2} \times M^2$$

Here, r represents the radius of the electron beam spread as it appears on the fluorescent viewing screen (0.08 m for the standard 4,200 µm^2 specimen illumination area used). M here is the magnification (with the fluorescent screen raised).

For example, if we use the standard conditions outlined earlier and a typical exposure time of 0.5 s:

$$(3.3) \quad I = \frac{1875 \times 10^{-12} \times 1.3 \times 2}{0.5 \times 1.2 \times 1.6 \times 10^{-19}} = 5.08 \times 10^{10} \ e^-s^{-1}$$

For the diffraction analysis of theophylline, 2.5k times magnification was used, with the electron beam spread over the entire fluorescent screen (diameter 160 mm). From this we can calculate the electron flux:

$$(3.4) \quad J = \frac{5.08 \times 10^{10}}{\pi \times 0.08^2} \times 2500^2 = 1.58 \times 10^{19} \ e^-m^{-2}s^{-1}$$

Converting to e$^-$Å^{-2}s^{-1} gives:

$$0.158 \, e^{-}\text{Å}^{-2}s^{-1}$$

The JEOL R005 microscope used for initial 300 kV imaging of theophylline form II does not make use of the FEI calibration calculations previously outlined. Instead, it used a Faraday cup to give a direct reading of current density in pA per cm^2 (for a beam spread over a 2.6 cm diameter fluorescent screen). This could be converted to electron fluence in the illuminated sample area. Based on the number of electrons in 1 Coulomb (6.25 x 10^{18}), where 1 C/s is 1 A:

$$1 \, pA \, cm^{-2} = 6.25 \times 10^6 \, e^{-} cm^{-2}s^{-1}$$

For a fluorescent screen of diameter 2.6 cm and area 5.31 cm^2, with 2.8 pA/cm^2 current density (typical values for experiments undertaken):

$$2.8 \, pA \, cm^{-2} = 1.75 \times 10^7 \, e^{-} cm^{-2}s^{-1}$$

Therefore, the current density for the entire electron beam is:

$$9.29 \times 10^7 \, e^{-}s^{-1}$$

We can now apply this value to the sample area illuminated by the beam to obtain an electron flux value. 25k times magnification was typically used. Based on the screen illumination diameter of 2.6 cm, the sample illumination diameter is:

$$\frac{0.026}{25000} = 1.04 \times 10^{-6} \, m \, (so \, radius = 0.52 \times 10^{-7} m)$$

Therefore, the sample illumination area is:

$$\pi \times (5.2 \times 10^{-7})^2 = 8.49 \times 10^7 \, \text{Å}^2$$

Dividing the current density by the illuminated sample area gives an electron flux of:

$$9.29 \times 10^7 / 8.49 \times 10^7 = 1.09 \, e^{-}\text{Å}^{-2}s^{-1}$$

3.4 – High-resolution Analysis of Theophylline Form II

3.4.1 – Bright-Field Scanning Transmission Electron Microscopy

Low-dose BF-STEM was used in attempts to directly image the crystalline lattices of theophylline form II. Samples were prepared as per CTEM specimens in 3.2.3, and the monochromator on the Titan[3] Themis was used to reduce the current of the beam down to ~1 pA. In STEM, electron flux is directly linked to magnification since higher magnification is achieved by reducing the scan area of the beam. Since current is not lowered to compensate, increasing magnification increases electron flux. This sets a limit on the magnification that can be used to observe sensitive samples such as theophylline based on their critical fluences. In the case of theophylline form II, its critical fluence was determined to be ~30 e$^-$Å^{-2} from the experiments detailed in 3.3.

3.4.2 – Scanning Moiré Fringes

Moiré fringes of theophylline form II were acquired by first orienting a chosen crystal in CTEM. The diffraction spots representative of the desired lattice spacings ({011} in this case) were rotated until perpendicular to the STEM scan direction in order to bring β as close to 0° as possible. Then, in BF-STEM mode, the magnification was set to 225k times, such that the pixel size (and therefore spacing size of the scanned lattice) was 0.329 nm. This is the closest match available to the size of the {011} lattice of theophylline form II, which has a spacing size of 0.341 nm. Assuming a β of 0° is obtained, moiré fringes of 9.34 nm spacing would be expected.

3.5 – High-resolution Analysis of Si-beta and Sn-beta Zeolites

3.5.1 – EM, iDPC, and HAADF

Zeolite samples provided by Haldor Topsøe A/S were subject to a number of high-resolution experiments in the Titan[3] Themis 300, with the main aim being the identification of Sn atom sites in the Sn-beta samples and corresponding proof that such sites were not also visible in the tin free Si-beta zeolite.

SEM was initially carried out on the samples to assess dispersion properties and surface features, which would inform TEM sample preparation methods and analysis targets. Samples were prepared by dispersing zeolite powder in ethanol, mixing, and then drop casting the resulting dispersion onto aluminium sample stubs. A carbon coating was then applied to samples using a Quorum Technologies Ltd. QT150E carbon coater. Samples were prone to charging under the electron beam, so were analysed between 1 and 2 kV in deceleration mode, in SE detection mode.

Based on the results, it was decided that most intact zeolite particles were too large (>1 µm) to be transparent for TEM analysis. Sonication was performed on the sample suspensions in order to break up the large crystals. Zeolite dispersions were sonicated for 10 minutes each prior to sample preparation. This was carried out in a VWR USC 300 TH ultrasonic cleaner. After sonication, samples were prepared by drop casting a single droplet of suspension onto a glass slide mounted lacey carbon grid. These were then heated to ~70°C to evaporate the ethanol and cause the zeolite crystals to deposit onto the TEM grid.

The experiments carried out in the Titan[3] had several distinct stages. Firstly, CTEM was performed in order to locate regions of zeolite crystals thin enough to be electron transparent. The diffraction patterns of these areas were then observed, and

alterations made to the tilt angles of the sample stage in order to bring the correct zone axis into view, namely the zone axis at which the pores of the zeolite structures are parallel to the electron beam. This zone axis can either be [100] or [001] as they are symmetrically identical. Experiments were carried out with a low beam current and a highly spread out beam so as to minimise damage to the specimen. Once suitable areas were located, experiments transitioned to STEM.
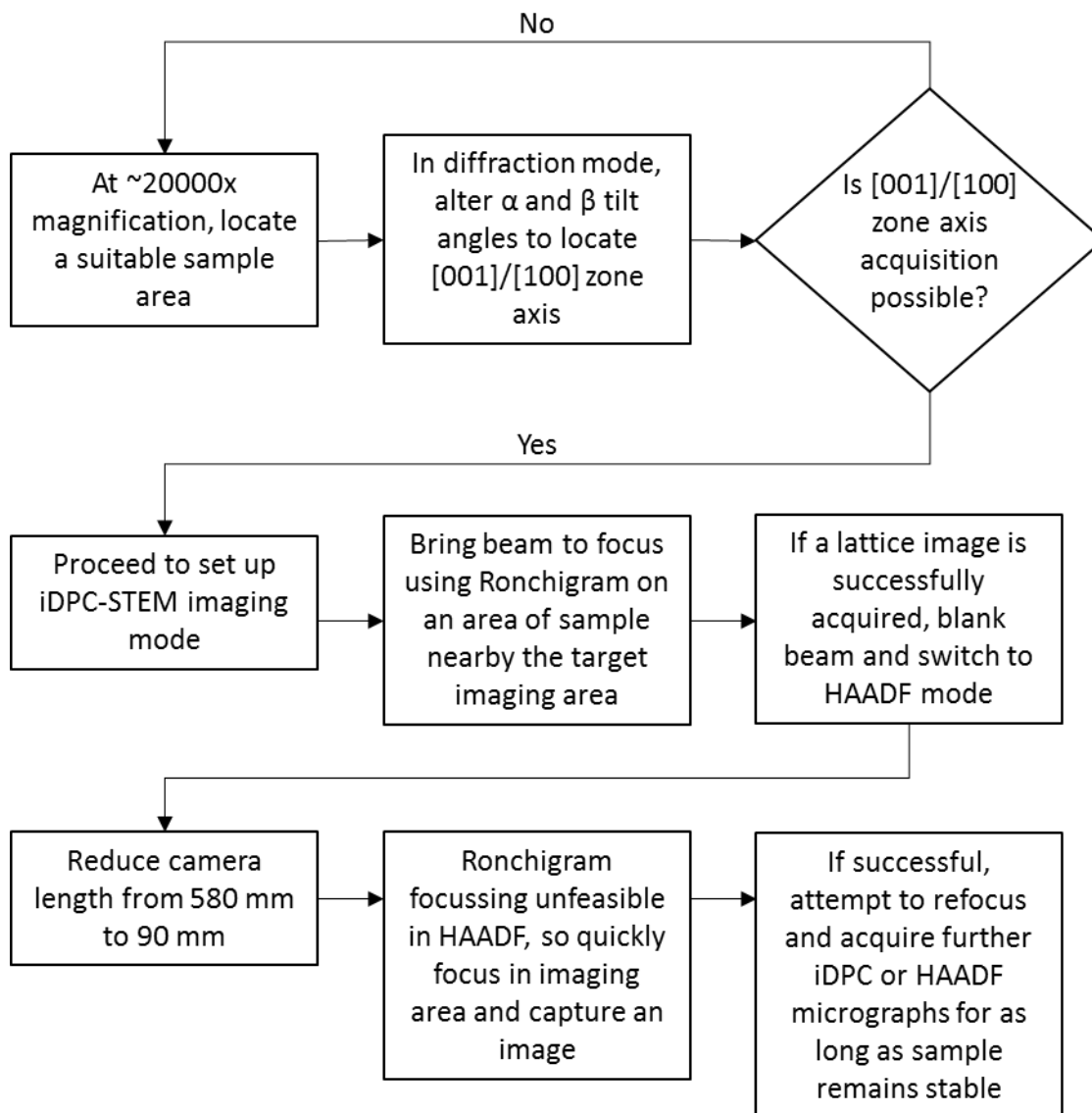
Fig.3.4: Flow chart detailing the acquisition of iDPC and HAADF STEM micrographs, starting from sample area identification in BF-TEM.

For STEM analysis, the electron beam current was reduced to 10 pA. At this current,

observations of up to 1.3M times magnification was possible before electron beam damage of the samples became obstructive. The regions identified in CTEM were observed using BF-STEM with the aim of acquiring lattice and atomic scale resolution images in spite of the sensitivity of the zeolites. Other techniques were used for more in depth analysis, including HAADF and iDPC imaging. With iDPC imaging, the aim was to acquire higher resolution images of the atomic lattices than would be possible with BF imaging. Using HAADF would allow for the identification of Sn sites in the Sn-beta atomic lattice, owing to the atomic mass contrast that HAADF provides. Figure 3.4 shows the experimental progression of joint iDPC and HAADF micrograph acquisition, starting with sample area identification in BF-TEM.

3.5.2 – Simulated HAADF

Simulated HAADF images were produced for comparison to the experimentally acquired images. Simulations were carried out by David Hernandez-Maldonado of the University of Madrid and were produced by multislice simulation using the VESTA software program (http://jp-minerals.org/vesta/en/). Conditions for the simulation were based on the experimental conditions used for STEM imaging of the zeolites, *i.e.* 300 kV accelerating voltage, 1.4 mm probe size, 10 mrad convergence angle, 40 mrad inner detector angle, and 200 mrad outer detector angle. Simulations were produced for Si-beta and Sn-beta zeolites. For the Sn-beta zeolite simulation a single Sn atom replaced a Si atom in a T-3 position close to the centre of a unit cell when observed down the [010] axis. Additional Sn-beta zeolite simulations were produced to investigate the effect of changing sample area thickness (2, 5, and 10 unit cells thick) and changing the position of the Sn atom (T-3 sites at the top and bottom surfaces of the simulation areas, and T-1 sites roughly ¼ and ¾ of the way down an atomic

column). These simulations were performed with the intent of identifying any significant changes in the intensity of the atomic columns containing Sn compared to those not containing Sn.

Figure 3.5 gives an overview of the parameter-space of each technique used to characterise the zeolite samples. SEM and EDX cover the lower resolution ranges to give information regarding surface structure and bulk elemental composition, while the STEM techniques cover atomic resolution content. The simulation provides a consideration of interactions between the electron beam and the sample for comparison to the experimentally obtained results.

Characterisation Technique	Parameter-Space
SEM	Surface Properties (~10 nm - ~1 mm)
EDX	Elemental Composition (~1 nm - ~1000 nm)
iDPC-STEM	Atomic Structure (~0.1 nm - ~50 nm)
HAADF-STEM	Atomic Level Density (~0.1 nm - ~50 nm)
Multi-slice Simulation	Electron Interactions (~0.000001 nm - 10 nm)

Fig.3.5: Table demonstrating the parameter-space of each of the techniques used for characterisation of zeolite samples.

Chapter 4 – Investigation of a Model Organic Material – Determination of the Critical Fluence of Theophylline Form II as a Function of Sample and Microscope Conditions

4.1 – Introduction

The primary purpose of this study is to investigate the effects of varying microscope and sample conditions on the irradiation stability of a model electron beam sensitive organic crystalline material, theophylline's anhydrous form II. This is done with the wider goal of assessing the usefulness of electron microscopy (EM) techniques for the characterisation of similarly beam sensitive organic materials, which are commonly used in major industries such as the pharmaceutical, food, cosmetic, and electronic industries (Vippagunta *et al.*, 2001; Schenk & Peschar, 2004; Kumar, 2000; Forrest & Thompson, 2007). EM techniques have been used previously to characterise crystalline organics such as phthalocyanines (Murata *et al.*, 1976; Menter, 1956), paraffin (Evans *et al.*, 2008; Zemlin *et al.*, 1985), and the pharmaceutical griseofulvin (Ricarte *et al.*, 2015) to name only a few. Despite the usefulness and potential of EM in this field, there is little in the way of a standardised methodology regarding the characterisation of beam sensitive crystalline organic materials. If these methodologies can be developed with the technologies that are readily available today, EM techniques may become an invaluable assessment tool for the analysis of crystalline organics on an academic and industrial scale. The first step towards that goal is understanding the effects of the electron beam on such materials, and how to mitigate damage.

4.2 – X-ray Diffraction and Scanning Electron Microscopy

Ensuring that the theophylline used in these experiments is the intended polymorphic form is of great importance, as the intended form II is needed for consistency during the EM experiments. This can be determined in several ways, such as by observation of crystal morphology by scanning electron microscopy (SEM) or by diffraction pattern (DP) analysis. X-ray diffraction (XRD) is a reliable method of determining and comparing crystal structures of multiple samples, as well as providing information regarding several other sample characteristics (purity, crystallite size, strain *etc.*)
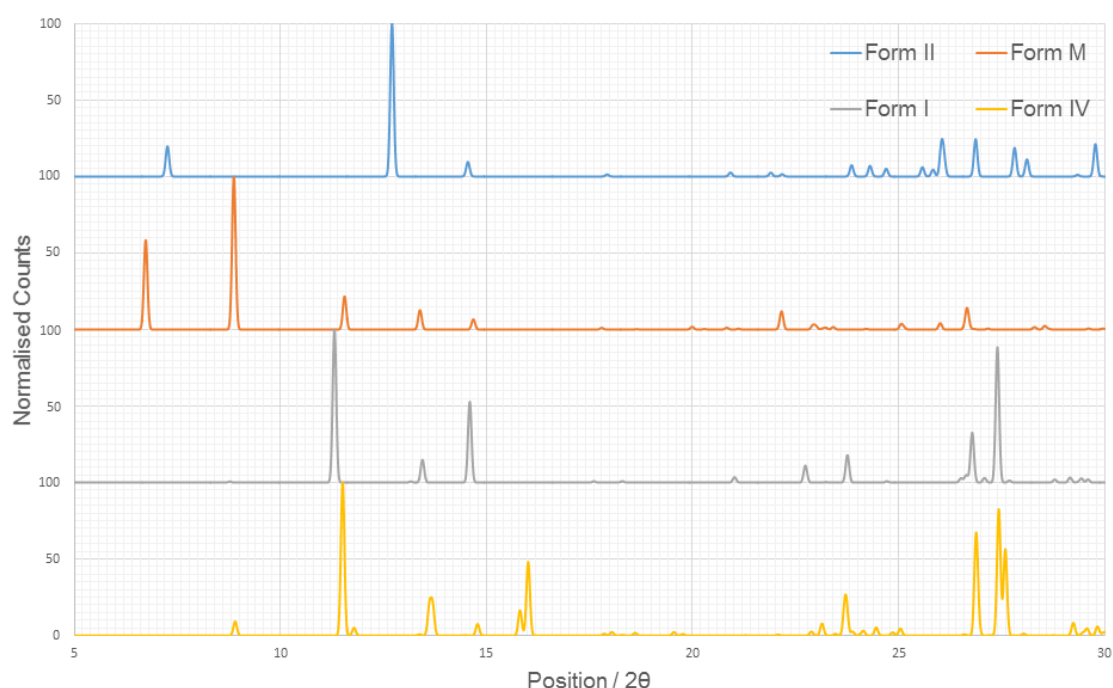
Fig.4.1: Simulated powder XRD data of the four stable anhydrous forms of theophylline. Data simulated using CrystalMaker software and .cif files. The CCDC references for the .cif files used and the structures they describe are listed in section 3.2.1.

Experimental XRD patterns were acquired using a PANalytical XPERT diffractometer using copper K-α radiation (λ = 1.541 Å). Powder samples were flattened into a plastic sample plate and scanned at a step size of 0.0025° 2θ, in the 5 to 30° 2θ angle range over 10 minutes.

77

SEM was carried out on as-bought and nitromethane recrystallised theophylline crystals in order to confirm their morphologies, determine average crystal/particle sizes, observe surface features, and verify the morphological changes suggested by the XRD results. As-bought theophylline crystals were directly deposited on to adhesive carbon substrates mounted on aluminium sample stubs. Recrystallised theophylline was grown directly on to the aluminium sample stubs from a saturated nitromethane solution (as per Eddleston, 2011), heated at ~70 °C to expedite the evaporation of the nitromethane.
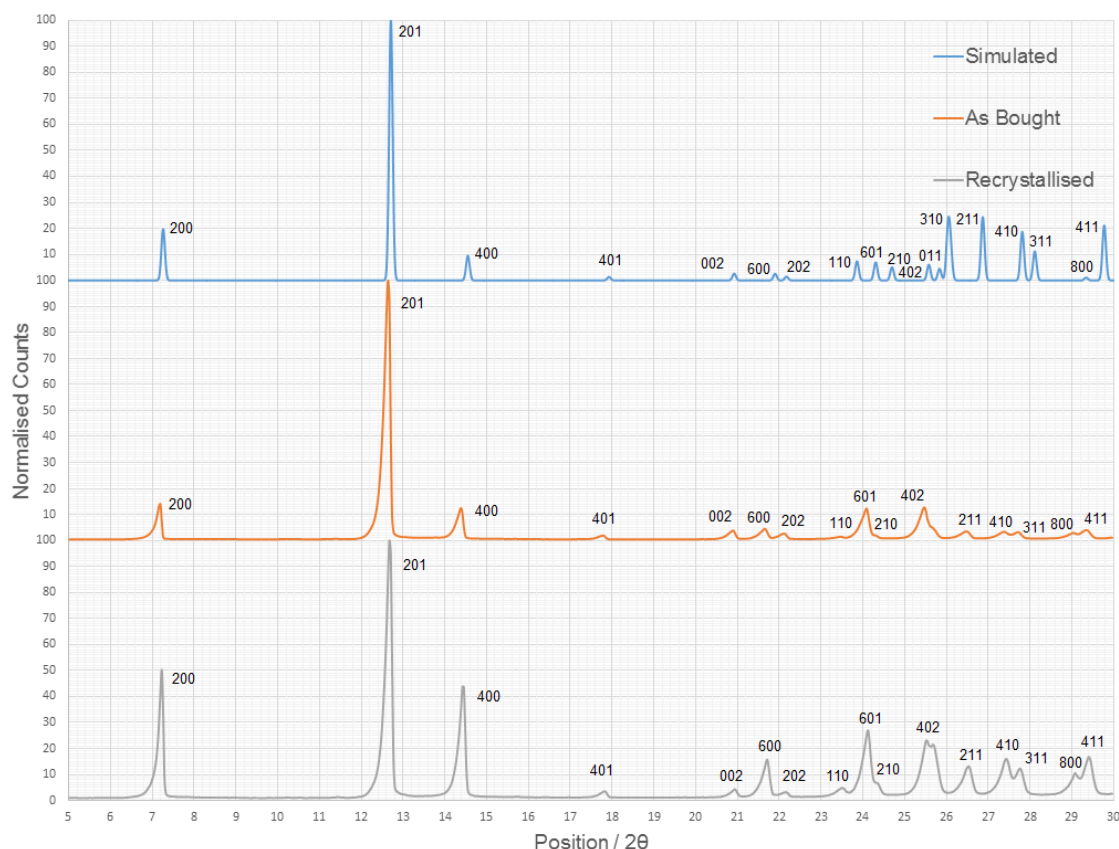
Fig.4.2: XRD patterns of simulated theophylline form II and experimentally acquired patterns for as-bought and recrystallised theophylline.

Firstly, it must be shown that the theophylline recrystallised from the nitromethane solution is the expected form II, as opposed to one of the three other stable anhydrous forms. Figure 4.1 shows the simulated XRD patterns of each of these forms, produced

using the CrystalMaker software, with the uppermost pattern being the desired anhydrous form II. Figure 4.2 shows the simulated form II pattern in comparison with the experimentally acquired XRD patterns of theophylline, both as-bought and recrystallised from nitromethane solution.
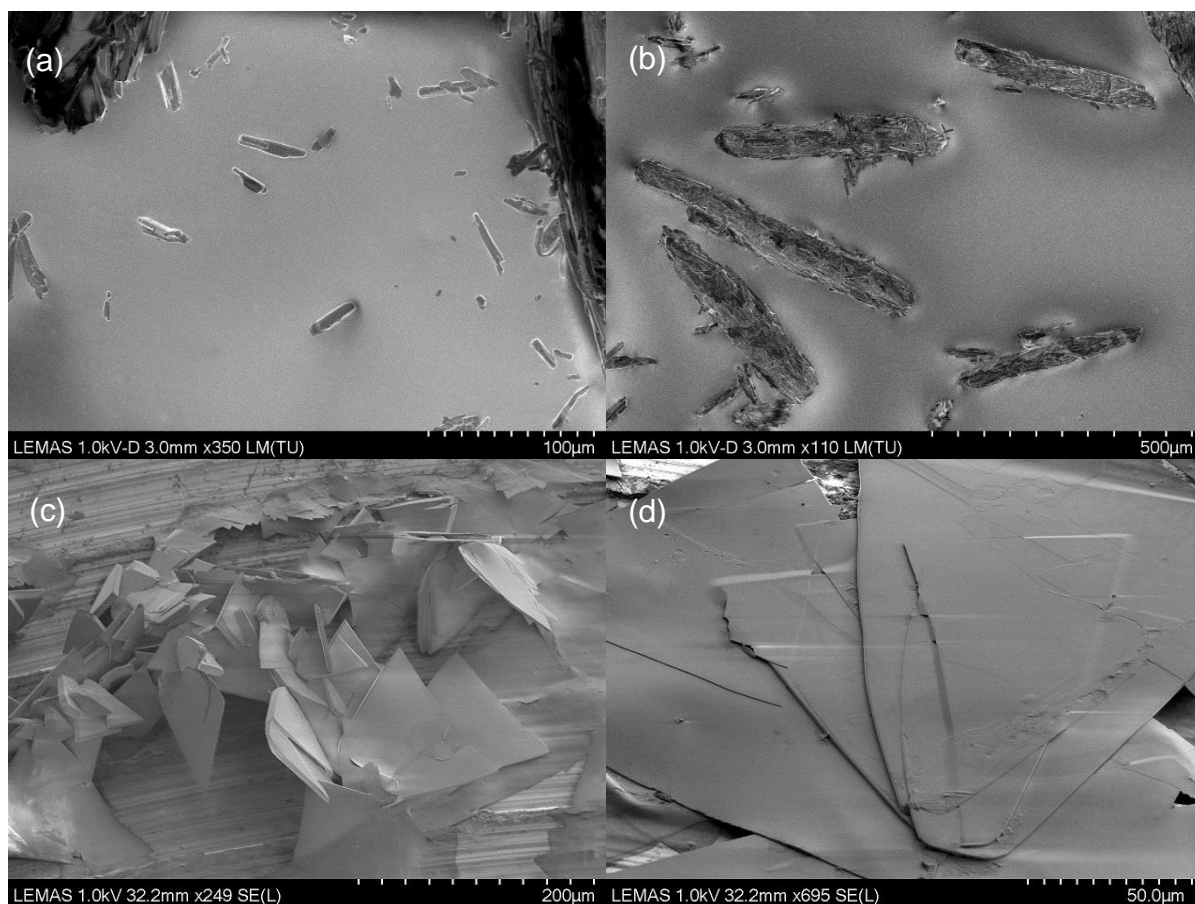
Fig.4.3: Secondary electron SEM micrographs of (a-b) crystals of as-bought theophylline form II, and (c-d) crystals of recrystallised theophylline form II. Micrographs are from samples mounted on aluminium sample stubs. Images acquired with a 1 kV beam acceleration in deceleration mode.

From the patterns shown in figure 4.2, we can confirm that the theophylline, both in its as-bought state and after recrystallisation from nitromethane, is the desired form II, based on the close match between experimental and simulated XRD patterns. Other characteristics are notable based on the XRD data. Firstly, the theophylline is very pure both before and after recrystallisation, with no notable additional or unexplained

diffraction peaks, which would indicate the presence of other crystalline phases. Secondly, there is a significant change in crystal morphology after recrystallisation, as noted by the change in relative peak intensities in the recrystallised materials. In the as-bought theophylline, the relative intensities of peaks more closely resemble that of the simulated pattern which assumes a random orientation of crystallites. The intensity of the {200} family of peaks increases relative to the intensity of the {201} family of peaks after recrystallisation, although the (201) peak still remains the most intense peak. The intensity of the (002) peak remains low in both cases, suggesting limited morphological alteration in this direction.

The changes between the as-bought and recrystallised XRD patterns suggest a transition from a random crystallite orientation to a more preferred or textured crystallite orientation. The increase in {200} family of peaks intensity suggests a preferred orientation of crystals in the [100] direction. Figures 4.3 (a-b) and (c-d) show SEM micrographs of the as-bought and recrystallised theophylline respectively. The morphological changes observed agree well with the XRD results, showing a transition from needle-like crystals to large, plate-like crystals.

Figure 4.4 shows a schematic diagram of a theophylline crystal formed by recrystallisation from nitromethane solution. The isosceles triangle shape of the crystals is shown experimentally in figure 4.5, with the (011) and (0-11) facets being longer than the (001) facet and making up the edges of the triangular crystals.
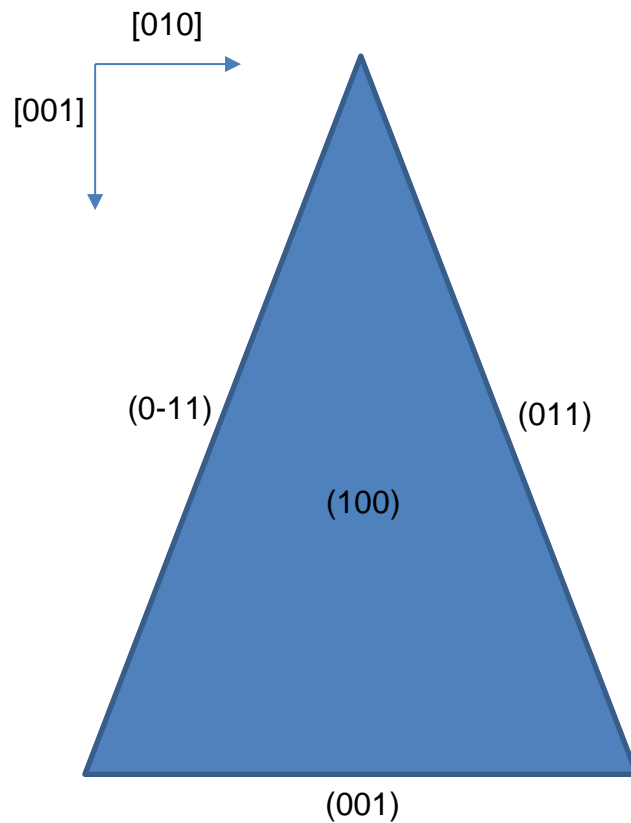
Fig.4.4: Schematic of a recrystallised theophylline form II crystal observed down the [100] axis. Based on experimental observations, crystals are typically many tens to hundreds of micrometres long in the [001] and [010] directions, but only up to several hundred nanometres thickness in the [100] direction.

In figure 4.3 (c), several theophylline crystals appear to have grown out from other crystals at odd angles. When deposited on a substrate, the plate-like morphologies of the crystals mean they would grow and lay flat consistently, as with the crystals in figure 4.3 (d). This would be ideal for TEM analysis, since crystals lying flat have a suitable projected thickness for the electron beam to pass through the entire sample easily, though individual crystals would be preferable compared to the multiple crystals shown in 4.3 (d) laying atop one another. Additionally, crystals in both figures 4.3 (c) and (d) are of inconsistent thickness, either due to fracturing or growth of multiple crystals on top of one other.
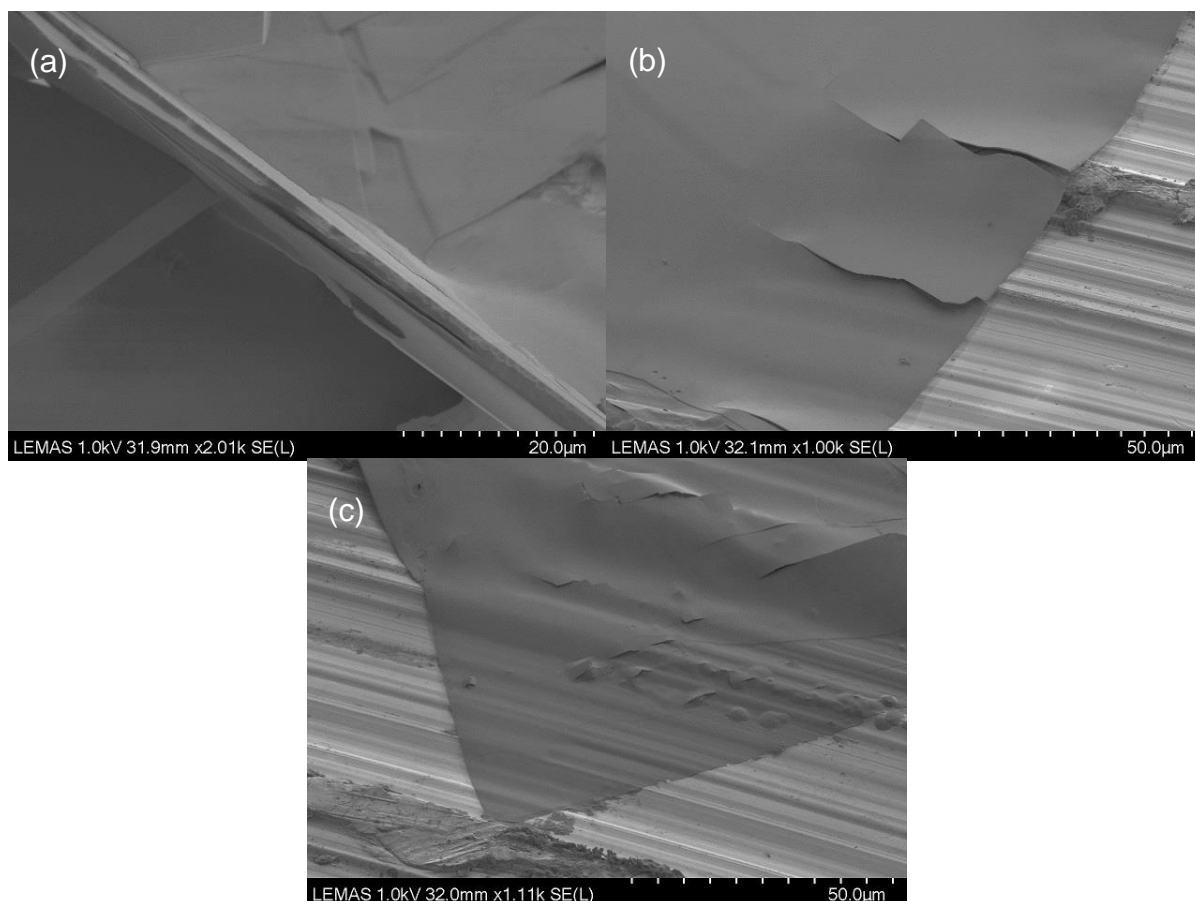
Fig.4.5: Secondary electron SEM micrographs of recrystallised theophylline form II crystals, showing (a) a crystal observed side-on, (b) a crystal region with multiple fractures, and (c) a thin crystal which has conformed to the shape of the aluminium substrate and fractured in multiple areas. Images acquired using a 1 kV beam acceleration in deceleration mode.

Observing a theophylline crystal side-on, as in figure 4.5 (a), the inconsistency in crystal thickness is highlighted, and a fracture running parallel to the major surfaces is evident. Since sample thickness plays a key role in damage progression in organic samples like theophylline, inconsistencies in thickness can affect C_F, and will be a likely cause of variation (Egerton *et al.*, 2004). Figure 4.5 (b) shows a theophylline crystal with two large fractures through it. Due to the long and wide but thin nature of the crystals, such fractures could be easily formed during crystal growth, but could also be indicative of defects in the crystalline lattice itself. Similar fractures are seen in the crystal in figure 4.5 (c). The fractures observed are oriented in similar directions,

suggesting a weakness in the crystalline structure of theophylline in this direction and a likely (100) shear or cleavage plane. Defects such as this were often noted by Eddleston (2011), particularly in the [010] direction which correspond to the likely direction of the fractures observed in figure 4.5 (b).

Also shown in figure 4.5 (c) is a crystal for which the aluminium stub substrate morphology has impacted on the crystal's morphology. The ridges and pits present on the aluminium stub cause similar structures to present themselves in the crystal itself. The morphology of the theophylline crystals seems affected by the substrate on which the crystals are grown. Such structural deformations could have an effect on the DPs acquired in TEM experiments. This is also apparent in the increased strain in the [100] direction observed by XRD for the recrystallised theophylline plates (figure 4.5 (a)).

4.3 – Transmission Electron Microscopy

4.3.1 – Bright-Field Imaging

By use of BF imaging in TEM, it was possible to image numerous theophylline form II crystals. Initial results (such as in figures 4.6 (a–c) and 4.7 (a–c)) further confirmed the morphology of the crystals as the large, triangular plates and, together with selected area electron diffraction, indicated that many of these crystals were transparent to the electron beam while oriented with the beam perpendicular to the largest crystal faces, *i.e.* the beam oriented down the [100] direction.
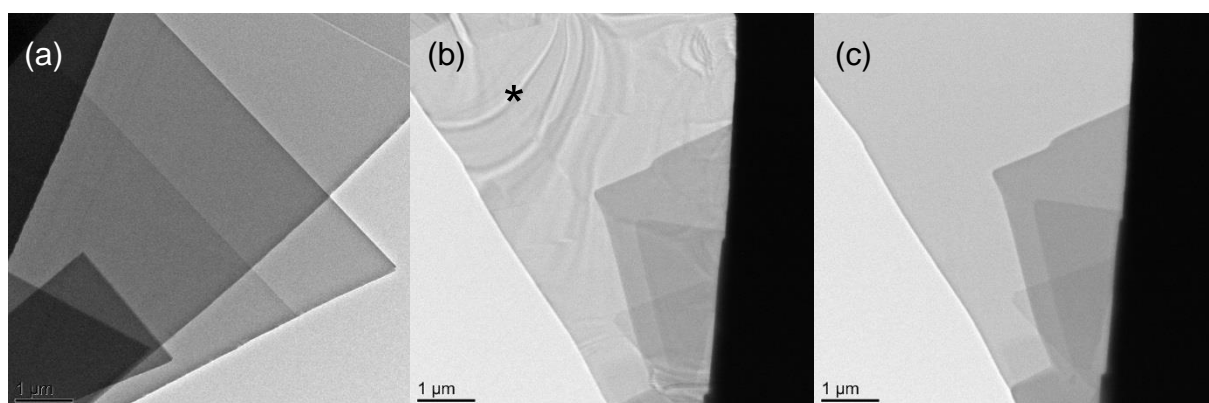
Fig.4.6: (a) BF-TEM micrograph of several theophylline crystals, oriented with the (100) plane perpendicular to the beam direction. (b) BF-TEM micrograph of several theophylline crystals, showing bend contours. Micrograph acquired before several minutes of beam exposure, or roughly 60 e⁻Å⁻² total fluence. (c) BF-TEM of the same crystals as shown in (b). The bend contours have disappeared after several minutes of beam exposure. Images acquired at 200 kV beam acceleration and at ambient temperatures.

Overlap of two or more crystals results in an obvious change in BF image contrast. For consistency when acquiring DPs for the purpose of C_F measurement, patterns were acquired from regions with only a single crystal present, since thickness changes in a sample could affect damage accumulation. The C_F can be roughly estimated at this stage, as the bend contours are indicators of crystallinity in the sample, and

changes can be made to imaging conditions accordingly to account for the sample's sensitivity. The bend contours shift during irradiation, suggesting further straining of the crystals during electron beam exposure as a result of bond breakage and potential hydrogen loss by radiolysis (Egerton *et al.*, 2004). The contours are eventually extinguished after prolonged beam exposure, as shown by the difference between figures 4.6 (b) and 4.5 (c). At a flux of 0.1 e$^-$Å^{-2}s^{-1}, bend contours lasted between 3 and 5 minutes, suggesting a critical fluence of between 18 and 30 e$^-$Å^{-2}.
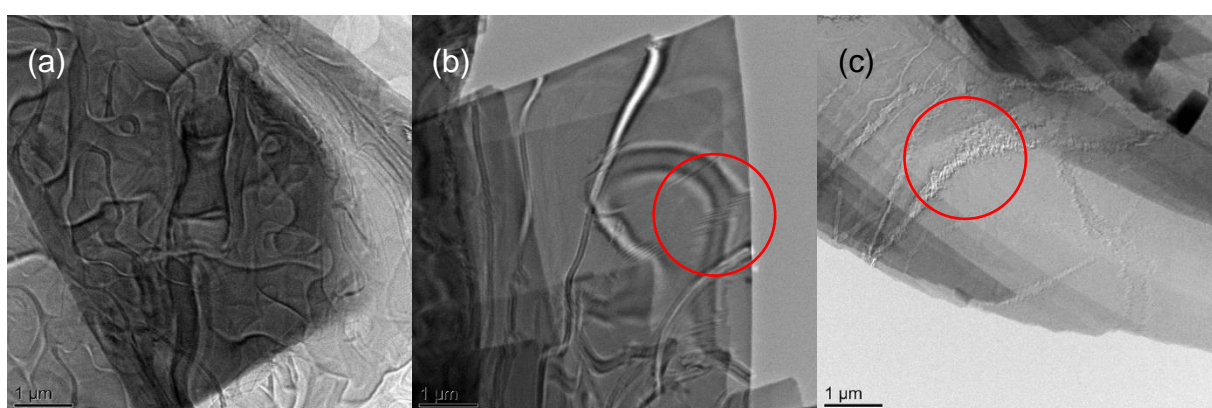
Fig.4.7: BF-TEM micrographs of theophylline form II crystals, showing (a) high densities of bend contours, (b) several large bend contours, and (c) several large, fractured bend contours. The circled areas in (b) and (c) highlight regions of high defect density. Images acquired at 200 kV beam acceleration and at ambient temperatures.

The presence of bend contours, as the name suggests, indicates a curvature in a crystal. This curvature causes compression and extension of the crystal lattice, which in turn causes alterations to the diffraction intensities, appearing in BF micrographs as contours covering a crystal. They can also highlight the presence and density of defects in a crystal. In crystals with few or no defects, bend contours would be continuous and unbroken curves running across a crystal, as with the contour marked with an asterisk in figure 4.6 (b). Defects which affect the lattice structure of the planes involved with the production of the bend contours cause breaks in the bend contours,

as observed with high density in the circled areas in figures 4.7 (b) and (c). The greater the number of breaks, the higher the density of defects. In this case the crystal in figure 4.7 (c) demonstrates a far greater density of contour breaks, and therefore defects, than the crystals in figures 4.7 (a) and (b).

As noted by Eddleston (2011), determining the exact type of lattice defect purely from observations of BF-TEM micrographs is difficult. Defect density was noted to be related to the speed with which crystals were allowed to form and grow, with crystals grown quicker (either from a more concentrated solution or by rapid cooling) more prone to defect formation. Defects observed by Eddleston included edge and screw dislocations, as well as stacking faults, though these had to be confirmed through the use of AFM. This effect may be a good explanation for the high density of defects observed in the samples shown in figure 4.7 (b) and (c), as the synthesis of these crystals was by means of a heated, saturated nitromethane solution being allowed to cool to room temperature by simply removing the heat source, rather than by a controlled cooling method. The high concentration of theophylline in this solution, combined with a relatively quick cooling rate, would cause rapid crystallisation, and therefore a high density of defects.

While generally interesting, defect observation and identification is not the primary focus of this work. Such defects could be useful in subsequent research if TEM can be shown to be a useful and viable experimental method for beam-sensitive materials, particularly for characterisations of pharmaceuticals and other materials for which dissolution properties are important.

4.3.2 – Diffraction Patterns and Critical Fluence Determination

Initially, single DPs were acquired to assess the reliability with which [100] patterns could be obtained. After acquisition of ~75 patterns, more than 50% were indexed as [100] without any prior reorientation of the sample. This is put down to the flat shape of the theophylline form II crystals, which grow and naturally lay flat on the TEM support films. As such, most of the time, the (100) plane will be perpendicular to the beam direction and is ideal for C_F measurement by DP analysis, since no time need be wasted before pattern acquisition on reorienting the sample.
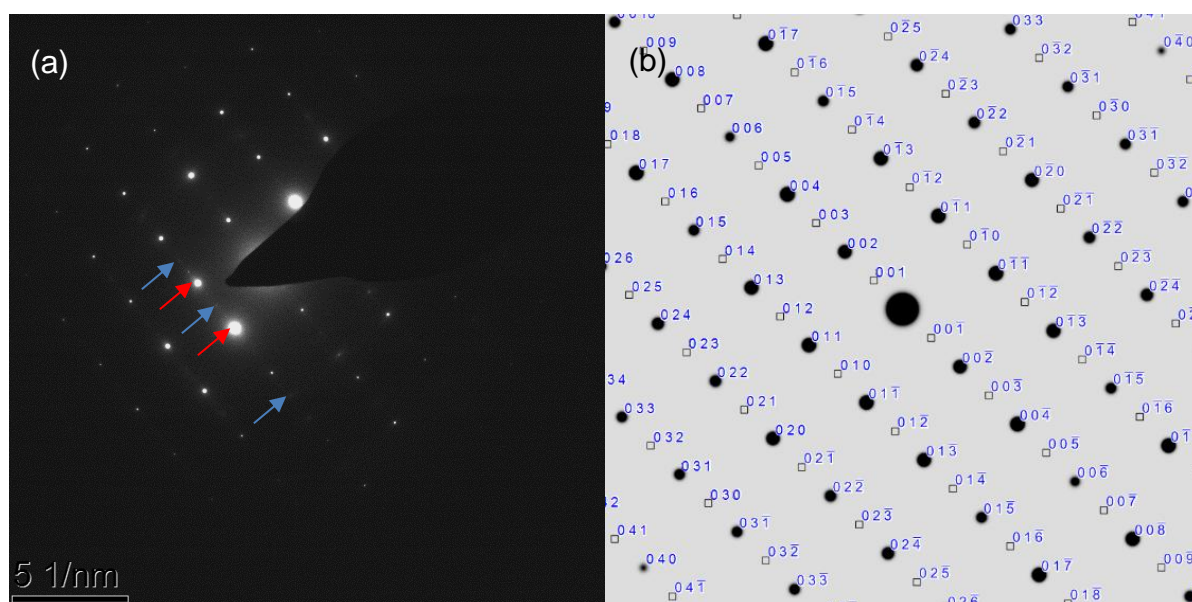
Fig.4.8: (a) An experimentally acquired [100] DP of theophylline form II, in comparison to (b) a simulated theophylline form II [100] DP showing both diffraction spots and systematic absences. The CrystalMaker software was used to produce the simulated pattern, along with the .cif file for theophylline form II, (CCDC reference 878133). The blue arrows in (a) highlight systematic absences with spots barely visible in positions (012), (010), and (01$\overline{4}$) respectively, while the red arrows highlight two {011} spots with different intensities. Acquired using 200 kV beam acceleration and a 40 μm diameter selected area aperture.

This is of particular importance for highly beam sensitive materials like theophylline. Every step of experiments like these which requires exposing the specimen to the

electron beam reduces the available lifetime of the specimen *i.e.* the dose budget, a concept which will be discussed in greater detail in chapter 5.

Figure 4.8 shows one of the experimentally acquired [100] DPs side-by-side with a CrystalMaker simulated [100] DP for theophylline form II. In terms of spot positions, the patterns match well, although there are significant differences between the relative intensities of the spots. This discrepancy can be explained by the inability of the simulated diffraction to account for the effects of crystal morphology and bend contours leading to the crystal being oriented slightly off-axis (*i.e.* dynamic diffraction effects). Also of note is the presence of dim spots where systematic absences should be in figure 4.8 (a). This is likely due to a combination of the sample thickness and presence of defects in the crystal, causing multiple diffractions of the electron beam, or a rotational misalignment of crystals along [100].

Figure 4.9 shows a series of [100] DPs, acquired over ten minutes of total electron beam exposure at 0.1 e$^-$Å^{-2}s. The observed changes indicate a loss of short range structural order over the first 3 minutes, followed by complete loss of long range order over the next 2 minutes. This is visualised by the degradation of the outer diffraction spots, followed by the inner spots. This damage progression is typical for many organic materials observed in the TEM (Glaeser & Taylor, 1978). The initial reduction in the intensity of outer diffraction spots is an indication of the loss of short-range order, *i.e.* weak intermolecular bonds are broken, causing localised rearrangement of atoms and disruption of the crystalline structure. Long range order, represented by the innermost diffraction spots, persist to higher total fluences as a result of certain atomic and molecular species retaining their positions relative to one another, immobilised by the surrounding amorphous material. In other words, the general molecular packing is maintained. These innermost spots eventually decay as the molecular species are

broken apart and mass loss occurs (Chapman *et al.*, 1980).
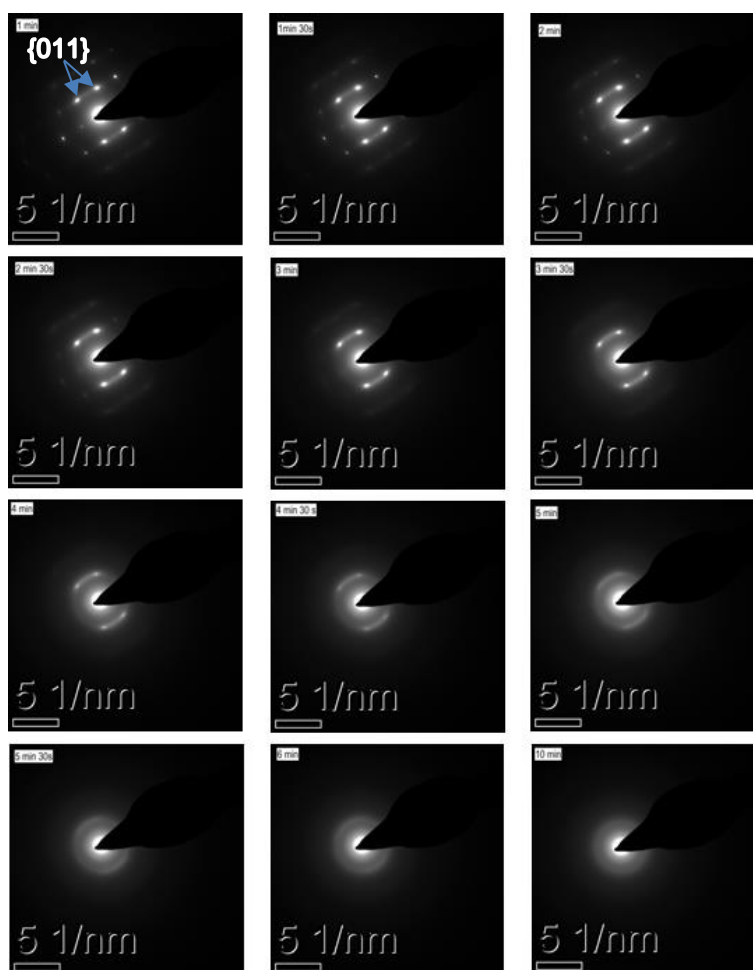
Fig.4.9: A series of [100] DPs taken from the same area of a theophylline form II crystal at different times after the start of beam exposure. Series taken at 300 kV with a 40 µm diameter selected area aperture. The arrows in the first pattern denote two of the {011} spots whose intensities were measured to determine C_F.

By measuring the intensities of selected spots (the {011} spots in this case, highlighted by arrows in the first DP of figure 4.9) as a function of total electron fluence, a C_F at which the normalised spot intensity has decayed to $\frac{1}{e}$ (~37 %) of the highest intensity can be determined. The intensities of each {011} spot in a DP series were measured at each time step and averaged, then averaged across multiple DP series using the same time steps and conditions. The number of measurements used ranged from ~5

for more time consuming experiments, such as with the sample cooled to liquid nitrogen temperatures, to ~20 for simpler experiments, such as when using the standard conditions.

Figures 4.10 (a-b) show examples of these measurements from particular {011} diffraction spots of a [100] DP of theophylline. In (a), the overall profile is a classic steepening decline in spot intensity followed by a tail off to zero and is one of many common profiles observed. In other data sets, such as figure 4.10 (b), spot intensities show a rather strange initial increase up to a maximum before decay sets in. Additional observed profile features include plateaus part way through exposure, and initial drops in intensity followed by a rise and eventual decay to zero. This wide range of potential profiles highlights the importance of repeated data collection and averaging of results from equivalent diffraction spots and data sets.
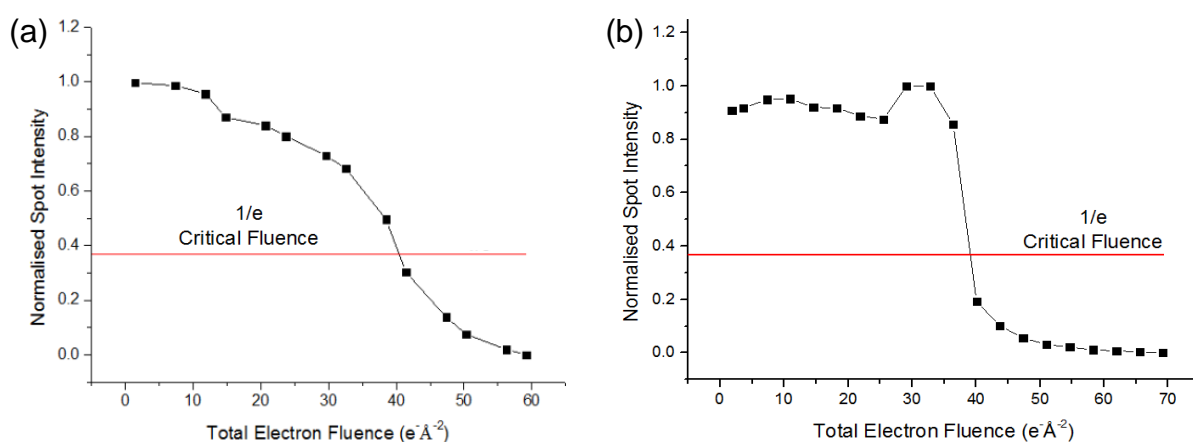
Fig.4.10: Graphs of normalised spot intensity versus total electron fluence for a (011) diffraction spot from a [100] DP series of theophylline form II at 300 kV. The C_F is measured off at 1/e of the initial spot intensity, which in these cases is about 40 e⁻Å².

These varied profiles have been observed before in pthalocyanines and a variety of pharmaceutical materials (Clark *et al.*, 1980; S'ari *et al.*, 2018) and have a number of potential origins. Effects such as the reorientation of crystals, mass loss, or rotation of

bonds have been suggested as reasons for the observation of plateaus in intensity profiles (Stenn and Barr, 2004; Egerton *et al.*, 2004). The cause of rising intensities can potentially be explained by the effects of high densities of lattice defects forming during irradiation, causing the electron beam to encounter strain fields as it passes through the sample. This could increase intensities in spots representing planes affected by these strain fields (Koehler, 1969). Similarly, the movement of bend contours through the exposed area would cause shifting intensities in the spots of planes affected by said contours, *i.e.* lattice reorientation. Considering that both large numbers of defects (figure 4.7 (c)) and bend contours (figure 4.7 (b)) are observed in the theophylline form II samples, either or both of these explanations would be appropriate for explaining the varying intensities of diffraction spots, as in figure 4.10.

Figure 4.11 shows the mean C_F values determined for the standard conditions (SC) and for varying microscope and sample parameters. Standard conditions were 200 kV accelerating voltage, ambient temperature, and with the sample deposited on a continuous carbon support film. Error bars are based on the standard deviation of CFs obtained over a number of repeat measurements for each set of conditions. For the standard conditions, the mean average C_F was determined to be 27 ± 5.1 e$^-$Å^{-2}. For comparison, the C_Fs of a number of organic materials determined previously by other authors are presented in figure 2.16. These values were all acquired at 100 kV, so would be relatively comparable to the theophylline C_F acquired at 80 kV (10.8 ± 2.8 e$^-$Å^{-2}). This would make theophylline more stable than paraffin or anthracene, but less stable than any of the phthalocyanine variants.

From the results in figure 4.11, improved stability in theophylline form II was achieved when using a 300 kV accelerating voltage (36.3 ± 8 e$^-$Å^{-2}) or a graphene film substrate in place of continuous carbon (34.5 ± 0.4 e$^-$Å^{-2}). Increased sample temperature (423

K) and a lower beam accelerating voltage (80 kV) reduced the stability of theophylline, giving CFs of 22.5 ± 7.5 and 10.7 ± 2.8 e⁻Å⁻² respectively. Lower sample temperatures (173 K and 93 K) had negligible impact on sample stability, giving CFs of 25 ± 4 and 27 ± 1.5 e⁻Å⁻² respectively, but using a combination of a graphene film substrate and 93 K sample temperature resulted in the highest obtained C_F of 42 ± 4 e⁻Å⁻².
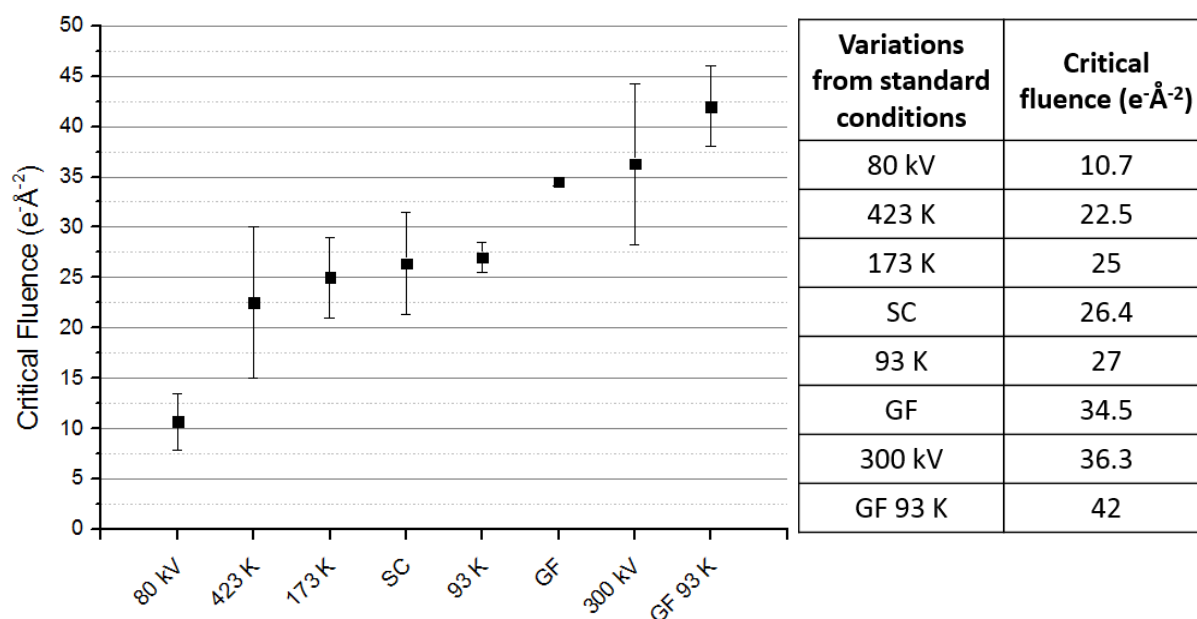
Variations from standard conditions	Critical fluence (e⁻Å⁻²)
80 kV	10.7
423 K	22.5
173 K	25
SC	26.4
93 K	27
GF	34.5
300 kV	36.3
GF 93 K	42

Fig.4.11: Graph of CFs for theophylline form II arranged in order from lowest to highest (least stable to most stable). CFs also shown in the table to the right. Values with units kV refer to electron beam accelerating voltages, while values with units K refer to sample temperatures. Acronyms SC and GF stand for 'standard conditions' and 'graphene film' respectively. Error bars were determined by standard deviation of CFs measured from multiple DP intensity series.

The large standard deviation seen in some of these results is a likely side effect of the uncontrollable thickness of the crystals observed. For each DP series acquired, the area illuminated was only ever a single crystal thick. However, as the SEM results highlight, even single crystals can have highly variable thicknesses. Techniques such as AFM, EELS, or contrast measurement in TEM micrographs could be utilised to measure thickness, but each would be quite time consuming, with EELS and TEM

contrast measurement taking up valuable dose budget.

The improved stability achieved by using 300 kV accelerating voltage rather than 200 kV is a well documented effect arising from the decreased interaction volume of the electron beam at higher accelerating voltages. The lower interaction volume decreases the chance of an interaction between the incident electrons and the sample. Therefore, fewer instances of damage result from these interactions. Although the electrons have more energy at higher accelerating voltages, there is sufficient energy to cause radiolysis regardless of whether 80, 200, or 300 kV is used. Hence, the limiting factor for radiolysis, in this accelerating voltage range, is simply the raw number of interactions that occur (Egerton *et al.*, 2004). However, while increasing accelerating voltage reduces the rate of radiolytic damage in the sample, it also decreases the elastic cross-section by the same ratio $\left(\frac{1}{E^0}\right)$. Therefore, though the sample will survive beam exposure for longer, this comes at the cost of lower image contrast and collection efficiency. Overall, this results in potentially no net improvement to the DLR (Egerton, 2013). See the discussion of DLR in section 5.1 for more details.

The stabilisation effect of graphene film is also one that has been recorded previously (Zan *et al.*, 2013). Graphene's high electrical and thermal conductivity aids sample stabilisation by reducing the effects of sample charging and heating. This explains the increased C_F observed in samples which included graphene film as a substrate. Further improvements may be expected if a second layer of graphene were added over the top of the sample (Wang *et al.*, 2014; Wilson *et al.*, 2009).

Increasing sample temperature caused a slight, but expected, decrease in stability. Organic materials such as theophylline are too complex to benefit from an increase in

temperature to drive bond repair, such as in materials like graphene/graphite (Freeman *et al.*, 2017). Instead, the increase in thermal energy increases the rate at which damage occurs.

The effect of decreasing sample temperature can have a stabilising effect, though this is highly dependent on the nature of the sample. Investigated by Glaeser and Taylor (1978), it was found that small molecule, anhydrous compounds benefitted only marginally from a low sample temperature, if at all. Larger, hydrated molecules benefitted from increased stability at lower temperatures, in some cases reducing damage rate by an order of magnitude. Since the theophylline experimented upon here is in its anhydrous form and is a relatively small molecule, the negligible effect of lower sample temperature would seem to correlate with these findings.

4.4 – Summary

The results of the XRD and SEM confirmed the crystallisation of form II of theophylline from the saturated nitromethane solution and show the transition from needle-like crystals in the as-bought theophylline to the desired large, flat, triangular plate crystals when recrystallised. SEM and TEM results highlight areas within a high density of crystal defects and potential for shearing in the recrystallised crystals.

The measurement of CFs of theophylline form II under different microscope and sample conditions provided mostly expected results, with the exception being the lack of significant improvement in stability when the sample was cooled. The greatest improvement in stability was observed when a graphene support film was used in conjunction with sample cooling. Despite the improvement, the C_F was only improved by ~ 60%, which, under the low-fluence conditions used, is relatively minor. Going forward, similar experiments would benefit from imaging at 300 kV where available, and only making changes to support film or sample temperature where absolutely necessary to maximise stability.

Follow up work on measuring the C_F of a number of different beam sensitive organic materials has been performed which did not rely on alterations to temperature or sample support film (S'ari *et al.*, 2015). Compared to the materials characterised in that work, theophylline is more stable with a C_F of 26.4 $e^-Å^{-2}$ for at standard conditions compared to 0.33 – 20.79 $e^-Å^{-2}$ for the ten materials analysed. Why exactly this is the case remains debatable, though further work by S'ari *et al.*, 2018, attempted to develop a predictive method of determining C_F of pharmaceutical materials based on their molecular structures. A group of three descriptors were found to most accurately predict the C_F of each molecule, these being the ratio of conjugated carbons to non-conjugated carbons, the ratio of hydrogen bond donors to acceptors, and the ratio of

hydrogen bond acceptors to donors, with the first of these showing a positive correlation to C_F and the other two showing a negative correlation. This may explain the relative stability of theophylline, as it has few hydrogen donors/acceptors and several conjugated carbons, though this method does not take into account intermolecular effects such as crystal enthalpy (stability). Additionally, theophylline is not classed as poorly soluble, which each of the materials in the study by S'ari *et al.*, 2018, was, so direct comparison may not be appropriate.

Chapter 5 – Acquisition of High-Resolution Lattice Information of Theophylline Form II

5.1 – Background

For any industry in which crystallised organic materials are utilised, information regarding the structure of such materials down to the atomic level is exceptionally useful, as it can be used for understanding the effects of materials processing. Conventional electron microscopy (EM) experimental techniques lack the sensitivity to reliably characterise organic materials to this level without destroying the sample. Scanning transmission electron microscopy (STEM) techniques have the potential to be used for the acquisition of this information. Such techniques have been previously shown to achieve spatial resolutions of <0.5 Å (Batson, 2002), although this was done using inorganic material samples relatively insensitive to electron beam induced damage.

The current density in the probe required for high-resolution STEM (typically $>10^5$ – 10^6 e⁻Å^{-2}) makes the use of STEM for observation of beam-sensitive organics a risky prospect, as such samples rapidly decay under conditions which would typically be used for analysis of stable inorganics. As a result, direct resolution of the lattice structures of sensitive organics has remained an elusive feat and is inherently limited by the electron beam sensitivity of the samples. Despite the difficulty, previous studies have utilised low-fluence CTEM methods to acquire lattice and molecular information of various materials, including polyethylene (Revol & St John Manley, 1986), copper and platinum phthalocyanines (Murata *et al.*, 1976; Menter 1956), quaterrylene (Smith & Fryer, 1981), paraffin (Zemlin *et al.*, 1985), and caffeine-glutaric acid co-crystals (Hasa *et al.*, 2016). Many other organics that are less sensitive to the beam are routinely analysed using CTEM methods and resolved at the molecular level

(Kobayashi, 1993).

Improvements in the collection efficiency of EM cameras have the potential to simplify direct observations of lattices in sensitive materials at low electron fluences. The degree to which dose-limited resolution (DLR) is improved through the use of a camera with improved detector quantum efficiency (DQE) is calculable by equation 5.1 (from Egerton, 2010).

$$(5.1) \quad DLR = \frac{SNR\sqrt{2}}{|C|\sqrt{DQE}\sqrt{FC_F/e}}$$

SNR is the signal-to-noise ratio which must equal or exceed a chosen background value, typically at least 3-5 times the standard deviation of the background noise to satisfy the Rose criterion (Rose, 1974). DQE is the detector quantum efficiency, a fundamental variable relating to a detector's ability to convert the signal received into an image. A higher DQE means that less input signal is required to produce an image of the same quality as a camera with lower DQE (alternatively, the camera with the higher DQE will produce a higher quality image with the same input signal). A camera which perfectly converts all input signal to an output image across all spatial frequencies would have a DQE of 1. Most complementary metal-organic semiconductor (CMOS) detectors, such as the Gatan OneView 4K used for most of the CTEM experiments reported here, have a DQE of ~0.5. C is the contrast, F is the collection efficiency of incident to detected electrons, C_F is the critical fluence, and e is the fundamental charge of an electron. C is a function of critical fluence, whilst F varies with kV and detector collection angles.

If all other variables are kept the same, increasing DQE causes a decrease (improvement) in DLR. In the first part of this study (section 5.2), a high-end Gatan K2 direct electron detection camera (with a DQE of roughly 0.8) will be used to attempt

direct lattice imaging of theophylline form II by CTEM.

Increasing the kV of the electron beam reduces the inelastic interaction cross-section and the elastic interaction cross-section by the same amount. This improves specimen stability, but at the cost of lower contrast and collection efficiency. However, if the specimen is relatively thick there may still be an improvement in DLR (Egerton, 2018).

While DQE is an important aspect of attaining a useable DLR, the C_F is the key limiting factor. Additionally, any electron beam exposure that occurs prior to final imaging will reduce the available lifetime of the specimen, *i.e.* the available dose budget, the dose within which all experimental steps which require the specimen to be exposed to the beam must be carried out under. Steps such as locating and focussing on the sample in CTEM take up some of the dose budget for a given sample area. STEM has an inherent advantage in this regard, as the area exposed to the beam for image capture is much smaller compared to in CTEM. Focussing of the beam can be done in an area nearby but separate from the area that is to be imaged. Additionally, the spread of the electron beam outside the imaging area means that a large area of the sample is exposed to the beam and damaged accordingly.

In STEM, F is decreased as electrons scattered to higher angles are not collected by the detector. This results in a decreased DLR. However, the effective DQE of the STEM detector (a photomultiplier tube) is higher compared to a CCD. There is also no modulation transfer function in STEM as the image is recorded point by point, increasing the contrast and hence the effective DLR. In this case, the increase in DQE and contrast in STEM is assumed to cancel out the decrease in F.

Few direct lattice images of organics have been achieved through STEM techniques, as dose increases with magnification (unlike CTEM), but one technique that has

provided several positive results in recent years is compressive sensing (Buban *et al.*, 2010, Stevens *et al.*, 2018). This technique functions by sampling only a fraction of a scanned area and using mathematical algorithms to fill in the remaining data. By only sampling a fraction of the sample area, only a fraction of the electron beam dose is applied to the sample, *i.e.* very little of the available dose budget is used. In the second part of this study (section 5.3.1), we will attempt to achieve direct lattice observation by BF-STEM.

Another technique which has been previously used to obtain lattice information in sensitive materials in both CTEM and STEM is through the use of moiré fringes (Su & Zhu, 2010). Moiré fringes are observed in electron microscopy when a crystal lattice and a reference lattice of a similar size overlap. The resultant interference pattern retains information from the base crystal lattice and can be observed at magnifications (and therefore electron doses) many times lower than would be required to directly resolve said base crystal lattice (Egerton, 2018). Moiré fringes acquired by STEM techniques are referred to as scanning moiré fringes (SMFs) and are the result of interference between a crystal lattice and the 'lattice' produced by the regular scanning motion of the electron beam. Disruption in these fringes can be interpreted as defects in the crystal structure (assuming no disruption to the scanned lattice), though the exact type, size, and location of such defects cannot accurately be determined due to the significant effects of rotational variance between scanned and real lattices (Williams, 2009). As such, care must be taken with interpretation.

The size of the produced general SMFs (d_{gm}) depend upon the magnification used (which determines the scanned pixel size and therefore the size of the scanned lattice (d_s)), the size of the base crystal lattice (d_l), and the offset angle between these two lattices (β). These factors are related by equation 5.2.

$$(5.2) \quad d_{gm} = \frac{d_l d_s}{\sqrt{(d_l - d_s)^2 + d_l d_s \beta^2}}$$

In the most basic of circumstances, the angle between the two lattices will be 0°, and a simplified equation (5.2) can be used to determine d_{tm} (translational moirés).

$$(5.3) \quad d_l = \frac{d_{tm} d_s}{d_{tm} + d_s}$$

As highlighted in Williams & Carter, 2009, small rotational and size variances between scanned and real lattices can drastically alter the size and rotation of the resulting moiré fringes. Additionally, as the size difference between d_l and d_s increases, the resulting moiré fringes become smaller. These relationships are shown in the graphs in figure 5.1 (S'ari *et al.*, 2019).
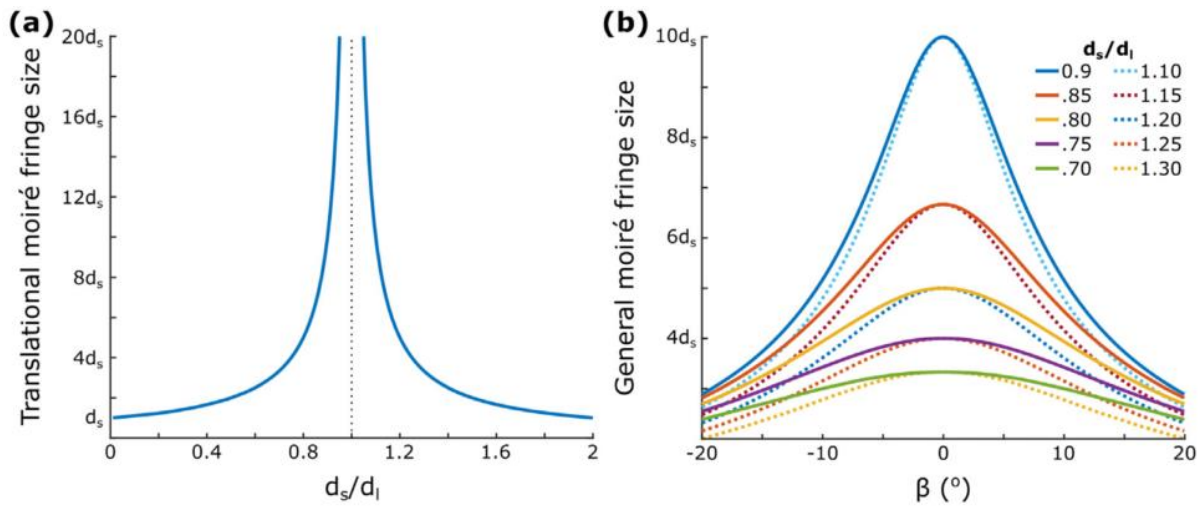
Fig.5.1: (a) Graph representing the size of the translational moiré fringes resulting from interference between scanned and real lattices with varying size ratios. As the ratio of sizes deviates from 1, the size of the moiré fringes decreases. (b) Graph representing the effect of changing β on the size of the resultant general moiré fringes with different d_s/d_l ratios. As β deviates from 0°, the size of the moiré fringes decreases. Graphs from S'ari *et al.*, 2019.

Care must also be taken when qualitatively analysing SMFs for the same reasons highlighted above. Figure 5.2 shows schematics for the formation of SMFs. Three

schematic combinations of a real defected lattice and a scanned lattice are shown, along with the moiré fringes that result from overlaying them. In figure 5.2(a), the scanned lattice is slightly smaller than the real lattice and the offset angle is 0°.
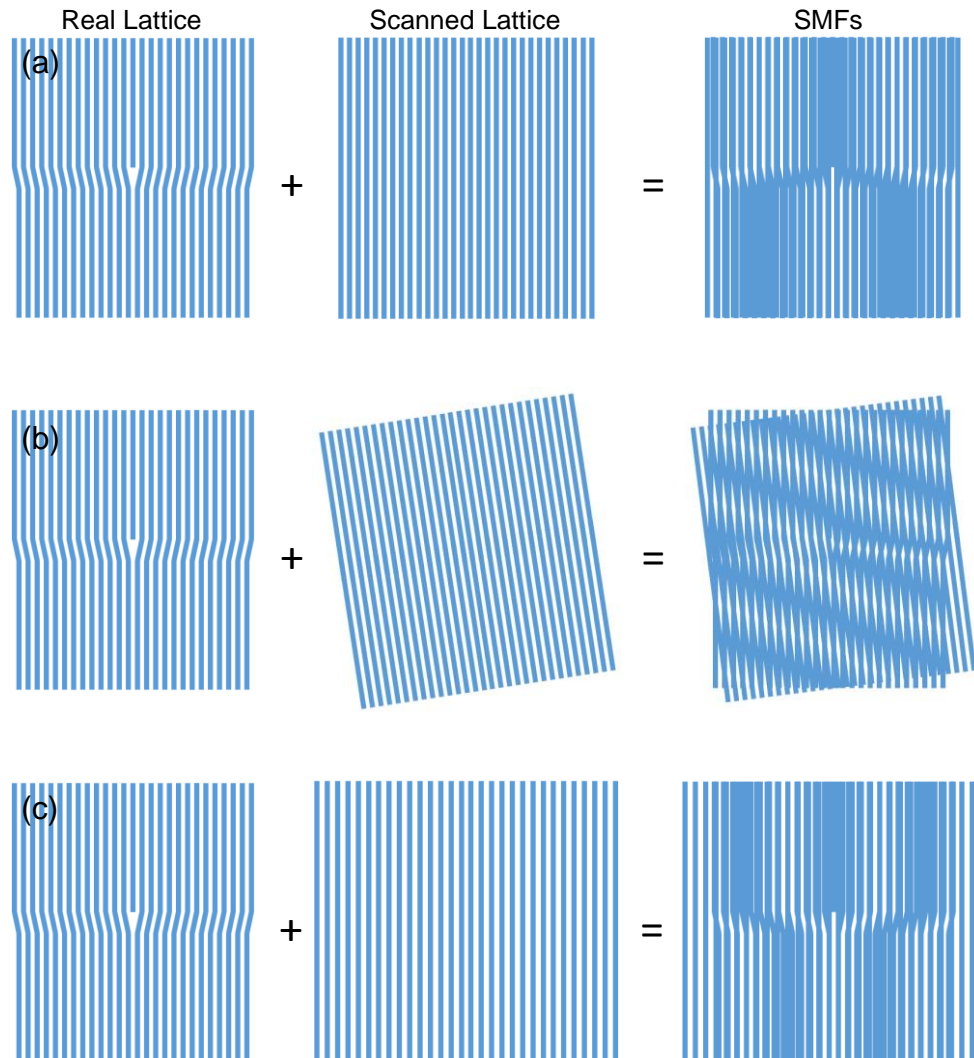
Fig.5.2: Schematic diagrams of moiré fringes formed from a defected lattice and (a) a lattice with smaller spacings than the defected lattice, (b) a rotated lattice, and (c) a lattice with larger spacings than the defected lattice. In (a), the resultant moiré fringes show the defect but in the opposite orientation. In (b), neither the type of defect nor the orientation are correct. In (c), the defect and its orientation are represented correctly.

The resultant moirés show a defect, but the orientation of this defect is inverted. Figure 5.2 (b) shows the combination of the same two lattices as in (a), but with the scanned lattice tilted, giving a non-zero β value. The defect is still observable in the moirés, but

the moiré fringe orientation is now offset from either base lattice. In 5.2(c), the scanned lattice is larger than the real lattice and β is 0°. The resultant moirés are oriented with the defect in the same orientation as the real lattice. For analysis of this kind of defect then, it would seem that using a scanned lattice with spacings slightly (d_s) larger than the real lattice is optimal (d_l). If the angle between them can successfully be brought to 0°, the resultant moirés produce an accurate magnification of the real lattices. This may not be possible depending on the real lattice under scrutiny and the magnification steps (pixel sizes) available in the STEM. For a more detailed discussion of moiré fringes, see S'ari *et al.*, 2019.

In the third section of this study (section 5.3.2), SMFs will be acquired and analysed in an attempt to acquire lattice and defect information about theophylline form II.

5.2 – Direct Lattice Observation with BF-TEM

Having determined critical fluences for theophylline form II under a number of microscope conditions (chapter 4), work could be done to attempt high-resolution phase contrast imaging, starting with BF-TEM. The critical fluence determined for theophylline form II at 300 kV, ambient temperatures, on a lacey carbon support film ($36.3 \ e^-Å^{-2}$) is the dose budget for these experiments. The major limitation of attempting high-resolution BF-TEM of such a sensitive material is the low electron flux available for imaging. Hence, the sensitivity of the camera becomes key. Neither of the TEMs present at Leeds (the FEI Tecnai TF20 with attached Gatan Orius SC600A CCD camera, and the Titan[3] Themis 300 with attached Gatan OneView 4k camera) proved sensitive enough to acquire high enough resolution images under such low flux conditions to be able to resolve lattices. Both cameras are CMOS detectors with DQEs of ~0.5 at best, thus reducing DLR compared to the Gatan K2.

The requirements for resolving and accurately defining fringes are twofold. Firstly, the Nyquist limit must be achieved, that being the necessity for a sampling interval (pixel size in this case) to be twice the spatial frequency of the feature (Williams & Carter, 2009). Without this, undersampling occurs, which prevents the accurate resolution of a feature. Secondly, the Rose criterion must be met, *i.e.* a signal-to-noise ratio of 3-5 is required to distinguish a feature with 100% certainty (Rose, 1974). These two requirements combined mean that there is a minimum magnification and a minimum electron flux that can be used to attempt to image the lattices in theophylline for a given camera type of known pixel size and DQE.

The most success by TEM was achieved with the Gatan K2 direct electron detection camera, which was briefly available for use on loan at the University of Leeds Faculty of Biological Sciences, attached to a Tecnai F20 TEM operated at 200 kV. Using this

setup and low-dose conditions, lattices were detected in the FFT of one of the BF micrographs, although they not directly observable. The reason for this is that FFT is the result of averaging over many unit cells, so any periodicity in a given area will be more easily observed this way compared to direct imaging (Kuo and Glaeser, 1975). The intensity in the FFT spots can be mathematically enhanced and inversed to produce a visualisation of the detected fringes.
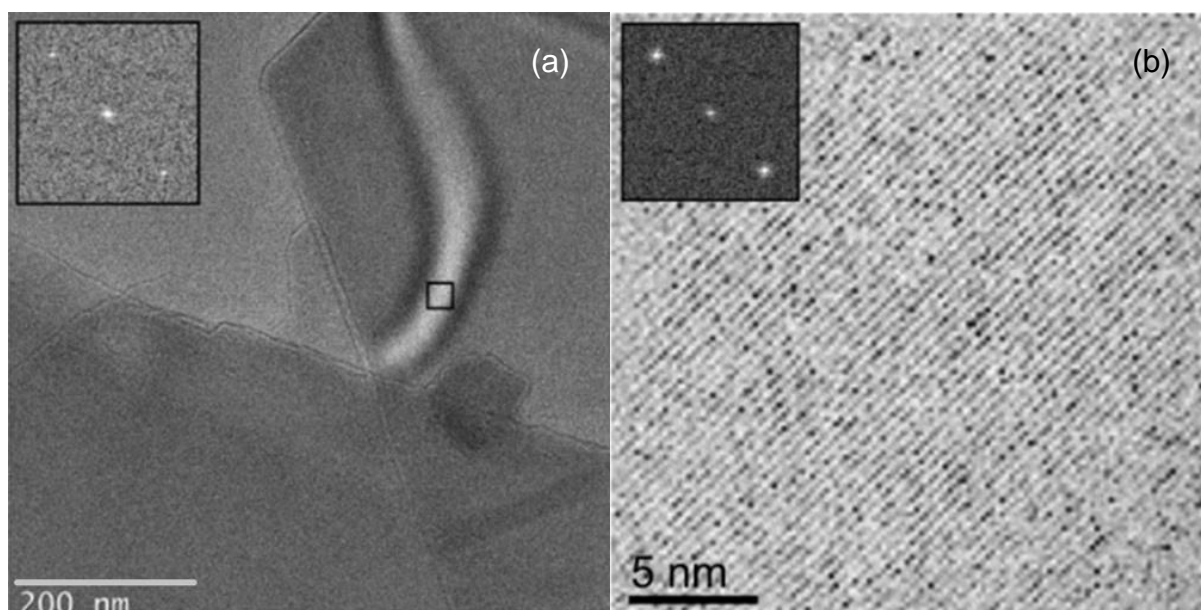
Fig.5.3: (a) BF-TEM micrograph of theophylline form II obtained using a Tecnai F2 and a Gatan K2 direct electron detection camera. Inset is the FFT from the highlighted area. (b) Inset is the FFT with 10 times intensity enhancement applied to the observed spots. The resulting inverse FFT shows the lattice fringes at higher magnification and improved contrast. Microscope conditions (magnification, electron flux, acquisition time) were manipulated to ensure critical fluence levels for theophylline at 200 kV and room temperature ($\sim$30 e$^-$Å^{-2}) were not exceeded.

Figure 5.3 shows the original BF micrograph obtained, alongside the FFT, the enhanced FFT, and the inverse FFT visualisation of the lattice. The enhanced FFT has had the intensity of the spots increased by 10 times relative to the background. The lattice spacings measure an average of 0.417 nm, closely matching the (002) spacing of theophylline form II (0.424 nm).

Figure 5.3 represents the only instance of direct lattice FFT spot acquisition and the subsequent inverse FFT of theophylline form II using the Gatan K2 direct electron detection camera during this study. The difficulty with which this was obtained highlights the challenging nature of direct lattice observations by BF-TEM of highly beam sensitive materials. Locating, focussing on, and imaging a sensitive material within a very limited dose budget is a considerable endeavour. Even the improved imaging capabilities of the K2 compared to more common cameras was not sufficient in most instances to meet both the Nyquist limit and Rose criterion without exceeding theophylline's critical fluence of ~30 e$^-$Å^{-2}. This inherent difficulty, combined with the high cost of cameras like the K2, make the prospect of mainstream analysis of this kind a difficult task.

Difficult, but not impossible. Recent results by Mark S'ari (presented at MMC 2019) on crocidolite asbestos (chosen because it is highly beam stable yet has large lattice spacings akin to an organic crystalline material) show the detection of lattices by FFT of BF-TEM micrographs at low electron fluences using a Gatan OneView 4K camera (figure 5.4). FFT spots of 0.32 nm spacings were observed in images taken with a total of 1 e$^-$Å^{-2} fluence at a flux of 10 e$^-$Å^{-2}s^{-1}. Though promising, these results were obtained only after a great deal of time had been invested, with the acquisition of focus at such low electron fluxes being the key limiting factor. Most results obtained were noisy and showed no visible or detectable fringes. Additionally, the asbestos used is highly beam stable, so observations would not suffer reduced resolution as a result of electron beam induced damage, unlike in organic crystalline samples.
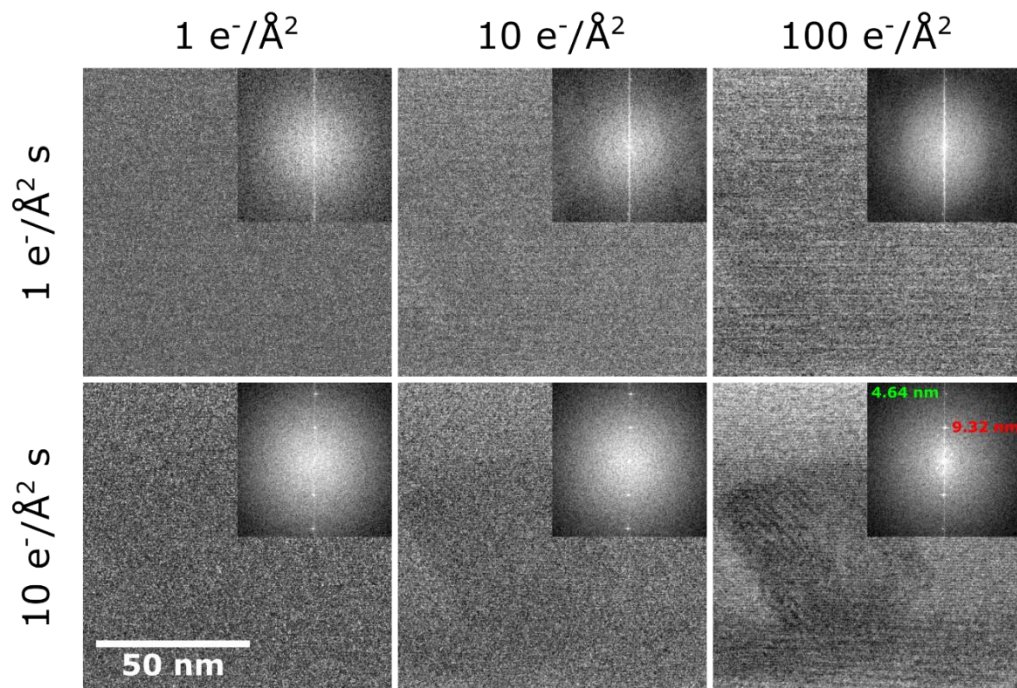
Fig.5.4: BF-TEM micrographs of crocidolite asbestos taken at different electron fluxes and total fluences, each with an inset FFT. At 1 e$^-$Å^{-2} fluence and 10 e$^-$Å^{-2}s^{-1} flux, spots are clearly observed in the FFT, but the asbestos lattice spacings do not become clear in the BF-TEM micrograph until a total electron fluence of 100 e$^-$Å^{-2} is used in image formation.

5.3 – Scanning Transmission Electron Microscopy

5.3.1 – Direct Lattice Observation by BF-STEM

While a similar DLR is theoretically obtainable in STEM as in CTEM (see section 5.1), the ability for focus to be carried out in an area separate from the imaging area (thus using up less of the dose budget prior to final image acquisition) should result in a slight improvement in DLR that is unobtainable in CTEM.
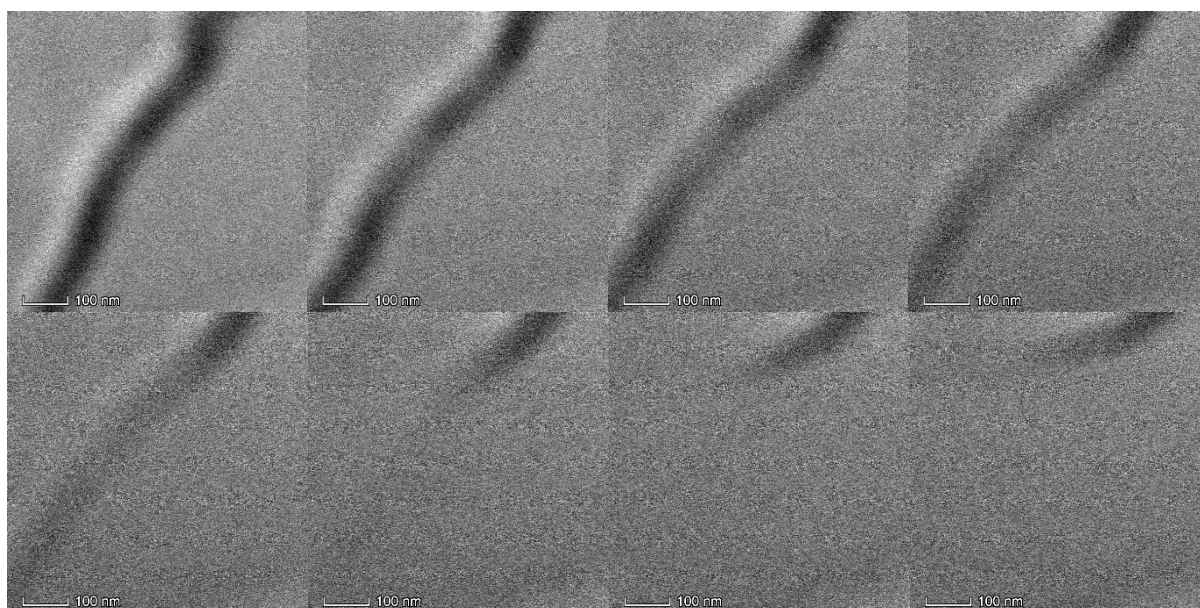
Fig.5.5: BF-STEM micrograph series of theophylline form II at 115k times magnification, 300 kV, room temperature, and an electron flux of 7.5 e⁻Å⁻² per scan. Total fluence for this series is therefore 60 e⁻Å⁻².

Conditions used for the STEM experiments were: 300 kV accelerating voltage, 4.5 kV extraction voltage, 10 mrad convergence semi-angle, and 5.5 mrad collection semi-angle (to achieve optimal phase contrast (Sader, 2010)). A monochromator was used to maintain an electron beam current of ~0.1 $e^-Å^{-2}$. As in TEM mode, bend contours are observed, which shift and disappear during exposure, indicative of a loss of crystallinity. The movement of the contours is due to stress applied to the crystal during irradiation and damage, causing physical distortion of the crystal itself.

With knowledge of the exact fluence applied per scan, a critical fluence for STEM mode was determined as ~50 e$^-$Å^{-2} (total loss of crystallinity, rather than 1/e of maximum diffraction spot intensity). This was determined by observation of bend contours over multiple scans, and the critical fluence was estimated based on the point at which the contours disappeared. One of the BF-STEM micrograph series used in the determination of the critical fluence is shown in figure 5.5. This critical fluence is higher than that calculated for theophylline form II using CTEM at 300kV and room temperature (36.3 ± 8 e$^-$Å^{-2}). Various damage effects act differently in STEM mode compared to CTEM mode (Egerton, 2004), and are possible sources of the discrepancy between the measured critical fluences. Hooley *et al.* (2019) noted an increased damage fluence for calcite when imaged by BF-STEM compared to BF-TEM.

Figure 5.6 shows a HAADF-STEM image of a theophylline crystal, with bend contours visible across it, and a damaged region exposed to the beam at a higher magnification in the centre of the image. Because of the limitation that is the high dose sensitivity of the sample, direct lattice imaging of theophylline form II by STEM was found to be difficult with the equipment available (the Titan^3 Themis 300 at the University of Leeds and the Nion UltraSTEM 100 at SuperStem). Although difficult, certain positive results were achieved, chief among which was a result of similar resolution to the BF-TEM image acquired by use of the Gatan K2 camera (figure 5.7). Despite the lower DQE of the BF-STEM detector used for this STEM experimentation, the dose budget saved by focussing the probe away from the imaged area preserved the sample enough for a direct lattice image to be acquired, if only just.
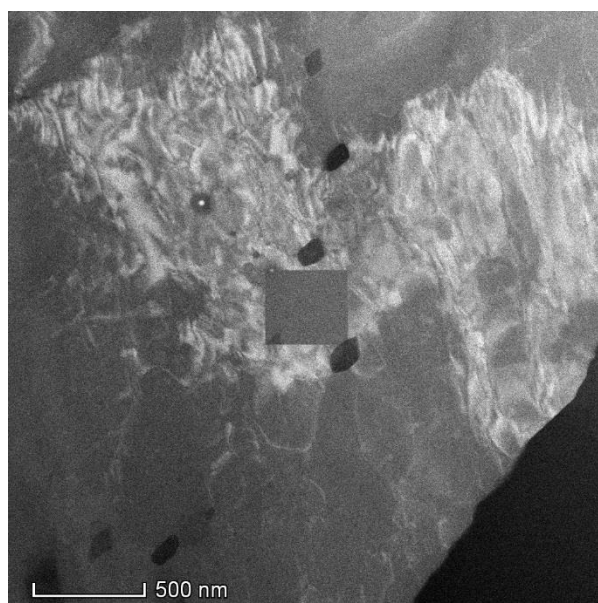
Fig.5.6: HAADF-STEM image of a theophylline form II crystal at 10k times magnification, showing a large area covered by bend contours and a region in the centre which has been scanned at a higher magnification, resulting in disruption of the bend contour in this area. Crystallinity was lost due to beam exposure exceeding the critical fluence. Image acquired at 300 kV and ambient temperature.

Figure 5.7 shows a BF-STEM image of an area of a theophylline form II crystal. The raw BF image shows a number of different fringes, though small enough that they are difficult to pick out without image enhancement. An FFT is used to confirm the presence of these fringes. The smaller fringes measure 0.34 nm, a good match to the theophylline form II (011) spacing which is commonly seen in diffraction patterns from plates in this orientation. At the magnification used, these fringes are at the Nyquist resolution limit of the image, hence their FFT spots are right on the outer edge of the FFT. Due to their size and low contrast of the source micrograph, enhancing the spot contrast and inverting the FFT, in a similar fashion to the inverted FFT in figure 5.3, does not improve the visibility of the fringes. As such, they can only be identified by the FFT. The larger spacings identified in the FFT (as marked by blue arrows) measure 0.57 nm, which could be representative of the (400) spacings. They are more likely

110

moiré fringes however, as the sample is known to be oriented with the [100] axis parallel to the electron beam so {h00} fringes should not be visible. As discussed in section 5.3.2, these moiré fringes are a useful observational tool for beam sensitive samples.
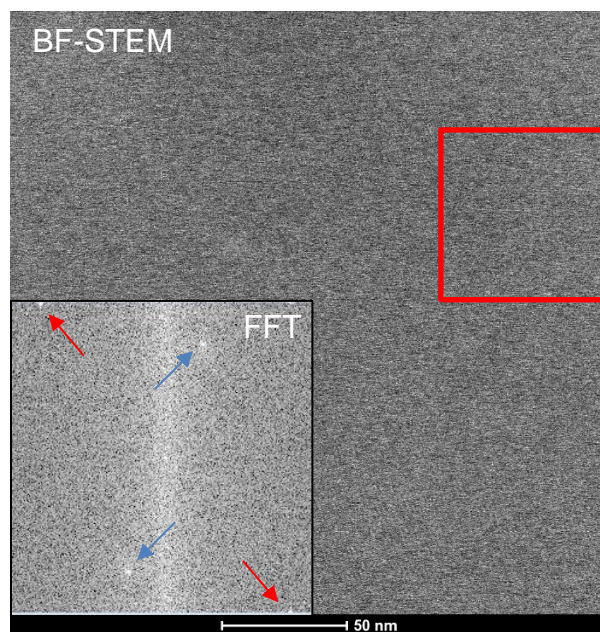
Fig.5.7: BF-STEM micrograph of theophylline form II with (inset) an FFT of the area outlined in red. Micrograph taken at 330k times magnification. The FFT shows two pairs of spots, indicative of the presence of lattice spacings. The smaller spacings (represented by the furthest separated pair of FFT spots, as marked by red arrows) fall on the resolution limit. These spots measure 0.34 nm, representative of the (011) spacing of theophylline form II. The micrograph was taken at 300 kV and ambient temperature, with a total fluence of 45 e⁻Å⁻².

5.3.2 – Moiré Fringe Observations in BF-STEM

While some success was achieved with direct lattice imaging using low-fluence conditions, such successes were few and far between. SMFs characterisation was attempted next, as the lower magnification at which SMFs can be acquired is beneficial to maintaining the stability of the sample. Numerous moiré fringes had already been

observed in theophylline form II up to this point, so acquisition was not difficult. The difficulty lies with finding the appropriate orientation of the SMFs in order to acquire a close match between the base crystal lattice and the resultant moiré fringes, as schematised in figure 5.2.
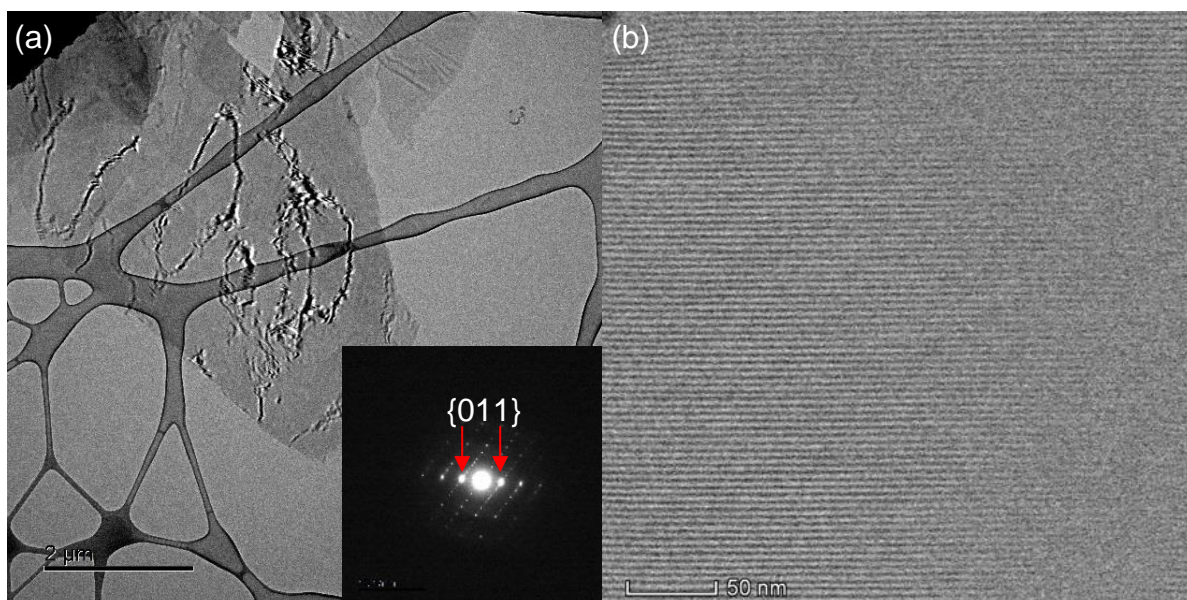
Fig.5.8: (a) BF-STEM micrograph at 4.3k times magnification showing a theophylline form II crystal with bend contours and inset diffraction pattern confirming it as having the (100) plane perpendicular to the beam direction. (b) a BF-STEM micrograph of the crystal shown in (a) at 225k times magnification and a fluence of 15 e⁻Å⁻². Moiré fringes measuring 4.38 nm are visible throughout.

It is possible to target a specific real lattice and orient the sample such that those lattice spacings are parallel to the scan direction of the electron beam, thus bringing β as close to 0° as possible. This is done by taking a diffraction pattern of a target crystal in CTEM and orienting the sample based on the chosen spots from this pattern. The STEM magnification which gives a pixel size closest to the size of the lattice spacings represented by the chosen diffraction spots can then be used to form translational moiré fringes. Figure 5.8 shows a successful application of this method.

Figure 5.8 (a) shows a BF-STEM micrograph of a theophylline form II crystal and inset diffraction pattern representative of the <100> zone axis. The sample was oriented such that the {011} spacings (highlighted by red arrows) were aligned vertically *i.e.* the {011} lattice spacings are horizontal relative to the camera, the same as the scanned electron beam in STEM mode. The {011} spacings are 0.34 nm in size. The closest pixel size to this is obtained when the STEM magnification is set to 225k times, giving a pixel size of 0.33 nm. Figure 5.8 (b) shows the resulting BF-STEM micrograph of a region of the crystal in (a), showing horizontal moiré fringes throughout. Measured directly from the image, these fringes are 4.38 nm wide, larger than any real spacing of theophylline form II (or indeed any stable anhydrous form of theophylline, see Appendix A), confirming their identity as moiré fringes.

Using the equations outlined in section 5.1, it is possible to determine whether or not the real lattice fringes were aligned perfectly with the scanned lattice. This can be done by using equation 5.1 and a d_l value of 0.341 nm, the spacing measured for the lattice spots aligned parallel to the scan direction from the diffraction pattern in figure 5.6 (a). The result of this calculation can then be compared by using equation 5.2 and a d_{tm} value of 4.38 nm, as measured directly from the fringes in figure 5.8 (b). d_s is a consistent value of 0.329 nm, from the pixel size at 225k times magnification, and β is assumed to be 0 radians. A non-zero β will be obvious if there are mismatches in d_l and d_{gm} values between the two equations.

$$(5.4) \quad d_{gm} = \frac{d_l d_s}{\sqrt{(d_l - d_s)^2 + d_l d_s \beta^2}}$$

$$d_{gm} = \frac{0.341 \times 0.329}{0.341 - 0.329}$$

$$\boldsymbol{d_{gm} = 9.34 \, nm}$$

$$(5.5) \quad d_l = \frac{d_{tm}d_s}{d_{tm} + d_s}$$

$$d_l = \frac{4.38 \times 0.329}{4.38 + 0.329}$$

$$\boldsymbol{d_l = 0.306\ nm}$$

The calculated values of d_{gm} and d_l both differ from the values observed experimentally, suggesting that there is an angular mismatch between the scanned lattice and the real crystal lattice. This angle can be estimated by trial-and-error use of equation 5.1, inputting an arbitrary value for β and correcting until d_{gm} is as close to the experimentally measured value, 4.38 nm, as desired. Doing so produces an estimate β of 0.00456 rads or 0.26°. For such a small misalignment of the lattices to cause such a drastic impact to the observed moiré fringe spacings suggests that obtaining information with a β of precisely 0 radians is unlikely.

As highlighted in Williams & Carter, 2009, and shown in figure 5.1(b), small rotational and size variance between scanned and real lattices can drastically alter the size and rotation of the resulting moiré fringes. This has a similar effect on the appearance, in the moiré fringes, of lattice defects present in the real crystal lattice. Figure 5.9 shows moiré fringes of an area of theophylline form II crystals. In the area highlighted, the fringes are disrupted by what appears to be a planar dislocation.

Though it appears in the moiré fringes as a planar dislocation, this disruption could be any one of a number of lattice defects, as the scan direction is rotated relative to the lattice spacings. Without knowing the angle or size difference between the scanned and real lattices, potential interpretation of this single defect is limited. However, it does highlight a success in identifying a defect in theophylline form II through means other

than the diffraction pattern or FFT, which themselves only identify repeated defects, rather than individual defects. Extension of this technique to pharmaceutical materials could be useful for characterising defect density of crystalline formulations and could be an effective technique for optimisation of formulation methods.
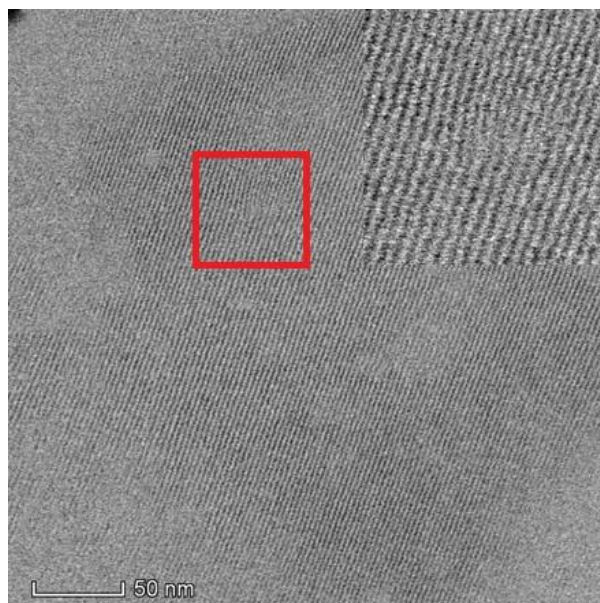
Fig.5.9: BF-STEM micrograph of theophylline form II showing moiré fringes. The highlighted area is magnified (inset) to emphasise the presence of a disruption in the fringes. Acquired at 300 kV accelerating voltage and ambient temperature.

5.4 – Summary

This study has shown the successful acquisition of lattice information of theophylline form II by direct and indirect observation in CTEM and STEM, though few results were obtained relative to the time spent observing samples.

Through the use of a Gatan K2 direct electron detection camera with a much improved DQE compared to CMOS cameras, it was possible to resolve theophylline form II lattices to a degree that they could be identified by the FFT the BF-TEM image. The spacing measurement closely matched the (002) spacings of theophylline form II.

Theophylline form II lattices were also barely resolvable in BF-STEM by low-dose techniques, also requiring the use of an FFT of the image for identification. The observed 0.34 nm could be representative of the {011} planes.

Most success was achieved by the acquisition and analysis of SMFs, with the observation of a magnified lattice defect in one instance, and the development of techniques to orient the sample such as to minimise the offset angle, β, between the base crystal lattice and scanned lattice. We have published this work in S'ari *et al.*, 2019, and extended it to include the successful analysis of SMFs in furosemide and felodipine, two highly beam sensitive organic crystalline materials with pharmaceutical properties (critical fluences of 7.1 ± 4.0 e$^-$Å^{-2} and 2.1 ± 0.9 e$^-$Å^{-2} respectively). Multiple defects were identified in both of these samples, highlighting a potential use of SMF analysis in understanding the effects of pharmaceutical formulation methods on pharmaceutical materials.

Suspected moiré fringes were also observed in TEM micrographs by Hasa *et al.* (2016) in cocrystals of caffeine and glutaric acid produced by polymer-assisted grinding. However, this requires the presence of overlapping crystals to generate

moirés, limiting the applicability of CTEM for this type of analysis.

While the results presented here and in S'ari *et al.* (2019) show promise, it is important to emphasise the amount of time and effort it took to acquire these relatively few positive results. Acquisition of lattice fringes, whether directly or indirectly, in highly beam sensitive organic crystalline materials is exceptionally difficult, even when using the most up-to-date equipment. As this equipment becomes more readily available and more microscopists become familiar with analysing materials of this type however, characterisation of industrially relevant beam sensitive organics may well become commonplace and useful.

Chapter 6 – Investigation of a Beam Sensitive Inorganic: Determination of Sn Atom Locations Within the Sn-beta Zeolite Structure

6.1 – Background and Initial Observations
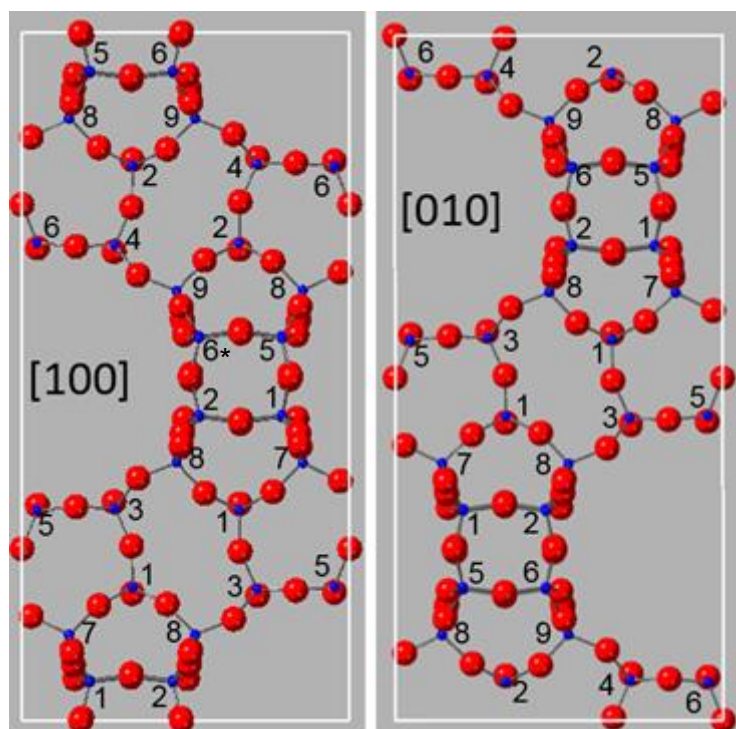
Fig.6.1: Schematics of the Si-beta zeolite (polymorph A) pore structure observed down the [100] and [010] directions, with different tetrahedral Si sites (T-sites) labelled 1 to 9. Red atoms are O, while blue atoms are Si. T-site locations based on 90° clockwise rotation from [100] to [010] orientation. Only topmost T-sites are labelled.

Zeolites are microporous aluminosilicate materials with well-defined and controllable pore sizes that are widely used for their catalytic properties. Their inherent porosity gives them high surface areas and allows for the incorporation of other reactive ionic species which aid in or activate catalytic activity and selectivity (Bhatia, 1989). The material of interest to this study is a dealuminated Si-beta zeolite doped with Sn, which has been shown to be a promising catalyst for a wide range of industrial-scale reactions (Corma *et al.*, 2002; Holm *et al.*, 2010; Moliner *et al.*, 2010).

Figure 6.1 shows a unit cell schematic of polymorph A of Si-beta (a dealuminated β-zeolite), the base material into which Sn of differing concentrations is doped. For a view of the extended zeolite structures, see figure 6.2. The crystal system is tetragonal with a P4₁22 space group and unit cell parameters $A = B = 12.6614$ Å and $C = 26.4061$ Å. All angles are 90°. The sites labelled 1-9 are the T-sites (tetrahedral sites based on the SiO_4 network), energetically distinct atomic positions within the structure of the beta zeolite. Only the topmost T-sites are labelled in figure 6.1. Other T-sites are present in each atomic stack underneath those labelled. For example, underneath the marked T-6 site in the [100] orientation is a T-4 and a T-2 site. Understanding the 3-dimensional layout of the T-sites will be important for identifying those sites potentially occupied by metal dopants.

One downside to using TEM techniques to characterise this particular zeolite is the inability to distinguish between the [100] and the [010] zone axes by either direct structural observations or by diffraction pattern analysis. In tetragonal crystal systems like Si-beta zeolite, these axes are symmetrically equivalent. The [100] and [010] zone axes structures are shown in figure 6.2, along with simulated diffraction patterns for both. Without prior knowledge of which zone axis is being observed, it is impossible to distinguish between the two. In retrospect, this issue makes identification of specific T-sites by TEM methods difficult, as identification of Sn at a particular site in either axis could potentially be one of a number of T-sites. The site would only be completely identifiable if the same site could be observed in the other zone-axis by 3D positional determination. Due to the zeolite's sensitivity to the electron beam and the crystal morphologies, this is an unlikely prospect for current equipment and methods.

To date, there has yet to be conclusive evidence acquired which identifies the specific T-site or sites which Sn occupies upon inclusion into the zeolite structure. Numerous
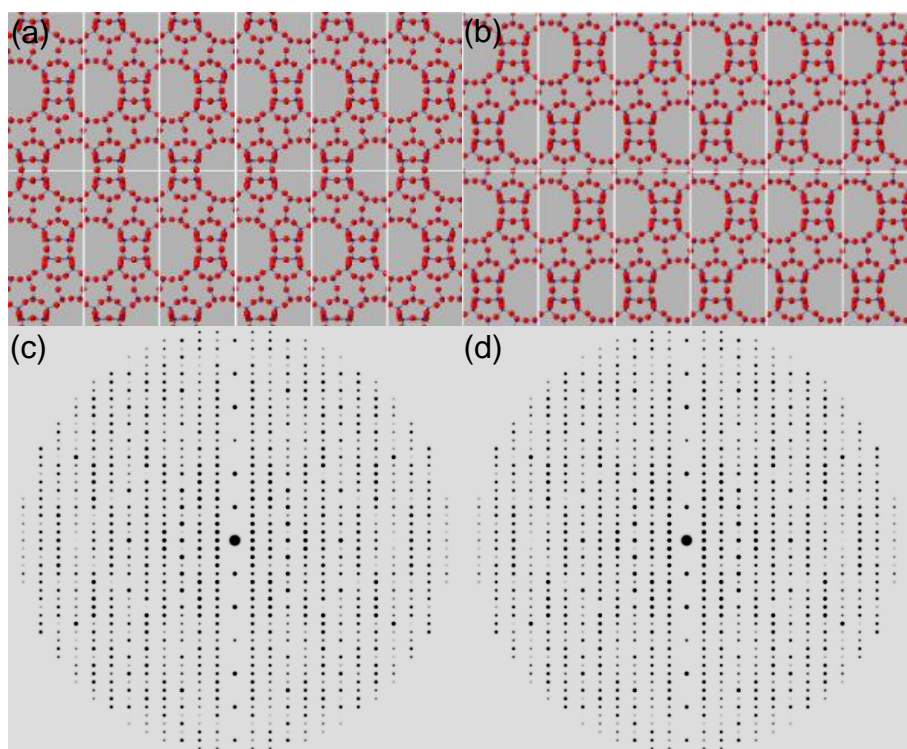
Fig.6.2: (a-b) Schematics of the atomic structure of Si-beta zeolite polymorph A, viewed down zone-axes [100] and [010] respectively. (c-d) Simulated diffraction patterns of the respective zone-axes.

studies have previously been carried out in attempts to determine this. Shetty *et al.* (2005) and Yang *et al.* (2013) used DFT to determine the most energetically preferential site for Sn occupancy and both found that the T-2 site was preferable. Bare *et al.* (2005), using multishell fit modelling of EXAFS, found that Sn was substituted as pairs into the T-1 and T-2 sites on opposite sides of a pore. While each of these studies considered closed atomic sites (*i.e.* the stable zeolite structure as shown in figure 6.1), Josephson *et al.*, 2017, studied open sites (*i.e.* ionised sites), also using DFT. They found that the T-1 and T-9 sites were preferential for Sn occupancy. More recently, Kolyagin *et al.* (2018) used magic-angle spinning nuclear magnetic resonance analysis on Sn-beta samples, and found the T-5, T-6, and T-7 sites to be the most populated by Sn.

Experimental techniques based on electron microscopy are utilised here, rather than computational methods, in an attempt to empirically determine the location of Sn in two Sn-beta zeolite samples prepared by different means. The main challenge with this approach is the electron beam sensitivity of beta zeolites. While these materials are more stable under the beam than organics like theophylline, the sensitivity of the siliceous materials is significant enough such that the high-resolution (and therefore total electron fluence) analysis required to identify specific atomic sites and their elemental occupancy could prove difficult (Wang *et al.*, 2000). Also of concern is the high density of stacking faults typical of beta zeolites, which can affect the interpretation of direct lattice imaging as well as diffraction data (Newsam *et al.*, 1988).

The samples used in this study were a Sn-free Si-beta zeolite and a 1:100 Sn:Si ratio sample prepared by hydrothermal synthesis (HS) methods given in Tolborg *et al.* (2014) and a Sn-containing zeolite prepared by solid-state ion-exchange (SSIE) as per Hammond *et al.* (2012).

A critical fluence for Sn-beta (HS) was determined by the same methods used for theophylline in chapter 4 *i.e.* measurement of the decay in diffraction spot intensity with respect to accumulated electron fluence. Examples of the first and last diffraction patterns in one of the series used to calculate critical fluence are shown in figure 6.3. A critical fluence of 17,000 $e^-Å^{-2}$ was calculated with a standard deviation of ± 8,000 $e^-Å^{-2}$. The high standard deviation is likely a result of the highly variable crystalline environments possible in this sample, mostly in terms of crystal thickness, with thicker crystals taking longer to structurally decay under beam exposure. The measured critical fluence is within a reasonable range of critical fluences measured for other zeolite materials previously, such as the three measured amorphisation fluences by Wang *et al.* (2000) of zeolites analcime (7,000 $e^-Å^{-2}$), natrolite (18,000 $e^-Å^{-2}$), and

zeolite-Y (34,000 e$^-$Å^{-2}). These measurements were also made by diffraction pattern analysis, but at 200 kV accelerating voltage rather than 300 kV, and critical fluences were measured at the point of complete diffraction pattern fade out, rather than at $\frac{1}{e}$ of the highest intensity of the average of each spot. Despite these differences, the critical fluences are roughly comparable and within the same order of magnitude. Though the critical fluence of Si-beta is much higher than that of theophylline form II, low-fluence conditions are still required to avoid damage and eventual complete degradation of the crystal structure.
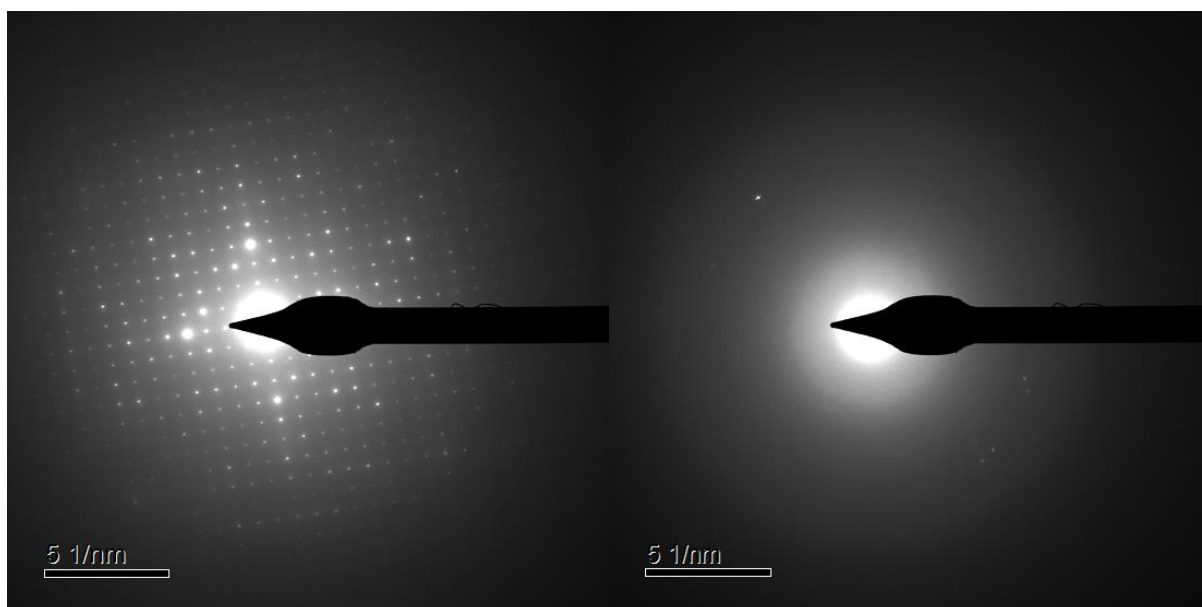
Fig.6.3: The first and last diffraction patterns of an exposure series from the same area of a Sn-beta (HS) zeolite crystal. [001] zone-axis. The critical fluence measured from this particular diffraction pattern series was 7500 e$^-$Å^{-2}. Acquired at 300 kV, ambient temperature, and with a 40 μm selected area aperture.

Radiolysis is the primary mechanism by which beam induced damage occurs in these zeolite materials (Treacy *et al.*, 1987). Additionally, while knock-on damage is less likely in silicon based zeolites compared to organic materials such as theophylline (due to Si atoms having a higher knock-on threshold energy than C atoms), at the low

electron beam currents used in these experiments radiolysis is still the dominant damage mechanism (Ugurlu *et al.*, 2011).

6.2 – Confirming Sn content

A combination of low-resolution SEM and TEM, as well as EDX analysis, was used to confirm the presence (or lack) of Sn in the three samples of beta zeolite used in this study. SEM and TEM micrographs are sufficient for Sn content confirmation in this case, due to the effects of Sn on the morphology of the crystals, with higher concentrations of Sn causing greater degrees of flattening of the square bipyramidal structure typical of Si-beta (Tolborg *et al.*, 2014). This effect is shown in figure 6.4.
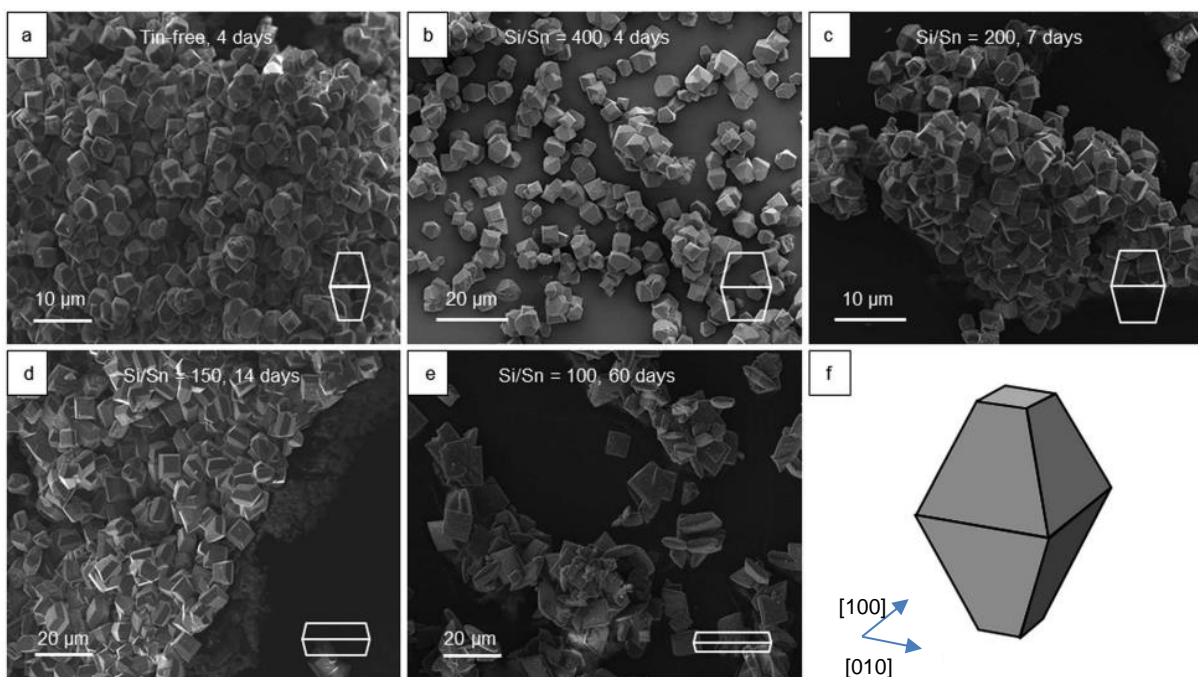
Fig.6.4: (a-e) SEM micrographs of zeolite materials produced by HS using different ratios of Si to Sn, from no Sn content in (a) up to a Si/Sn ratio of 100 in (e). Increased Sn content causes the resultant crystals to flatten, as depicted by the schematics in the bottom right of each image. Increased Sn content also increases the required synthesis time. (f) shows a 3D schematic of a Si-beta zeolite crystal. (Figure from Tolborg *et al.*, 2014).

Further experimentation by Tolborg *et al.* (2014) confirmed that the observed morphological changes reported in figure 6.4 were a result of the incorporation of Sn into the crystal structure causing changes in directional growth rates, as opposed to

the effects of changes in pH during synthesis with different Sn source concentrations.

6.2.1 – Scanning electron microscopy
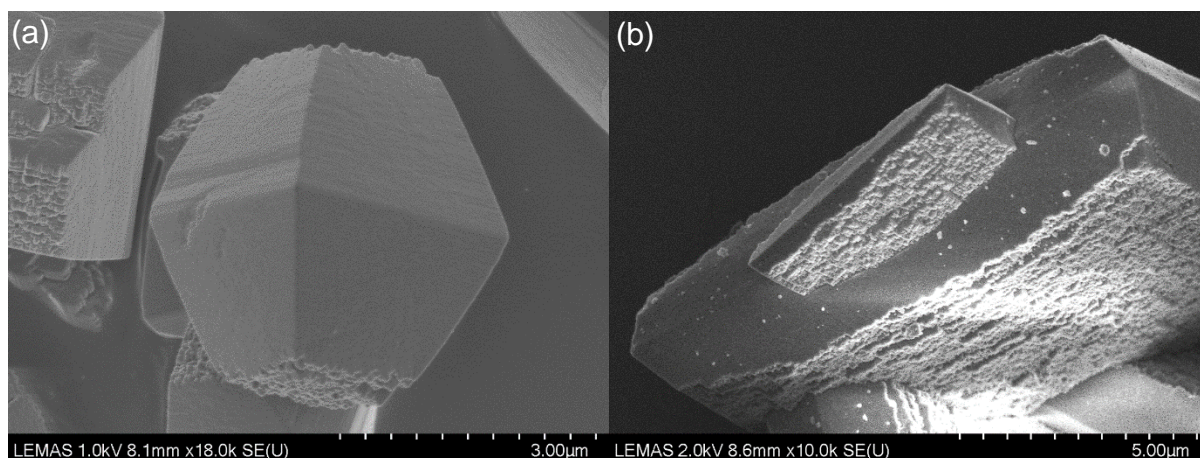
Fig.6.5: (a) SEM micrograph of Si-beta crystals, whose structures conform to the expected square bipyramid shape. (b) SEM micrograph of Sn-beta (HS). The square bipyramid structure has taken on a flattened form due to the effects of Sn on the structure. Numerous particles cover the surfaces of the crystals, suspected to be leftover Sn from the synthesis, present in the form of SnO_2 particles. Acquired with a 1 kV beam acceleration and at ambient temperatures.

The results of SEM of the Si-beta and the Sn-beta (HS) samples analysed here, shown in figures 6.5 (a) and (b) respectively, conform to the expected square bipyramidal morphology, as in figure 6.4. Si-beta, shown in figure 6.5 (a), shows the square bipyramidal structure of crystals several micrometres in size, with relatively smooth side faces and rough top and bottom faces ((001) planes). Figure 6.5 (b), the Sn-beta (HS) sample, shows the flattened structure expected, with much larger (001) planes. In addition, several fine particles are observed on the surfaces of the crystals. At this stage, these were assumed to be SnO_2 particles, produced from excess Sn supplied during the synthesis.

While the morphologies are as expected, the SEM results raised a concern going forward with high-resolution TEM analysis, namely the size of the crystals. Complete crystals would be near impossible to transmit an electron beam through, thus TEM analysis would have to rely on observations made at the edges of the crystals. Otherwise, sonication or other size reduction methods like grinding or milling could be implemented to break apart the crystals.

LEMAS 1.0kV 8.0mm x22.0k SE(U) 2.00µm
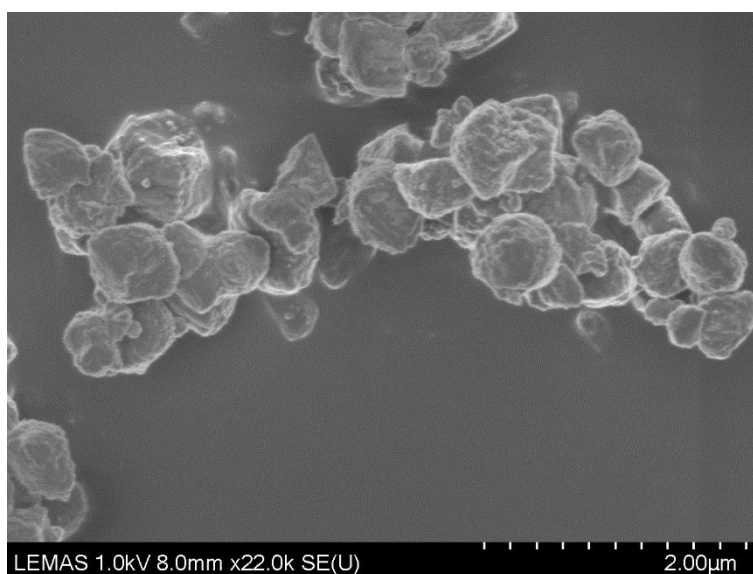
Fig.6.6: SEM micrograph of Sn-beta (SSIE). The mechanical grinding of these particles has reduced their size and the square bipyramid structure is lost. Acquired with a 1 kV beam acceleration and at ambient temperatures.

Figure 6.6 shows an SEM micrograph for the Sn-beta zeolite produced by SSIE. This sample is made up of smaller crystallites with a non-uniform, roughly spherical morphology. The smaller size might make this sample the easiest to acquire high-resolution images of, but the mechanical grinding used to increase the efficacy of SSIE is likely to have introduced a high density of lattice defects, which would be particularly disruptive to the acquisition of images showing the pristine pore structure of beta zeolites.

6.2.2 – Transmission electron microscopy

Figures 6.7 (a), (b), and (c) show low magnification BF-TEM micrographs of Si-beta, Sn-beta (HS), and Sn-beta (SSIE) respectively. As suspected, a complete crystal of Si-beta (figure 6.6 (a)) is too large for electron beam transmission, even with a relatively small crystal (~500 nm in diameter). Despite this, the uneven areas of contrast toward the top and bottom of the crystal show some regions that are thin enough for electron beam transmission. For high-resolution experiments, these areas would prove useful.
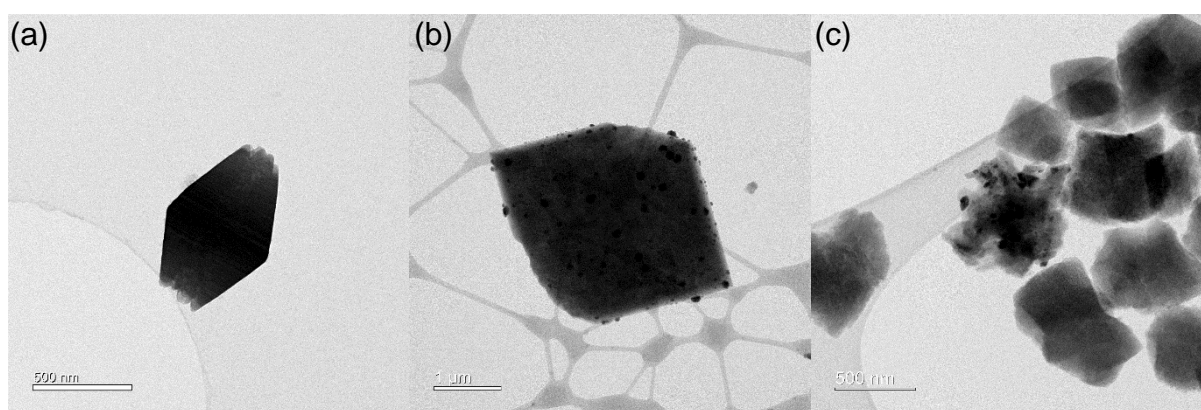
Fig.6.7: BF-TEM micrographs of (a) Si-beta, (b) Sn-beta (HS), and (c) Sn-beta (SSIE). (a) displays a profile view of the square bipyramid structure, and the contrast gradient across it gives an idea of its thickness, with areas towards the top and bottom edges showing some electron transparency. (b) displays a profile view of a crystal down the [001] axis. The crystal is covered in dense nanoparticles, suspected as being SnO_2. In (c) multiple smaller crystals are observed with a less consistent morphology. The central crystal has several dense particles attached, unlike the crystals that surround it. These particles are also likely SnO_2. Micrographs acquired at 300 kV beam acceleration.

Figure 6.7 (b) shows a BF-TEM micrograph of a crystal of Sn-beta zeolite prepared by HS, observed down the [001] axis. Though larger than the Si-beta crystal shown in figure 6.7 (a), the altered morphology of the Sn-beta makes the [001] direction thin enough for electron beam transparency. The pore structure of Sn-beta is only visible

when observed down the [100] or [010] directions. As such, any attempts to image the pores would have to rely on tilting of the sample stage in order to bring one of those axes into alignment with the electron beam. Also visible in this micrograph are many dense particles covering or perhaps incorporated into the crystal. Considering the synthesis method, these are likely to be SnO_2 nanoparticles left over from production. EDX will be used to confirm the elemental content of these particles.

Figure 6.7 (c) shows a BF-TEM micrograph of several Sn-beta (SSIE) crystals. These crystals are smaller than crystals in either of the other two samples and are also less uniform in morphology. This is as a result of the mechanical grinding applied to the sample during synthesis. The central crystal in this image shows multiple dense particles, similar to those seen in figure 6.7 (b). Again, these particles are suspected to be SnO_2 nanoparticles, for which EDX will be used to confirm, as detailed in section 6.2.3. The central crystal is the only one which shows the presence of these particles. During synthesis of these particles, dealuminated zeolite and tin(II)acetate are mixed together and are subject to mechanical grinding to encourage the incorporation of Sn into the zeolite by SSIE, prior to calcination at 500°C. The accumulation of SnO_2 around only one zeolite particle could indicate a non-homogeneous mixing of the tin(II)acetate during grinding, which could affect the concentration of Sn in each zeolite particle.

6.2.3 – Energy dispersive X-ray spectroscopy

Although the spatial resolution of EDX is sufficient to identify the localised presence of Sn ions in the crystal structure, the electron dose required to produce a sufficient X-ray signal at high-resolution would destroy the crystal structure before acceptable data

acquisition could occur. Despite this, EDX can still be used to confirm the presence, or lack, of Sn in each particle, and can also be used to confirm the composition of the additional fine particles and any impurities seen in the Sn-beta samples.

Figures 6.8 to 6.10 respectively show the STEM-EDX maps and spectra for regions of Si-beta, Sn-beta (HS), and Sn-beta (SSIE) respectively. The maps and spectra confirm that the Si-beta sample (figure 6.8) is devoid of Sn, with detection levels of Sn being no greater than background noise levels (represented by the Ti *Kα* map in figure 6.8 (e)). The EDX maps and spectra for the Sn-beta samples show increased levels of Sn throughout the scanned areas, as well as high concentrations of Sn in high density clusters (figure 6.9 (d)). Oxygen levels within these clusters are similar to the levels throughout the entire crystal. These observations suggest the composition of the fine particles seen in SEM and TEM (figure 6.5 (b), 6.7 (b), and 6.7 (c)) as Sn_xO_y.
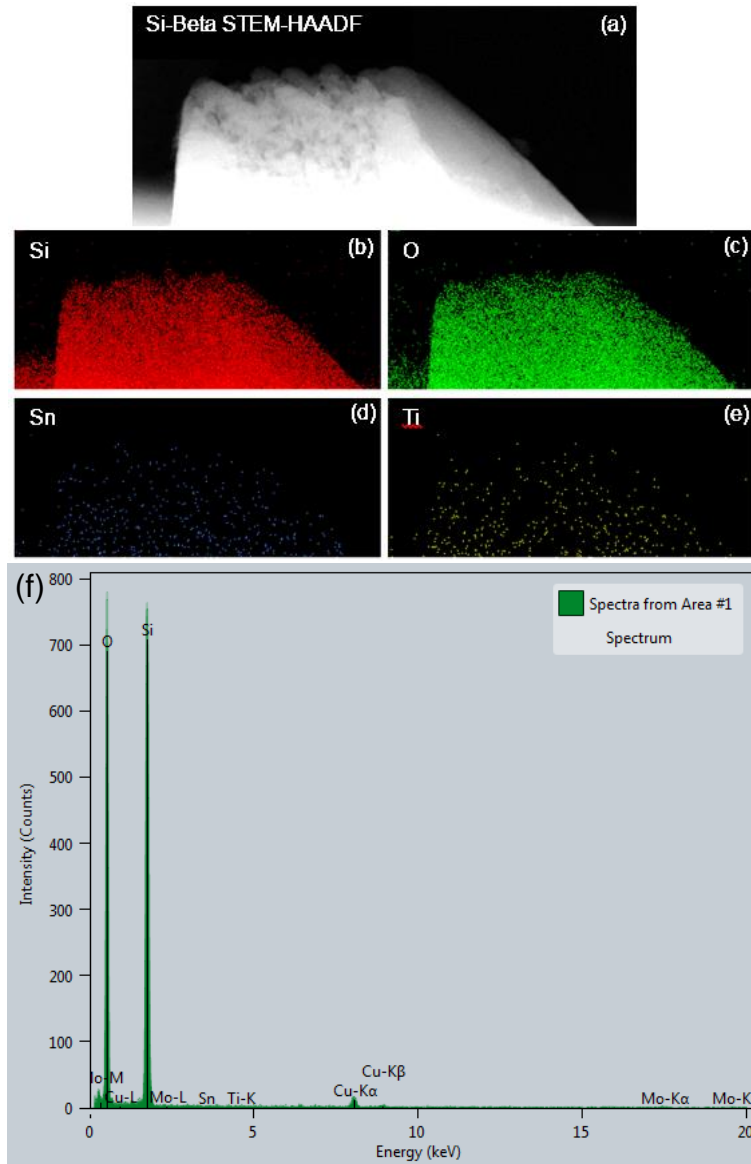
Fig.6.8: (a) STEM-HAADF of a Si-beta crystal. (b – e) *Kα* EDX maps for Si, O, Sn, and Ti respectively. Sn levels are comparable to background noise levels, represented here by the Ti map. (f) EDX spectrum of the whole scanned area in (a). Si and O levels are high and roughly even, while Sn levels are no higher than background levels, suggesting the expected SiO elemental composition. The slight Cu peak is likely from internal TEM components.
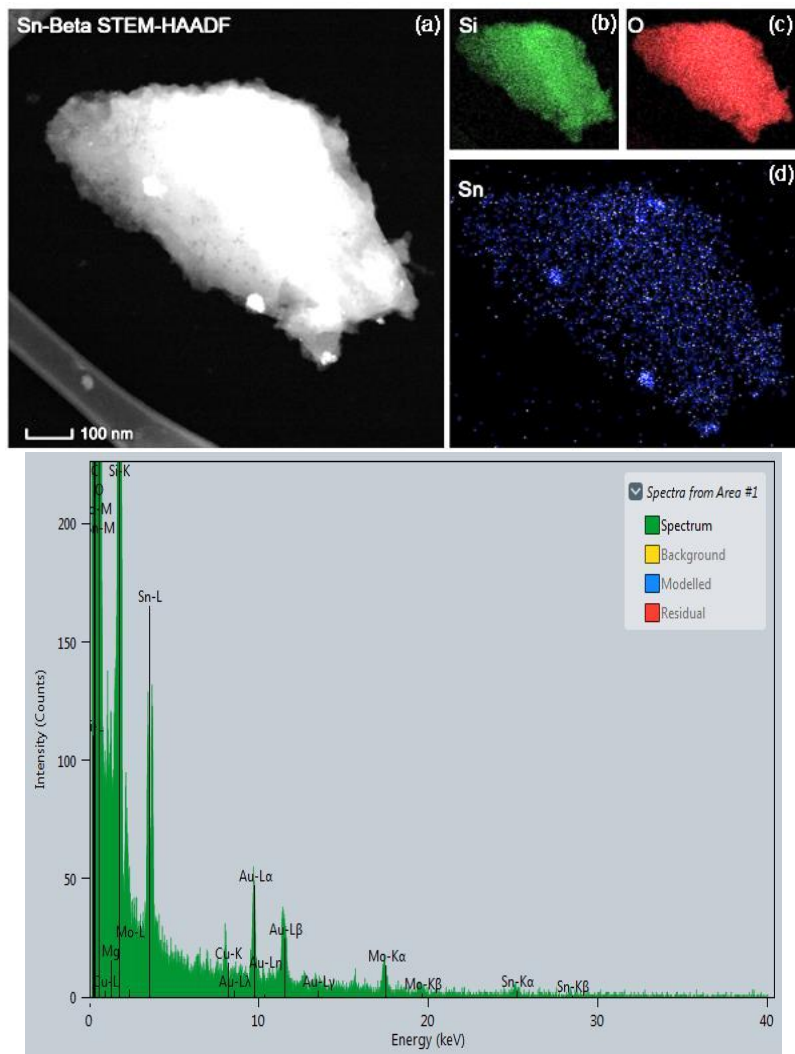
Fig.6.9: (a) STEM-HAADF of a fragment of a Sn-beta (HS) crystal. (b-d) *Kα* EDX maps for Si, O, and Sn respectively. Sn appears present in low levels throughout the crystal, and in higher concentrations in the fine particles which appear brightest in the HAADF. EDX spectrum of the whole scanned area in (a). Spectrum shows high levels of Si and O, as well as significant Sn peaks. Au, Mo, and Cu peaks likely originate from the sample grid, holder 'O' ring, and internal TEM components respectively.
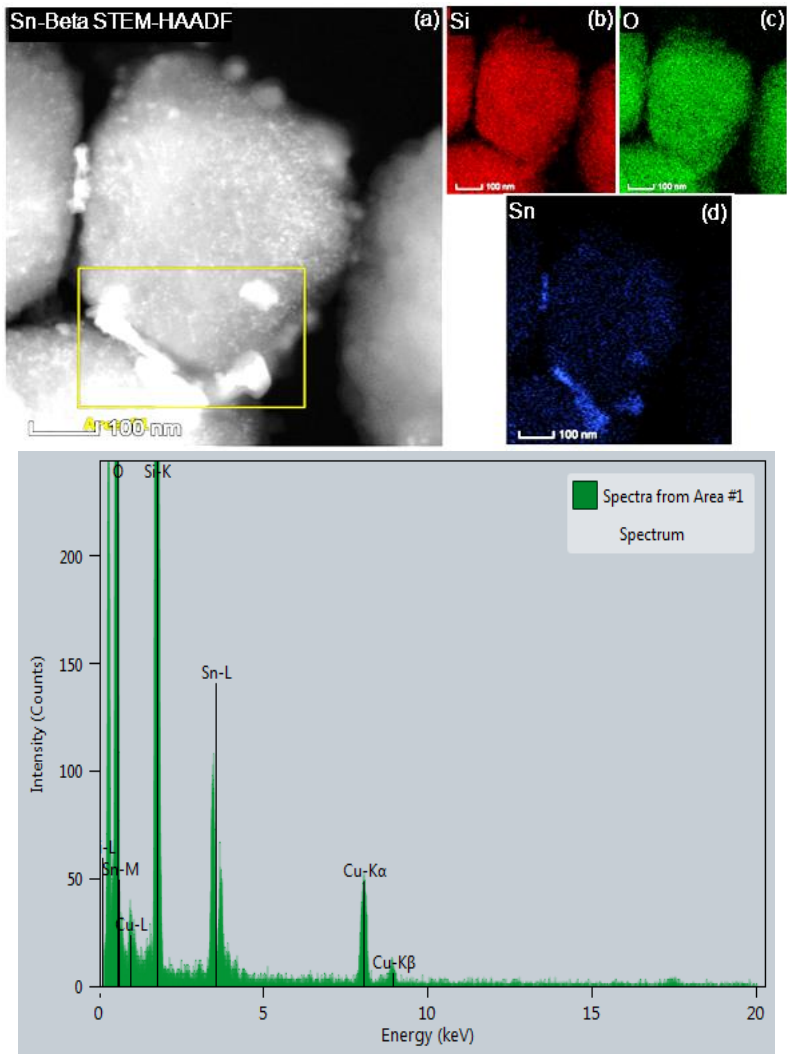
Fig.6.10: (a) STEM-HAADF micrograph of Sn-beta (SSIE) showing the area scanned to obtain the EDX spectrum in the spectrum below. (b – d) *Kα* EDX maps for Si, O, and Sn respectively. (e) EDX spectrum of the area highlighted by a yellow box in (a). Spectrum shows expected high levels of Si and O, as well as significant Sn peaks. A Cu grid was used in this instance, so there is no Au peak as in figure 6.9.

6.3 – High-resolution Scanning Transmission Electron Microscopy

6.3.1 – Bright-field STEM

Due to the large irradiation area and consequent broad damage of whole sections of crystal typical of CTEM techniques, STEM techniques were considered next. For a single high-resolution image in BF-TEM, a large region of a crystal would have to be sacrificed to produce an image with sufficient SNR, whereas with STEM, even if the local electron flux is higher, only the imaged region and a small area around it would be damaged. Therefore, STEM allows for more high-resolution observations per crystal. Figure 6.11 shows the effect of extended beam exposure in BF-TEM.
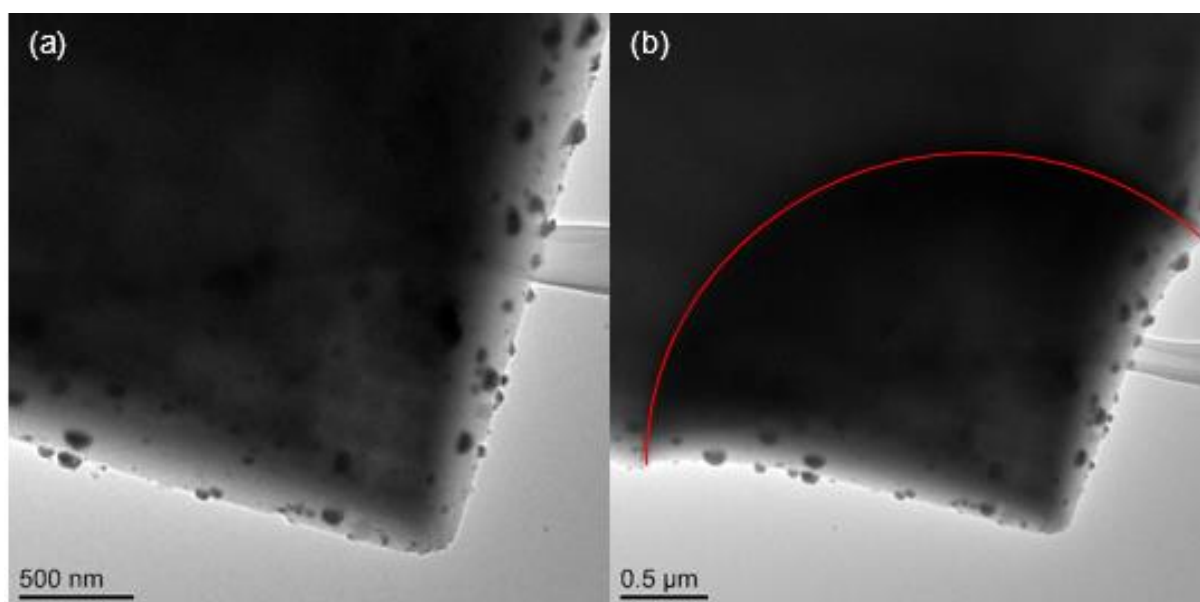
Fig.6.11: BF-TEM micrographs of a Sn-beta zeolite (HS), showing the contraction effect of prolonged beam exposure, wherein (a) displays a pristine crystal at initial exposure, and (b) shows the same crystal after an extended period of exposure with the beam focussed in the marked region. Micrographs acquired at 300 kV beam acceleration and ambient temperatures.

Figures 6.11 (a) and (b) were taken before and after extended beam exposure respectively. While (a) shows a pristine Sn-beta crystal with sharp surface facets, (b) shows a marked circular region which has contracted inward from the surface and

133

matches the region previously exposed to the electron beam during diffraction pattern acquisition for critical fluence determination. This suggests that as the crystal structure is damaged, the pore structure itself collapses inwards, causing contraction of the particle structure. This would affect attempts to acquire high-resolution images, due to shifting of the crystal structure during imaging. Hence, the use of the lowest possible beam flux that still allows for pore observation is necessary. With this in mind, the conditions ultimately used for BF-STEM imaging were 300 kV accelerating voltage, 20 µs dwell time, 5 pA beam current, 10 mrad probe convergence semi-angle (α). The convergence semi-angle gives a probe size of 1.4 Å. With a BF collection semi-angle (β) of 7 mrad at a camera length of 460 mm, conditions are met for good phase contrast collection efficiency for an uncorrected STEM, as per Sader *et al.* (2010). Ideally, β would be equal to half of α, but as β is tied to camera length, which has set values, a β of 7 mrad is as close as could be achieved.

Initial high-resolution BF-STEM experiments were performed with the aim of observing the pore structure of the zeolites without exceeding the critical fluence of the material, which was measured as ~17,000 ± 8,000 e$^-$Å^{-2}.

Figure 6.12 (a) shows a BF-STEM micrograph of a Sn-beta zeolite (HS) crystal at 900k times magnification and 235 e$^-$Å^{-2} total electron fluence. The crystal was initially oriented in either the [100] or [010] zone-axis by observing the diffraction pattern of the crystal at low magnification in TEM mode and using the double tilt capabilities of the sample holder to reorient until the correct on-axis diffraction pattern was observed. An example of this process is exemplified in figure 6.13. At low magnification and electron flux, this reorientation process typically exposes the sample to less than 10 e$^-$Å^{-2}.
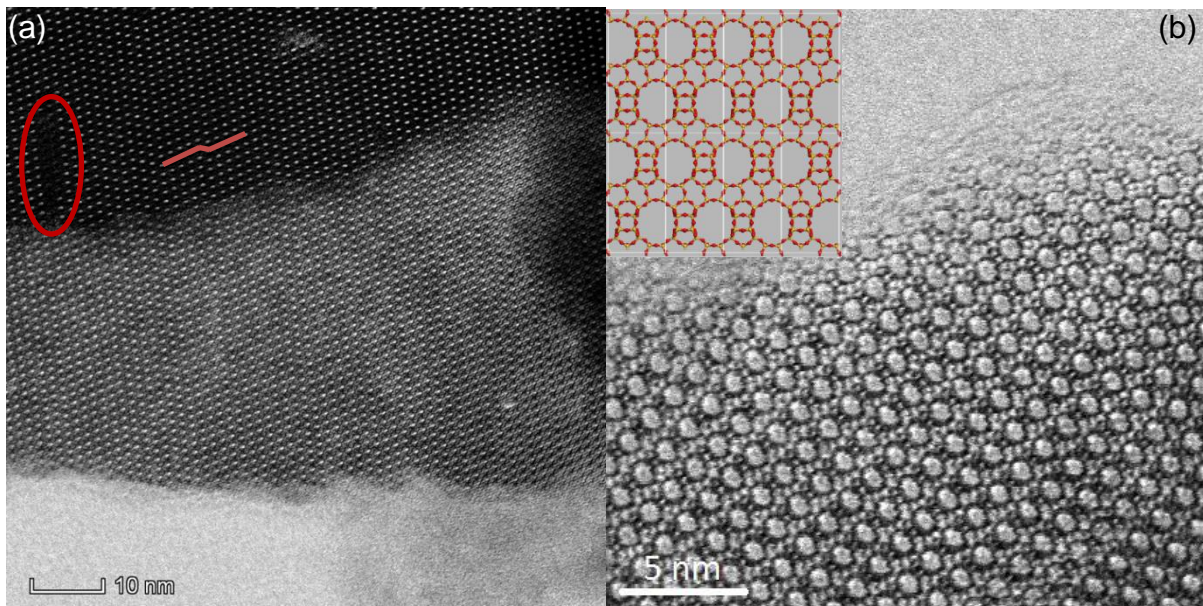
Fig.6.12: (a) BF-STEM micrograph of a Sn-beta zeolite (HS) crystal at 900k times magnification and 235 e⁻Å⁻² total fluence, showing several features of the crystal structure, including the pore structure, the effects of thickness (regions of differing contrast), and stacking faults, highlighted. (b) BF-STEM micrograph of a Sn-beta zeolite (HS) crystal at 2.7M times magnification and 1950 e⁻Å⁻² total fluence, showing the details of the zeolite pore structure and interconnecting molecular structure. The projected schematic structure of the [010] axis of Si-beta zeolite polymorph A is shown inset. Micrographs acquired at 300 kV accelerating voltage and ambient temperatures.

The micrographs in figure 6.12 were the earliest successful acquisitions of the pore structure of one of the zeolite samples. Though the resolution is not good enough at this magnification to make out the entire projected crystal structure, the pores are visible. Highlighted in figure 6.12 (a) is the effect of sample thickness on image quality, with the thicker regions showing darker contrast, and with less detail visible between the pores. The effects of crystal defects can be seen in this image and are highlighted by red lines and the circled area. The lines across the image show the effect of a stacking fault, causing misalignment of columns of pores throughout the structure. The circled area also shows the effect of a stacking fault as viewed down a perpendicular

axis, causing the pores to no longer overlap properly.
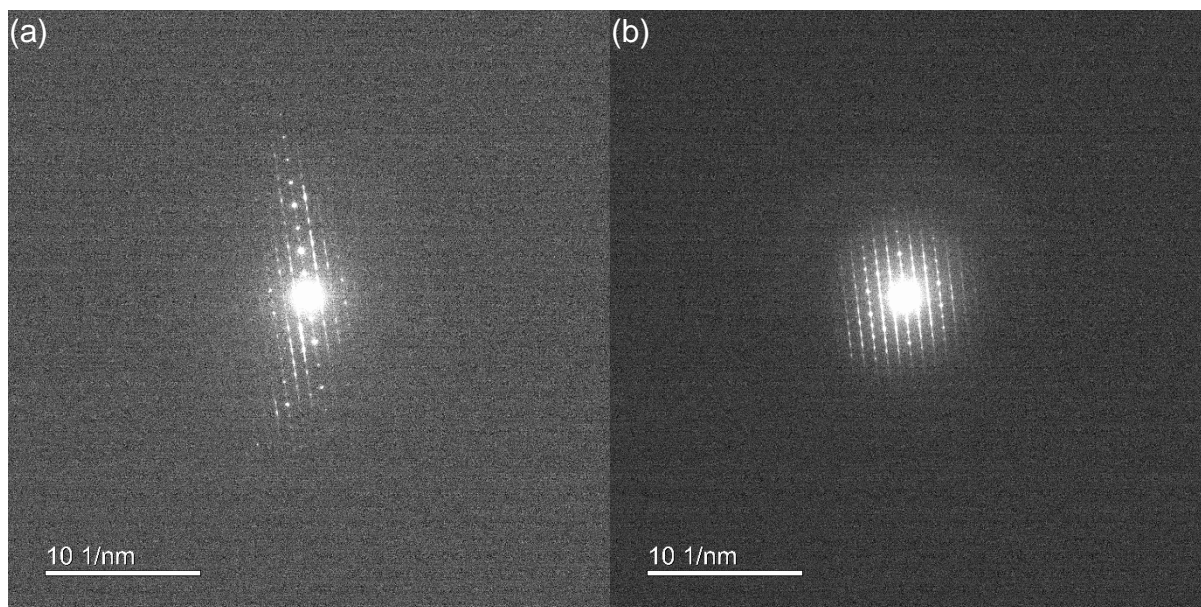
Fig.6.13: Diffraction patterns of Sn-beta zeolite (HS) (a) before and (b) after double tilt reorientation onto the [100]/[010] zone-axis. Acquired at 300 kV beam acceleration and ambient temperatures.

Figure 6.12 (b) shows a similar BF-STEM micrograph, but of a region observed at a higher magnification (2.7M times). The pore structure and interconnecting crystal structure is easily visible. Individual pores can be measured at about 0.8 nm across. This image again shows the effect of increasing sample thickness on the resolution. The atomic structure is most easily observed in the areas towards the very edge of the crystal. However, roughly 10 – 20 nm in from the edge the clarity of the features begins to drop. Despite the level of detail there is no way to distinguish between the Sn and Si atoms from images such as these, with individual atomic sites not clearly visible.

6.3.2 – Combined iDPC and HAADF-STEM

To overcome the limitations of BF-STEM, a combined imaging method was suggested. The iDPC imaging mode would be used to acquire high-resolution crystal structure

micrographs with improved phase contrast, giving clearer views of the projected atomic structure. Meanwhile, corresponding HAADF imaging would allow for improved contrast between the light and heavy elements, giving clearer views of potential Sn sites. HAADF alone can not be used, as the electron fluence required to obtain a HAADF image with sufficient SNR to observe the full projected crystal structure would greatly exceed the zeolite's critical fluence, hence the need for both low-fluence iDPC and HAADF.
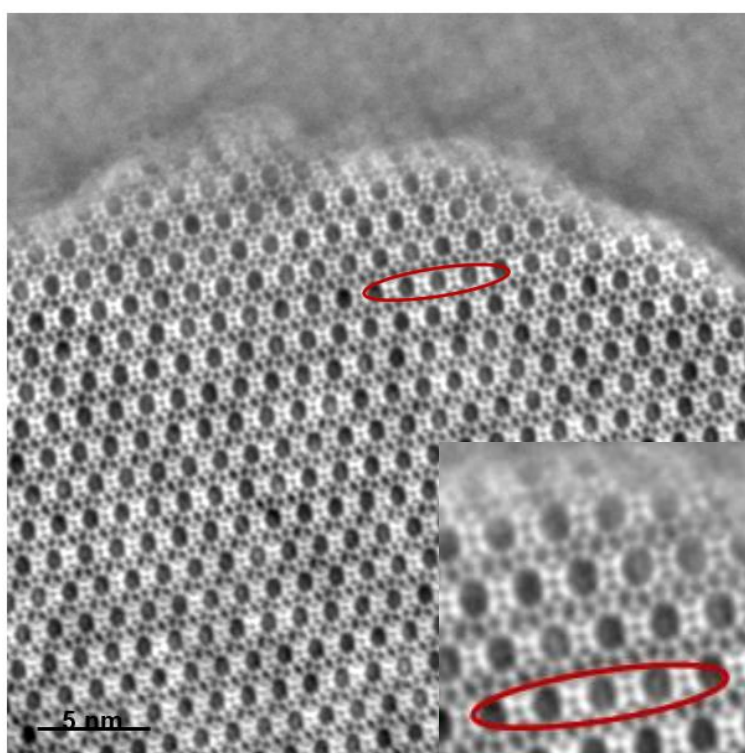
Fig.6.14: iDPC-STEM micrograph of a Si-beta zeolite crystal at 1.8M times magnification and 960 e⁻Å⁻² total fluence. Pore structure is very well resolved at the edge of the crystal and phase contrast has been improved, as indicated by the brighter contrast in the atomic columns highlighted. The region around the marked area is magnified to show the details of the atomic structure. Acquired at 300 kV beam acceleration and ambient temperatures.

Figures 6.14 and 6.16 show iDPC-STEM micrographs of Si-beta and Sn-beta (HS) respectively. Both micrographs show further improved resolution compared to the BF-STEM micrographs, with the crystal structure observable in high detail, particularly

towards the edge of the crystals where it is thinnest. Further in from the edge, the effect of crystal thickness is readily apparent as a blurring of structural detail.
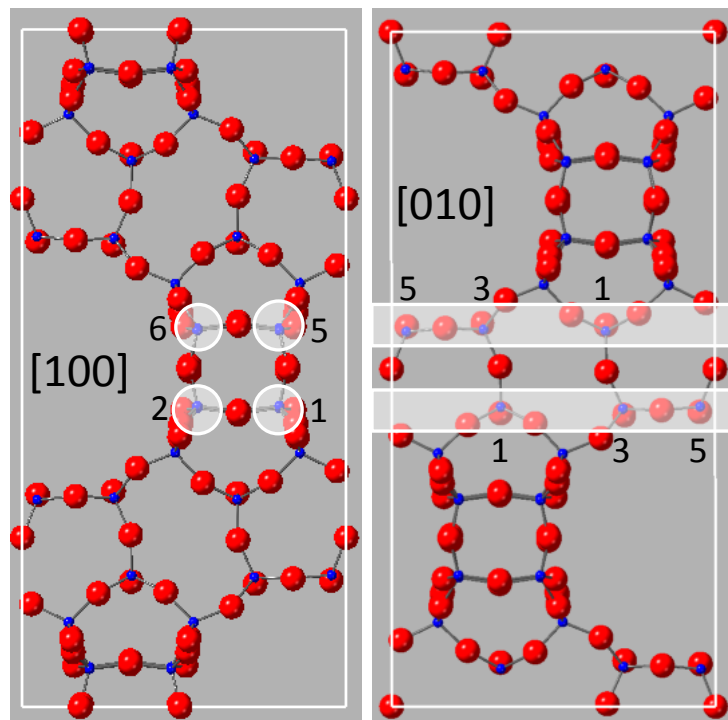
Fig 6.15: Schematics of the zeolite structure in the [100] and [010] directions. Red atoms are O, and blue atoms are Si. The highlighted regions show the most densely stacked regions as viewed in each direction. The highlighted regions in the [100] schematic will be referred to as the inter-pore columns. The dense stacking causes them to appear brighter than the surrounding atomic stacks in iDPC-STEM micrographs. The topmost T-sites in each of the columns in each orientation are labelled.

The phase contrast improvement obtained by iDPC imaging is also visible in these micrographs. The area highlighted by a red oval in figure 6.14 encompasses atomic columns which appear brighter compared to their neighbours. Based on the crystal structure of the zeolites, this is due to the increased atomic occupancy of these inter-pore columns, being about twice as dense as atomic columns outside this region. Figure 6.15 outlines this effect by showing the zeolite schematics in the [100] and [010] directions and highlights the regions of dense atomic stacking in the [100] orientation.

This region will be referred to as the inter-pore columns. T-sites 1-6 are encompassed in this area, with T-sites 7, 8, and 9 located in the sites between the areas highlighted in figure 6.15 (see figure 6.1).
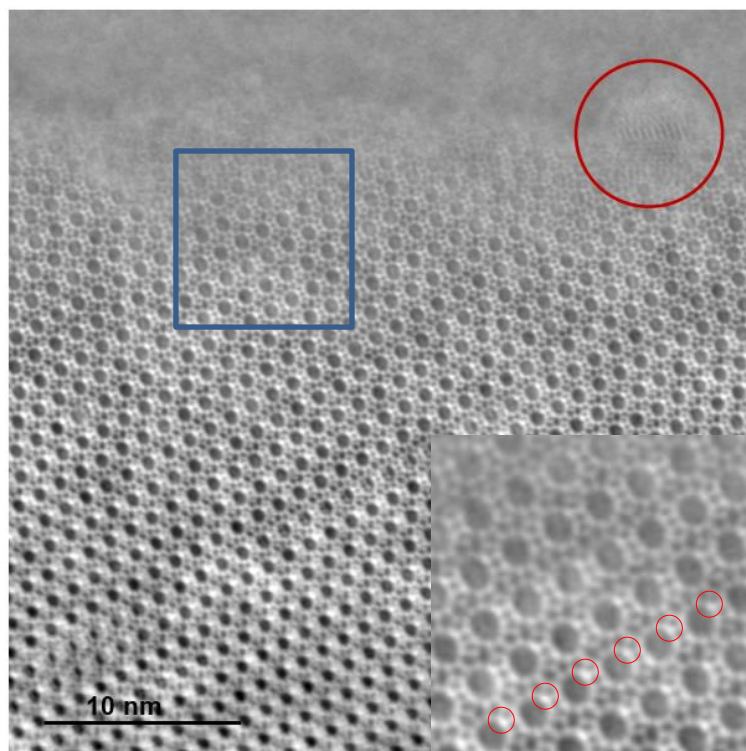
Fig.6.16: iDPC-STEM micrograph of a Sn-beta zeolite (HS) crystal at 1.35M times magnification and 430 e⁻Å⁻² total fluence. The pore structure is very well resolved at the crystal edge, and the phase contrast improved. Additionally, the area highlighted in the red circle shows the lattice of a SnO_2 nanoparticle on the surface of the zeolite crystal. The area highlighted with a blue square encompasses the area inset in the bottom right, magnified to show the projected atomic structure in more clarity. Acquired at 300 kV beam acceleration and ambient temperatures.

Contrast improvement is also seen in figure 6.16. However, within the inter-pore regions identified in figure 6.15 for the [100] zone-axis, a contrast imbalance is observed, with one of the four inter-pore columns appearing brighter than the others across a large section of figure 6.16. This may be down to the presence of Sn in these specific sites, though without knowledge of the orientation or vertical position of an

identified site, distinguishing between T-sites 1 to 6 is not possible. Sn occupancy in each of the highlighted sites seems unlikely given the 100:1 Si:Sn ratio used in the synthesis of these materials, and also the uniformity with which the brightest spot appears. However, Tolborg *et al.* (2014) noted an increase in Sn density around the edges of the crystals compared to the centres, which could account for this increased contrast if all of these sites are occupied by Sn.

Also visible in figure 6.16 is a lattice structure separate from that of the zeolite, highlighted by the red circle. Measuring these lattice spacings confirms this as a SnO_2 nanoparticle attached to the surface of the zeolite crystal, with a spacing measuring ~0.33 nm identified as the (110) spacing of SnO_2. Despite the high detail with which the crystal structure is visible in these micrographs, determination of the exact location of any Sn present in the Sn-beta sample is still impractical, hence the need for HAADF-STEM. Figure 6.17 emphasizes this point, with iDPC micrographs of both Si-beta and Sn-beta pores appearing near identical when compared in detail.
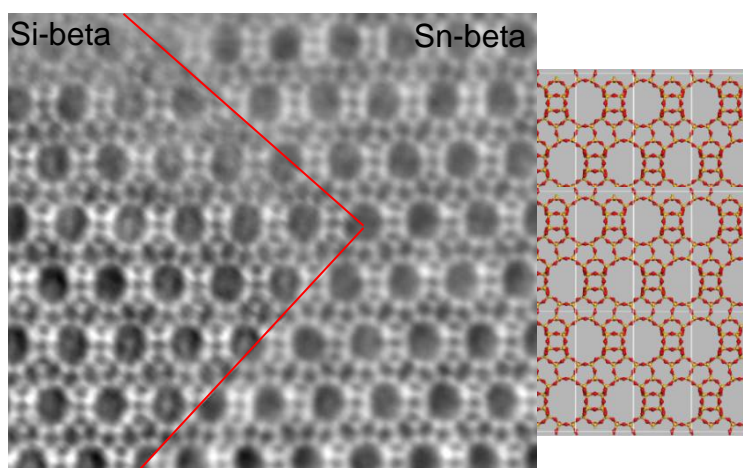
Fig.6.17: Composite image of cropped regions of Si-beta and Sn-beta (HS) observed down the [100]/[010] axis. The separation between the two is highlighted, and the schematic structure of Si-beta zeolite in the same orientation is also shown.
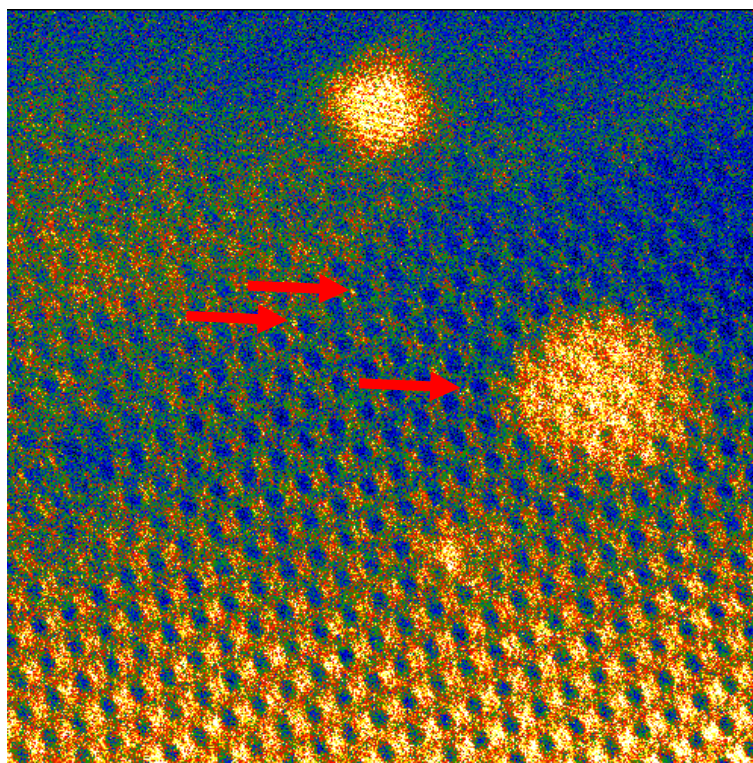
Fig.6.18: A false-coloured HAADF-STEM micrograph of a Sn-beta zeolite (HS) crystal taken at 1.8M times magnification and 960 $e^-Å^{-2}$ total fluence. Taken from the same area as the iDPC image in figure 6.16, with the SnO_2 nanoparticle at the surface being the same as the one highlighted in figure 6.16. Resolution is much lower than with iDPC, but contrast between elements greatly enhanced. Arrows highlight potential Sn sites, based on their relative brightness compared to the surrounding atomic columns. Acquired at 300 kV beam acceleration and ambient temperatures.

Figure 6.18 shows a HAADF-STEM micrograph of the same region of Sn-beta zeolite as imaged by iDPC in figure 6.16, and with false colour contrast applied. The critical fluence of Sn-beta is high enough that HAADF and iDPC micrographs can be acquired sequentially using a 5 pA probe current without significantly degrading the crystal. The level of detail is notably lower than the iDPC micrograph, as expected due to the exclusive collection of highly scattered (and therefore less intense) electrons in HAADF image formation, resulting in lower SNR. Despite this, the pore structure is visible. The SnO_2 nanoparticles are very clear in this image, owing to the improved

141

elemental contrast due to the higher atomic weight of Sn compared to Si. Also observed are certain columns of atoms in the zeolite structure that appear brighter than their neighbours, as highlighted by the red arrows. These localised bright spots are currently the prime candidate for Sn occupancy in Sn-beta zeolite.
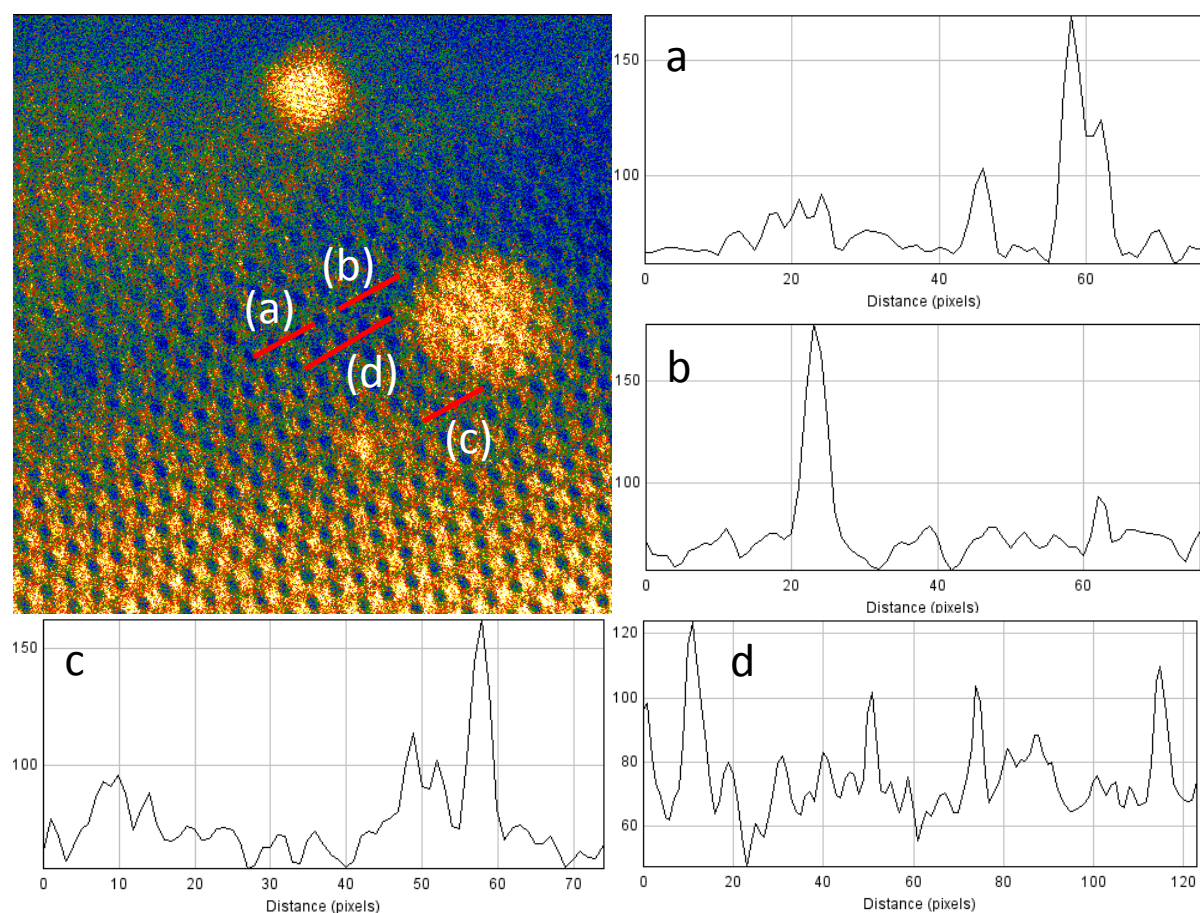
Fig.6.19: Intensity line profiles of Sn-beta where profiles (a) to (d) correspond to the lines (a) to (d) shown in the above false-coloured HAADF-STEM micrograph. Profiles (a) to (c) represent regions with a suspected Sn atom present, (d) without. Profiles produced with a line width of 5 pixels. The peak ratio between the column representing the suspected Sn occupancy and its nearest neighbour are 2.7 for (a), 5.6 for (b), and 1.8 for (c). The ratio between the highest peak and its nearest neighbour for (d) is 1.2.

In order to confirm that these bright spots are of significant intensity to indicate suspected Sn occupancy, intensity line profiles of these areas were obtained and compared to regions in the Sn-beta HAADF-STEM micrograph where these bright

spots do not appear, as well as compared to similar intensity line profiles from a Si-beta HAADF-STEM micrograph. Figure 6.19 shows the regions in Sn-beta from which four line profiles were taken, with regions (a) to (c) having suspected Sn occupancy, and region (d) having no such suspected occupancy.

Figures 6.19 (a-d) show the resulting intensity line profiles of these four regions. The peak ratios between the columns representing the suspected Sn occupancy and their nearest neighbours are 2.7 for (a), 5.6 for (b), and 1.8 for (c). The ratio between the highest peak and its nearest neighbour for (d) is 1.2. While the profile for (d) suggests that the noise levels are significant throughout this micrograph, the peak ratios for (a) to (c) are well above that level and suggest a significant increase in peak intensity at the selected points.
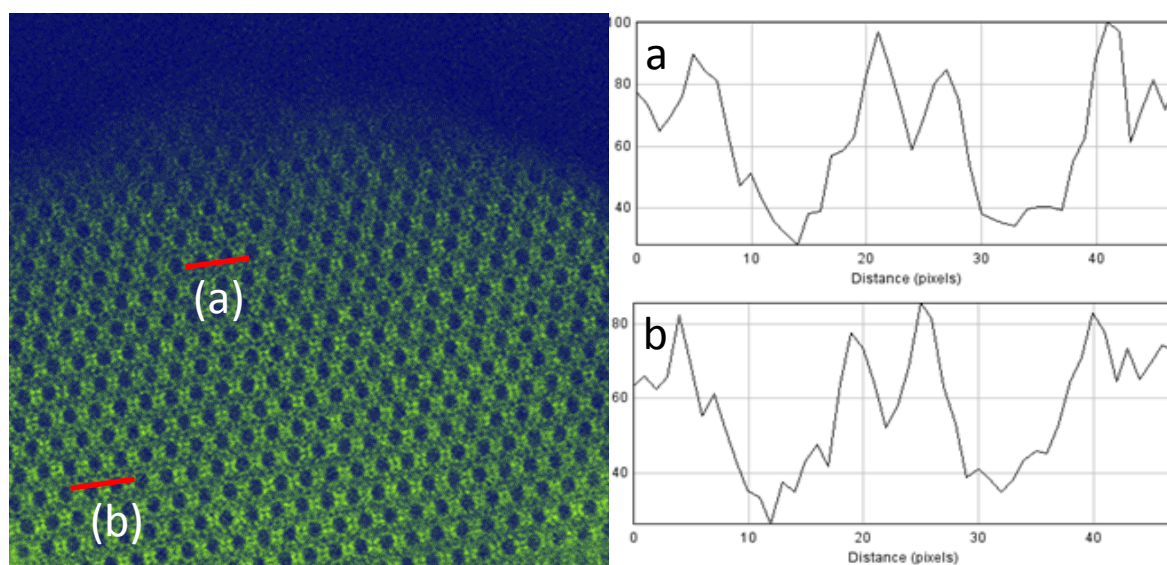
Fig.6.20: A false-coloured HAADF-STEM micrograph of Si-beta zeolite. Highlighted regions (a) and (b) correspond to the intensity line profiles opposite. Peak ratios between the central two peaks in each profile were 1.1 and 1.05 respectively.

Figure 6.20 shows a similar false-coloured HAADF-STEM micrograph as in 6.19, but this time taken from Si-beta. Two line profiles are also shown, corresponding to the marked regions in the HAADF-STEM micrograph. Unlike the Sn-beta micrographs, Si-

143

beta shows no obvious bright atomic stacks which might indicate the presence of Sn, so the line profiles were taken at locations where intensity differences in the stacks of atoms are more prominent to the naked eye. The result is two line profiles with intensity ratios between the most intense peaks in the profiled region being 1.1 and 1.05, both significantly lower than the values obtained from the line profiles of Sn-beta. This comparison supports the notion that the brighter atomic stacks in the Sn-beta HAADF-STEM micrographs are indicative of Sn occupancy.

From the high intensity peaks observed in line profiles across HAADF images of Sn-beta, and the lack of such peaks in HAADF images of Si-beta, identification of Sn atoms within the structure of the zeolite has potentially been achieved. However, because of the limited resolution achievable in HAADF due to the irradiation sensitivity of the sample, the exact atomic site occupied by the Sn atoms can not be accurately determined. Assuming Sn atoms are present in the atomic stacks in the bright spots observed in figure 6.18, Sn present in T-sites 1, 2, 3, 4, 5, and 6 would produce such images, with only T-sites 7, 8, and 9 effectively discounted, as they are the only sites which do not occupy the identified atomic column in either the [100] or [010] orientation. Nothing short of an accurate 3-dimensional positional measurement for the Sn atoms is capable of determining with 100% certainty the specific T-site occupancy of Sn in this Sn-beta zeolite from T-1 to T-6. Such a measurement is likely well out of the realm of possibility for STEM techniques, primarily as a result of the sensitivity of the material to the electron beam. To acquire a 3-dimensional location for the Sn by current STEM methods, two micrographs of the same area would have to be acquired; one down the [100] axis, and a second down the [010] axis. Given the morphology of the particles observed, finding a particle which is equally thin in both these directions is unlikely.

The potential Sn sites identified in figure 6.18 are in the same positions relative to the local structure, with each site being the top right position of the inter-pore columns highlighted in figure 6.15. If these positions are indeed occupied by Sn, this would suggest a uniformity with which the Sn is incorporated into the zeolite structure. Of concern is the fact that bright spots in figure 6.18 are not also seen in the alternative positions for the same T-sites. For example, if the bright spots seen represent T-1 occupancy by Sn, one might expect other bright spots to appear in any one of the other T-1 sites per unit cell, as shown in figure 6.1, though this is not the case. This may be due to the more limited HAADF contrast in these positions, or due to selective Sn occupancy resulting in Sn being incorporated into a particular position across a large area.

Sites such as those identified in figure 6.19 were identified in only two other locations, despite the great amount of time dedicated to finding them. This highlights the difficulty with which these sites are identified, based on the intricacies of achieving good quality iDPC and HAADF-STEM pairs before the onset of sample degradation.

6.4 – Computer simulated HAADF-STEM images

Though the results represented by the combined iDPC-STEM and HAADF-STEM micrographs are promising, the difficulty with which they are acquired and the limited number of sites available for the production of the line profiles limits their potential importance. As such, it was decided that computer simulated variations of the HAADF-STEM micrographs could be useful in supporting the experimentally obtained results. Simulations were carried out in collaboration with David Maldonado-Hernandez of the Complutense University of Madrid and were produced using the VESTA software package and multislice (Bloch-wave) methods. Simulations used the same convergence and collection angles as were used experimentally: 300 kV, 10 mrad semi-convergence angle, 1.4 nm probe size.
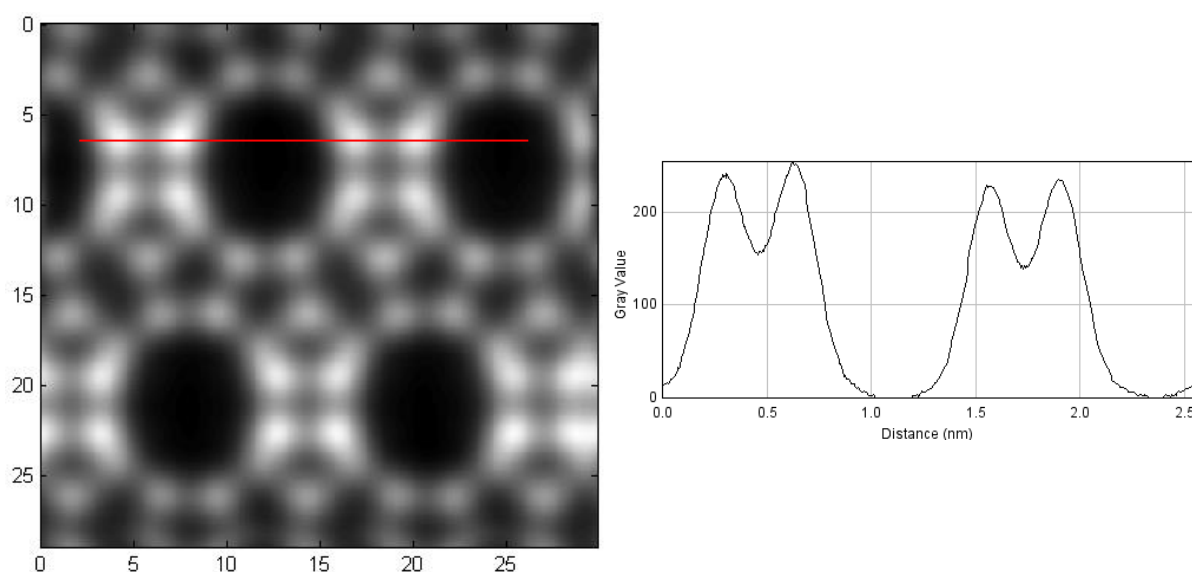
Fig.6.21: A simulated HAADF-STEM micrograph of Si-beta zeolite, observed down the [010] direction. The model has a thickness of 5 unit cells. Also shown is a line profile of the area highlighted in the simulated HAADF-STEM micrograph. Peak ratios are 1.1 and 1.05 respective to the left and right peak pairs.

Figure 6.21 shows a simulated HAADF-STEM micrograph of the Si-beta zeolite structure. The expected intensity differences between atomic sites are shown, with the

more densely occupied atomic columns separating the pores appearing brighter. The line profile also shown, produces limited intensity differences between these atomic columns with peak ratios between the central adjacent peaks of 1.1 and 1.05 respectively.
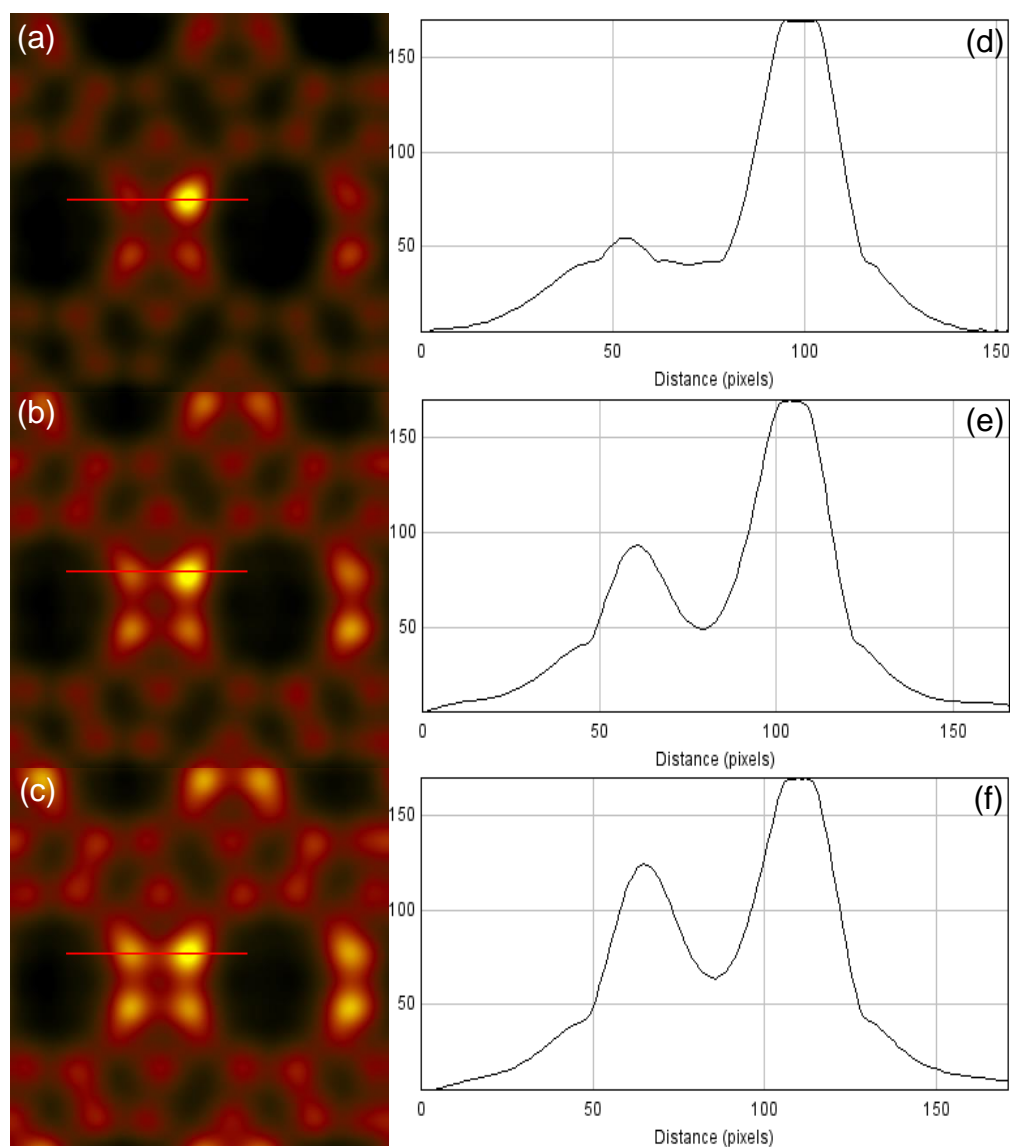
Fig.6.22: (a – c) Simulated false-colour HAADF-STEM micrographs of Sn-beta zeolite observed down the [010] direction. The Sn occupies the T3 site. The simulations are 2, 5, and 10 unit cells thick respectively. (d – f) Line profiles for each simulation of an area as highlighted in (a). Peak ratios are 3.1, 1.8, and 1.4 respectively.

Figure 6.22 shows three simulated false-colour HAADF-STEM micrographs of Sn-beta

zeolite (a – c) with line profiles across Sn occupied atomic columns (d – f). Each simulation represents an area of zeolite with a different thickness, those being 2, 5, and 10 unit cells thick respectively (2.5, 6.3, and 12.7 nm). In these cases, there is a single Sn atom in one of the T-3 sites about half way down the top right inter-pore atomic column. The T-3 site was chosen as it is relatively close to the centre of the atomic column. Each of the simulations shows increased brightness in the column with a Sn atom present. The relative level of brightening decreases with increasing thickness of the simulated area, with peak ratios between the Sn occupied atomic column and its neighbour from the line profiles measuring 3.1, 1.8, and 1.4 for (d), (e), and (f) respectively.

Another set of simulations was produced to investigate the effects of Sn atom position within a given atomic stack, the results of which are shown in figure 6.23. It was theorised that, depending on the depth of the Sn atom, electron beam channelling could occur, resulting in intensity variation in the resultant HAADF. Four such simulations were run, with 2 unit cell thick sample areas (2.5 nm). In each, one Sn atom was positioned within the same atomic stack as in figure 6.22, but in different sites within that stack to alter the depth of the Sn atom. A T-3 site was occupied for positioning the Sn atom at the top and bottom surfaces, and a T-1 site was occupied for positioning the Sn atom ¼ and ¾ of the way down the atomic column. Each resultant simulated HAADF closely resembled figure 6.22(a) and, when measured, peak ratios for each were 3 ± 0.1. This suggests that the effects of channelling are not significant enough to cause a perceptible change in intensity for atomic stacks with Sn present.
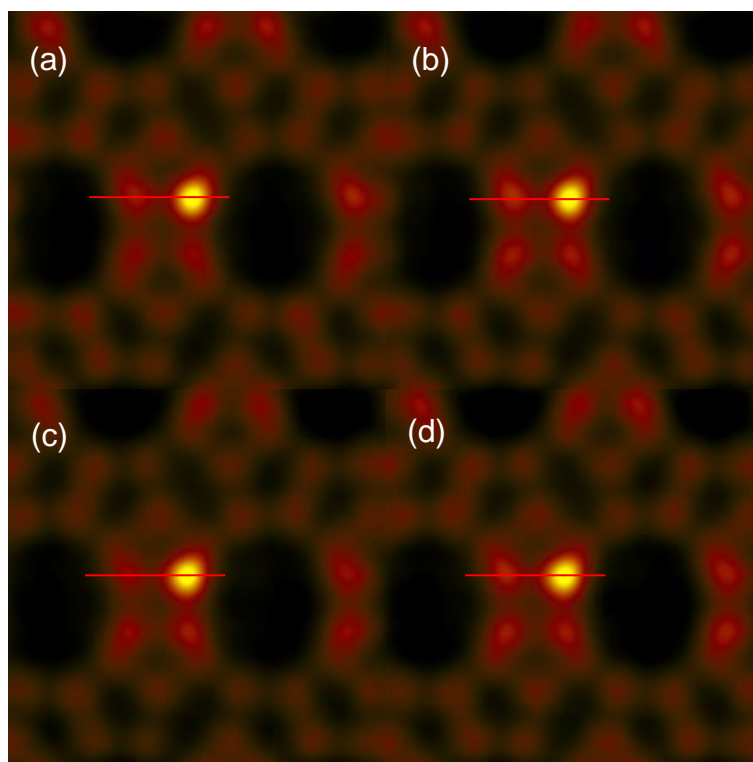
Fig.6.23: Simulated false-colour HAADF-STEM micrographs of Sn-beta zeolite observed down the [010] direction. These simulations are 2 unit cells thick. In (a) Sn occupies the T-3 at the top of the atomic stack. In (b) Sn occupies a T-1 site roughly ¼ of the way down the atomic stack. The Sn also occupies a T-1 site in (c) though ¾ of the way down the atomic stack in this case. In (d) Sn occupies the T-3 site at the bottom of the atomic stack. Line profiles for each (not shown) were measured from the highlighted areas and the peak ratios measured.

6.4 – Discussion

The iDPC and HAADF results suggest Sn occupancy in one or multiple T-sites from 1 – 6. T-sites 7, 8, and 9 fall outside of the identified inter-pore region containing suspected Sn occupancy. There is some disagreement between the iDPC and HAADF results however, with the iDPC micrographs showing potential Sn occupancy in similar sites across large areas of a sample (figure 6.16), while HAADF results show only a handful of sites of potential Sn occupancy within a given area (figure 6.18). Tolborg *et al.* (2014) noted a higher density of Sn towards the edges of crystals of this material, which could explain the iDPC results, though a great number of repeated experiments would be needed to confirm this.

In comparison to previous studies aimed at determining the T-site occupancy of Sn in beta zeolite, this work does not narrow down the range of T-sites as much as any one of the papers mentioned in section 6.1. However, in contrast to most of the cited research in section 6.1, this work is based primarily on experimental research as opposed to computational simulation. Additionally, the results of this work can be used as support or refutation of other literature. For example, the studies by Shetty *et al.* (2005) and Yang *et al.* (2013) both found the T-2 site to be preferably occupied, which this work would support. Similarly, for the study by Bare *et al.* (2005), which found the T-1 and T-2 sites preferable, this work supports these findings. The works of Josephson *et al.* (2017) and Kolyagin *et al.* (2019) are only partially supported by this work, as they identified T-1 and T-9, and T-sites 5, 6, and 7 respectively, where our work has discounted T-sites 7, 8, and 9.

6.5 – Summary

The key findings from this study are as follows. Firstly, a critical fluence was determined for Sn-beta zeolite in order to inform our decisions regarding high-resolution imaging. This was measured as 17,000 ± 8,000 $e^-Å^{-2}$. By the use of EDX spectroscopy, Sn was confirmed to be present within the Sn-beta zeolite samples, but absent in the Si-beta zeolite sample, as expected. Sn signals showed the presence of Sn throughout the samples, as well as in smaller high density clusters or nanoparticles of Sn_xO_y. BF-STEM was determined as a preferable technique for characterisation of these materials compared to BF-TEM owing to the more localised imaging areas used for BF-STEM, preventing damage to large areas of a crystal. iDPC-STEM provides improved phase contrast and resolution over BF-STEM, sufficient enough to show all projected atomic positions of the zeolites in the [100]/[010] orientations. It is not sensitive enough to easily reveal the locations of Sn atoms however. The use of HAADF-STEM in conjunction with iDPC-STEM highlights SnO2 contamination and potential Sn atomic sites within the Sn-beta zeolite structures, though repeated acquisition of such results proved challenging. Simulations of the HAADF micrographs produce intensity profiles similar to the experimentally acquired HAADF micrographs with Sn atoms in the T-1 and T-3 positions. Due to the identical nature of the [100] and [010] axes however, without observation of a Sn site in both of these orientations, accurate identification of the inhabited atomic site is impossible. With only information from one orientation, the Sn sites identified in figure 6.18 could be T-sites 1, 2, 3, 4, 5, or 6.

Chapter 7 – Summary and Concluding Remarks

This work has demonstrated the potential application of low-dose electron microscopy (EM) to the structural characterisation of organic compounds and beam-sensitive inorganics. These non-conducting materials suffer from radiolytic alteration on irradiation with high-energy electrons. Techniques and workflow strategies to mitigate this have been investigated and demonstrated. These include: lowering the irradiation intensity; increasing the kV (if the specimen is relatively thick); cooling the specimen; using a conducting support film. Of all the microscope techniques utilised in this study, bright-field (BF) scanning transmission electron microscopy (STEM) holds the most promise for direct imaging of the atomic lattice. This is because of the efficient use of dose budget made possible by Ronchigram focussing and the ability to lower dose via the use of scanning moiré fringes (SMFs). Additionally, the collection of all electrons in the zero-order disc has yet to be optimised.

7.1 – Critical Fluence of Theophylline Form II

A combination of energy dispersive X-ray spectroscopy (EDX) and scanning electron microscopy (SEM) was used to confirm the production of theophylline form II in its desired morphology by recrystallisation of theophylline from a nitromethane solution. DP analysis was used to determine the critical fluence (C_F) of theophylline form II under a number of controlled sample and microscope conditions. Under standard conditions (200 kV accelerating voltage, room temperature, continuous carbon support film) a C_F of 26 ± 5 e$^-$Å^{-2} was measured. Specimen stability was improved by increasing the accelerating voltage to 300 kV and using a graphene support film. Cooling the sample to liquid nitrogen temperature did not result in a significant

improvement in C_F, however the combination of cooling and the use of a graphene support film gave the highest C_F of 42 ± 5 e$^-$Å^{-2}.

Follow up work on measuring the C_F of a number of different beam sensitive pharmaceutical compounds has been performed by S'ari *et al.* (2015). These were found to be even more beam-sensitive than theophylline. This work was extended by S'ari *et al.* (2018), reporting a predictive method of determining C_F of pharmaceutical materials based on their molecular structures. A group of three descriptors were found to predict most accurately the C_F of each molecule, these being the ratio of conjugated carbons to non-conjugated carbons, the ratio of hydrogen bond donors to acceptors, and the ratio of hydrogen bond acceptors to donors.

7.2 – Scanning Moiré Fringes of Theophylline Form II

Atomic lattice information for theophylline form II by both direct and indirect observation in conventional transmission electron microscopy (CTEM) and STEM were obtained. The (002) spacings of theophylline form II were identified in the fast Fourier transform (FFT) of a BF-TEM micrograph obtained using a direct electron detection (DED) camera (Gatan K2). (011) spacings were just resolvable by FFT using low-dose BF-STEM techniques. Indirect observation was achieved by developing a methodology for repeated SMF acquisition and analysis. Defects in the SMFs of theophylline form II were observed. This work was published and extended to two other pharmaceutical materials in S'ari *et al.* (2019). Multiple defects were imaged in these additional materials. Each of these results came only after a great amount of time and effort. As high-end technology like the DED cameras (including pixelated STEM detectors) become increasingly available, such effort should be minimised.

7.3 – BF-STEM and iDPC of Sn-Beta Zeolite

A C_F was determined for Sn-beta zeolite of 17,000 ± 8,000 $e^-Å^{-2}$. By EDX spectroscopy, Sn was confirmed to be present within the Sn-beta zeolite samples, but absent in the Si-beta zeolite sample, as expected. Integrated differential phase contrast (iDPC) STEM was used to produce high-resolution micrographs of the zeolites, revealing projected atomic positions in the [100]/[010] orientations. The use of high-angle annular dark-field (HAADF) STEM in conjunction with iDPC-STEM highlighted excess Sn in the form of SnO_2 and identified potential individual Sn atomic sites within the Sn-beta zeolite structures. Simulations of the HAADF micrographs produced intensity profiles similar to the experimentally acquired HAADF micrographs with Sn atoms positioned in the T1 and T3 Si sites. Due to the identical nature of the [100] and [010] axes, accurate identification of the inhabited atomic site by these techniques alone is not possible. With only information from one orientation, the Sn sites identified could be any of T-sites 1, 2, 3, 4, 5, or 6.

Improvements to TEM characterisation of zeolites and similarly beam sensitive inorganics are ongoing, and a recent paper by Zhang *et al.* (2018) highlighted their efforts to automate the process of specimen tilting onto a zone-axis. By doing so, less time, and therefore dose budget, is spent manually tilting the specimen. Such dose-saving methods then allow for extended atomic resolution characterisation.

7.4 – Future Outlook

Based on the outputs of this work, methods and workflows for TEM characterisation of similarly beam sensitive materials are suggested. Firstly, measure the C_F of the material under investigation by TEM electron diffraction (ED), as this will define the

dose budget for that specimen and allows for appropriate planning of further EM experiments. If improvements are required, lower the electron beam flux as much as possible, use 300 kV accelerating voltage where available (particularly if the sample is ≥50 – 100 nm thick), cool the sample to liquid nitrogen temperatures, and use a conductive specimen substrate. If a DED is available for use in place of a complementary metal-oxide-semiconductor (CMOS) camera, take advantage of it, although CMOS cameras are more than useable. A recent review of 3D ED techniques (Gemmi *et al.*, 2019) has shown the improvements made in recent years owing to several technological and technique advances (faster, more sensitive cameras, beam precession, and specimen tilt and rotation automation. The crystal structures of beam-sensitive pharmaceutical materials are therefore now resolvable by this technique (van Genderen *et al.*, 2016).

BF-STEM techniques show most promise for analysis of these materials, owing to much more limited areas of specimen damage afforded by on-specimen Ronchigram focussing, phase contrast improvement techniques (such as SMFs), and the potential for improvement in electron collection efficiency with pixelated STEM detectors (*e.g.* MacLaren *et al.*, 2016, and Sagawa *et al.*, 2018). Ongoing developments here mean that BF-STEM could outstrip BF-TEM in terms of the amount of data that can be collected within the available dose budget of a specimen.

As shown by studies such as those of S'ari *et al.*, 2019, and Zhang *et al.*, 2018, improvements in the understanding, techniques, and equipment associated with TEM of beam-sensitive materials are quickly accelerating, and there is potential for TEM to become an indispensable tool for industrial scale characterisation of a wide range of such materials.

7.5 – Final Summary

The work done to determine the critical fluence of theophylline form II under a number of different beam and sample conditions (Chapter 4) has brought together the findings of multiple prior works into a single experimental investigation, in order to determine optimum conditions for EM characterisation of a model beam-sensitive organic material. A suggested workflow for characterisation of similar materials is proposed, which has already proven successful for characterisation of samples even more beam sensitive that theophylline.

The work on high resolution characterisation of theophylline (Chapter 5) has extended the work described in the literature by succeeding in the lattice imaging of theophylline by means other than Cryo-EM, and by incorporating moiré fringe acquisition as a qualitative characterisation technique. A workflow for consistent acquisition of these fringes is proposed, which has also seen further success with other materials.

The work done to characterise the Sn content of Sn-beta zeolite has provided an experimental contrast to the predominantly computer simulation based prior literature, and supports certain conclusions drawn by said prior literature. A workflow for joint iDPC and HAADF imaging of this material is produced which may prove useful for future elemental characterisation of similarly beam-sensitive materials.

References

Abellán, P, Woehl, TJ, Parent, LR, Browning, ND, Evans, JE, Arslan, I, *Chemical Communications*, **50**, 'Factors Influencing Quantitative Liquid (Scanning) Transmission Electron Microscopy', 2014, 4873-4880

Aitipamula, S, Chow, PS, Tan, RBH, *CrystEngComm*, **16**, 'Polymorphism in Cocrystals and their Physiochemical Properties', 2009, 3451-3465

Armache, JP, Jarasch, A, Anger, AM, Villa, E, Becker, T, Bhushan, S, Jossinet, F, Habeck, M, Dindar, G, Franckenberg, S, Marquez, V, Mielke, T, Thomm, M, Berninghausen, O, Beatrix, B, Söding, J, Westhof, E, Wilson, DN, Beckmann, R, *Proceedings of the National Academy of Sciences*, **107**, 'Cryo-EM Structure and rRNA Model of a Translating Eukaryotic 80S Ribosome at 5.5-Å Resolution', 2010, 19748-19753

Arora, KK, Thakral, S, Suryanarayanan, R, *Pharmaceutical Research*, **30**, 'Instability in Theophylline and Carbamazepine Tablets: Cocrystal Formation due to Release of Lattice Water', 2013, 1779-1789

Auerbach, SM, Carrado, KA, Dutta, PK eds., 'Handbook of Zeolite Science and Technology', 2003, Marcel Dekker, Inc. (New York)

Bare, SR, Kelly, SD, Sinkler, W, Low, JJ, Modica, FS, Valencia, S, Corma, A, Nemeth, LT, *Journal of the American Chemical Society*, **127** (37), Uniform Catalytic Site in Sn-β-Zeolite Determined Using X-ray Absorption Fine Structure', 2005, 12924-12932

Barnes, PJ, *Thorax*, **61**, 'Theophylline for COPD', 2006, 742-743

Batson, PE, Dellby, N, Krivanek, OL, *Nature*, **418**, 'Sub-ångstrom resolution using aberration corrected electron optics', 2002, 617-620

Bell, DC, Erdman, N, *Wiley-Royal Microscopical Society Series*, 'Low voltage electron microscopy: principles and applications', ISBN: 978-1-118-49848-4, 2012

Bennett, DW, 'Understanding Single Crystal X-Ray Crystallography', 2010, Wiley-VCH (Weinheim)

Betzig, E, Patterson, GH, Sougrat, R, Lindwasser, OW, Olenych, S, Bonifacino, JS, Davidson, MW, Lippincott-Schwartz, J, Hess, HF, *Science*, **313**, 'Imaging

Intracellular Fluorescent Proteins at Nanometer Resolution', 2006, 1642-1645

Bhatia, S, 'Zeolite catalysts: principles and applications', 1989, CRC Press (Boca Raton)

Brydson, R 'Aberration-Corrected Analytical Transmission Electron Microscopy', 2011, Wiley

Brydson, R, 'Electron Energy Loss Spectroscopy', 2001, BIOS Scientific (Oxford)

Brydson, R, Eddleston, MD, Jones, W, Seabourne, CR, Hondow, N, *Journal of Physics: Conference Series*, **522**, 'EELS from Organic Crystalline Materials', 2014, 012060

Buban, JP, Ramasse, Q, Gipson, B, Browning, ND, Stahlberg, H, *Journal of Electron Microscopy*, **59**, 'High-Resolution Low-Dose Scanning Transmission Electron Microscopy', 2010, 103-112

Bučar, DK, Lancaster, RW, Berstein, J, *Angewandte Chemie International Edition*, **54**, 'Disappearing Polymorphs Revisited', 6972-6993, (2015)

Bursill, LA, Lodge, EA, Thomas, JM, *Nature*, **286**, 'Zeolitic structures as revealed by high-resolution electron microscopy', 1980, 111-113

Chai, Y, Xie, L, Yu, Z, Dai, W, Wu, G, Guan, N, Li, L, *Microporous and Mesoporous Materials*, **264**, 'Lead-containing Beta zeolites as versatile Lewis acid catalysts for the aminolysis of epoxides', 2018, 230-239

Chang, J, Weigele, P, King, J, Chiu, W, Jiang, W, *Structure*, **14**, 'Cryo-EM Asymmetric Reconstruction of Bacteriophage P22 Reveals Organization of its DNA Packaging and Infecting Machinery', 2006, 1073-1082

Chen, CJ, 'Introduction to Scanning Tunnelling Microscopy', 2008, Oxford University Press (Oxford)

Chung, FH, Smith, DK, 'Industrial Applications of X-Ray Diffraction', 2000, Marcel Dekker, Inc. (New York)

Clark, WRK, Chapman, JN, MacLeod, AM, Ferrier, RP, *Ultramicroscopy*, **5** (1-3), 'Radiation damage mechanisms in copper phthalocyanine and its chlorinated derivatives', 1980, 195-208

Corma, A, Domine, ME, Nemeth, L, Valencia, S, *Journal of the American Chemical*

Society, **124**, 'Al-free Sn-beta zeolite as a catalyst for the selective reduction of carbonyl compounds (Meerwein-Ponndorf-Verley reaction)', 2001, 3194-3195

Craven, RJ, Lenki, RW, *Food & Function*, **3**, 'Symmetry, Chirality and Crystalline Tendency: The Polymorphism of Triacylglycerols', 2012 228-233

Cronstedt, AF, *Svenska Vetenskaps Akademiens Handlingar Stockholm*, **17**, 'Natural zeolite and minerals', 1756, 120

Dekkers, NH, de Lang, H, *OPTIK*, 'Differential Phase Contrast in STEM', 1974, 452-456

Eaton, P, West, P, 'Atomic Force Microscopy', 2010, Oxford University Press (Oxford)

Eddleston, MD, 'Crystal Form and Defect Analysis of Pharmaceutical Materials', PhD Thesis, 2011, University of Cambridge

Eddleston, MD, Bithell, EG, Jones, W, *Journal of Pharmaceutical Sciences*, **99** (9), 'Transmission Electron Microscopy of Pharmaceutical Materials', 2010, 4072-4083

Eddleston, MD, Hejczyk, KE, Bithell, EG, Day, GM, Jones, W, *Chemistry – A European Journal*, **19**, 'Determination of the Crystal Structure of a New Polymorph of Theophylline', 2013, 7883-7888

Eddleston, MD, Hejczyk, KE, Cassidy, AMC, Thompson, HPG, Day, GM, Jones, W, *Crystal Growth & Design*, **15**, 'Highly Unusual Triangular Crystals of Theophylline: The Influence of Solvent on the Growth Rates of Polar Crystal Faces', 2015, 2514-2523

Egerton, RF, 'Physical Principles of Electron Microscopy', 3rd edition, 2008, Springer Science+Business Media, LLC (New York)

Egerton, RF, Konstantinova, T, Zhu, Y, 'Analysis of Beam-Sensitive Materials by Electrons and X-Rays', In: Advances in Imaging and Electron Physics, eds. Berz, M, Duxbury, PM, Ruan, CY, 2015, Elsevier (San Diego)

Egerton, RF, Li, P, Malac, M, *Micron*, **35** (6), 'Radiation damage in the TEM and SEM', 2004, 399-409

Egerton, RF, *Microscopy*, **67** (1), 'Calculation, consequences and measurement of the point spread function for low-loss inelastic scattering', 2018, 52-59

Egerton, RF, *Ultramicroscopy*, **127**, 'Control of Radiation Damage in the TEM', 2013,

100-108

Egerton, RF, *Ultramicroscopy*, **145**, 'Choice of operating voltage for a transmission electron microscope', 2014, 85-93

Evans, JE, Hetherington, C, Kirkland, A, Chang, LY, Stahlberg, H, Browning, N, *Ultramicroscopy*, **108**, 'Low-dose aberration corrected cryo-electron microscopy of organic specimens', 2008, 1636-1644

Feigin, LA, Svergun, DI, 'Structure Analysis by Small-Angle X-Ray and Neutron Scattering', 1987, Springer (New York)

Forrest, SR, Thompson, ME, *Chemical Reviews*, **107**, 'Introduction: Organic Electronics and Optoelectronics', 2007, 923-925

Freeman, HM, Scott, AJ, Brydson, RMD, *Carbon*, **115**, 'Thermal annealing of nuclear graphite during in-situ electron irradiation', 2017, 659-664

Fucke, K, McIntyre, GJ, Wilkinson, C, Henry, M, Howard, JAK, Steed, JW, *Crystal Growth & Design*, **12**, 'New Insights into an Old Molecule: Interaction Energies of Theophylline Crystal Forms', 2012, 1395-1401

Garratt-Red, AJ, Bell, DC, 'Energy Dispersive X-Ray Analysis in the Electron Microscope, 2005, BIOS Scientific (Oxford)

Gemmi, M, Mugnaioli, E, Gorelik, TE, Kolb, U, Palatinus, L, Boullay, P, Hovmöller, S, Abrahams, JP, *ACS Central Science*, **5**, '3D Electron Diffraction: The Nanocrystalline Revolution', 2019, 1315-1329

Glaeser, RM and Taylor, KA, *Journal of Microscopy*, **112** (1), 'Radiation damage relative to transmission electron microscopy of biological specimens at low temperature: a review', 1978, 127-138

Goodhew, PJ, Humphreys, J, Beanland, R, 'Electron Microscopy and Analysis', 3rd edition, 2000, CRC Press (Boca Raton)

Grubb, DT, *Journal of Materials Science*, **9**, 'Review – Radiation Damage and Electron Microscopy of Organic Polymer', 1974, 1715-1736

Hammond, C, Conrad, S, Hermans, I, *Angewandte Chemie International Edition*, **51**, 'Simple and scalable preparation of highly active Lewis acidic Sn-β', 2012, 11736-11739

Han, Z, Fina, A, *Progress in Polymer Science*, **36**, 'Thermal Conductivity, of Carbon Nanotubes and their Polymer Nanocomposites: A Review', 2011, 914-944

Hao, X, Kuang, C, Gu, Z, Wang, Y, Li, S, Ku, Y, Li, Y, Ge, J, Liu, X, *Light: Science & Applications*, **2**, 'From Microscopy to Nanoscopy via Visible Light', 2013

Hardy, M, Doherty, MD, Krstev, I, Maier, K, Möller, T, Müller, G, Dawson, P, *Analytical Chemistry*, **86**, 'Detection of Low-Concentration Contaminants in Solution by Exploiting Chemical Derivitization in Surface-Enhanced Raman Spectroscopy', 2014, 9006-9012

Haruta, M, Kurata, H, *Scientific Reports*, **2**, 'Direct Observation of Crystal Defects in an Organic Molecular Crystals of Hexachlorophthalocyanine by STEM-EELS', 2012, 252

Hasa, D, Carlino, E, Jones, W, *Crystal Growth & Design*, **16**, 'Polymer-Assisted Grinding, a Versatile Method for Polymorph Control of Cocrystalization', 2016, 1772-1779

Herman, B, Lemasters, JJ eds., 'Optical Microscopy – Emerging Methods and Applications', 1993, Academic Press, Inc. (San Diego)

Hobbs, LW, 'Radiation Effects in Analysis by TEM', In: Introduction to Analytical Electron Microscopy, eds. Hren, JJ, Goldstein, JI, Joy, DC, 1987 Plenum Press (New York)

Holm, MS, Saravanamurugan, S, Taarning, E, *Science*, **328**, 'Conversion of sugars to lactic acid derivatives using heterogeneous zeotype catalysts', 2010, 602-605

Hooley, R, Brown, A, Brydson, R, *Micron*, **120**, 'Factors affecting electron beam damage of calcite nanoparticles', 2019, 25-34

Iwashita, N, 'Chapter 2 – X-ray Powder Diffraction', in: Inagaki, M, ed, 'Materials Science and Engineering of Carbon', 2016, Butterworth-Heinemann – Oxford

Jensen, G, 'Methods in Enzymology – Volume 481 – Cryo-EM, Part A – Sample Preparation and Data Collection', 2010, Elsevier (San Diego)

Jones, W, 'Interaction of high-energy electrons with organic crystals in the electron microscope: Difficulties associated with the study of defects', in: Roberts, MW, Thomas, JM, eds, 'Surface and Defect Properties of Solids: Volume 5', 1976, Royal

Society of Chemistry (London)

Jones, W, Thomas, JM, *Progress in Solid State Chemistry*, **12** (2), 'Applications of electron microscopy to organic solid-state chemistry', 1979, 101-124

Josephson, TR, Jenness, GR, Vlachos, DG, Caratzoulas, S, *Microporous and Mesoporous Materials*, **245**, 'Distribution of open sites in Sn-beta zeolite', 2017, 45-50

Khamar, D, Pritchard, RG, Bradshaw, IJ, Hutcheon, GA, Seton, L, *Acta Crystallographica*, **61** (12), 'Polymorphs of anhydrous theophylline: stable form IV consists of dimer pairs and metastable form I consists of hydrogen-bonded chains', 2011, o496-o499

Kobayashi, T, Fujiyoshi, Y, Uyeda, N, *Acta Crystallographica*, **38**, 'The Observation in Crystal Defects and the Growth Mechanism of Thin Phthalocyanine Films', 1982, 356-362

Kobayashi, T, Isoda, S, *Journal of Materials Chemistry*, **3**, 'Lattice Images and Molecular Images of Organic Materials', 1993, 1-14

Koehler, JS, Physical Review, **181** (3), 'Diffusion of lattice defects in a stress field', 1969, 1015-1019

Kolyagin, YG, Yakimov, AV, Tolborg, S, Vennestrøm, PNR, Ivanova, II, *The Journal of Physical Chemistry Letters*, **9**, 'Direct Observation of Tin in Different T-Sites of Sn-BEA by One- and Two-Dimensional ^{119}Sn MAS NMR Spectroscopy', 2018, 3738-3743

Kossel, A, *Berichte der Deutschen Chemischen Gesellschaft*, **21**, 'Ueber eine neue Base aus dem Pflanzenreich', 1888, 2164-2167

Kumar, MNVR, *Reactive and Functional Polymers*, **46**, 'A Review of Chitin and Chitosan Applications', 2000, 1-27

Kuo, AIM, Glaeser, RM, *Ultramicroscopy*, **1** (1), Development of methodology for low exposure, high-resolution electron microscopy of biological specimens', 1975, 53-66

Lazić, I, Bosch, EGT, Lazar, S, *Ultramicroscopy*, **160**, 'Phase contrast STEM for thin samples: Integrated differential phase contrast', 2016, 265-280

Lewis, IR, Edwards, HGM eds., 'Handbook of Raman Spectroscopy', 2001, Marcel Dekker, Inc. (New York)

MacLaren, I, Nord, M, Ross, A, Krajnak, M, Hart, M, Doye, A, McGrouther, D, Bali, R, Banerjee, A, Hadfield, R, *European Microscopy Congress 2016: Proceedings*, 'Pixelated STEM detectors: opportunities and challenges', 2016, 663-664

Mayoral, A, Anderson, PA, Diaz, I, *Micron*, **68**, 'Zeolites are no Longer a Challenge: Atomic Resolution Data by Aberration-Corrected STEM', 2015, 146-151

Menter, JW, *Proceedings of the Royal Society of London. Series A, Mathematical and Physical Sciences*, **236**, 'The direct study by electron microscopy of crystal lattices and their imperfections', 1956

Moliner, M, Román-Leshkov, Y, Davis, ME, *Proceedings of the National Academy of Sciences of the United States of America*, **107** (14), 'Tin-containing zeolites are highly active catalysts for the isomerization of glucose in water', 2010, 6164-6168

Momma, K, VESTA modelling software - http://jp-minerals.org/vesta/en/ [Last accessed: 20/09/2019]

Murata, Y, Fryer, JR, Baird, T, *Journal of Microscopy*, **108** (3), 'Molecular imaging of copper phthalocyanine', 1976, 261-275

Newsam, JM, Treacy, MMJ, Koetsier, WT, de Gruyter, CB, *Proceedings of the Royal Society of London A*, **420**, 'Structural characterization of beta zeolite', 1988, 375-405

Ni, ZH, Yu, T, Lu, YH, Wang, YY, Fang, YP, Shen, ZX, *ACSNano*, **2**, 'Uniaxial Strain on Graphene: Raman Spectroscopy Study and Band-Gap Opening', 2008, 2301-2305,

O'Brien, LE, Timmins, P, Williams, AC, York, P, *Journal of Pharmaceuticals and Biomedical Analysis*, **36**, 'Use of in situ FT-Raman Spectroscopy to Study the Kinetics of the Transformation of Carbamazepine Polymorphs', 2004, 335-340

Palmer, DC & Palmer, SE, CrystalMaker modelling software - http://crystalmaker.com/ [Last accessed: 20/09/2019]

Phadnis, N V & Suryanarayanan, R, *Journal of Pharmaceutical Sciences*, **86**, 'Polymorphism in anhydrous theophylline - Implications on the dissolution rate of

theophylline tablets', 1997, 1256-1263

Phifer, D, Tuma, L, Vystavel, T, Wandrol, P, Young, RJ, *Microscopy Today*, **17** (4), 'Improving SEM Imaging Performance Using Beam Deceleration', 2009, 40-49

Reimer, L, 'Scanning Electron Microscopy: Physics of Image Formation and Microanalysis', eds. Hawkes, PW, Enoch, JM, Schawlow, AL, Shimoda, K, MacAdam, DL, Tamir, T, 2013, Springer – Verlag (Berlin)

Reimer, L, Golla, U, Boeneger, R, Kaessens, M, Schindler, B, Senkel, R, *Optik*, **92**, 'Charging of Bulk Specimens, Insulating Layers and Free-Supporting Films in Scanning Electron Microscopy', 1992, 14-22

Revol, JF, St John Manley, R, *Journal of Materials Science Letters*, **5**, 'Lattice imaging in polyethylene single crystals', 1986, 249-251

Ricarte, RG, Lodge, TP, Hillmyer, MA, *Molecular Pharmaceuticals*, **12**, 'Detection of pharmaceutical drug crystallites in solid dispersion by transmission electron microscopy', 2015, 983-990

Rose, H, *Optik*, **39** (4), 'Phase contrast in scanning transmission electron microscopy', 1974, 416-436

Roy, C, Vega-Gonzalez, A, Subra-Paternault, P, *International Journal of Pharmaceuticals*, **343**, 'Theophylline formulation by supercritical antisolvents', 2007, 79-89

S'ari, M, Blade, H, Brydson, R, Cosgrove, SD, Hondow, N, Hughes, LP, Brown, A, *Molecular Pharmaceutics*, **15** (11), 'Toward Developing a Predictive Approach To Assess Electron Beam Instability during Transmission Electron Microscopy of Drug Molecules', 2018, 5114-5123

S'ari, M, Cattle, J, Hondow, N, Blade, H, Cosgrove, S, Brydson, RM, Brown, AP, *Journal of Physics: Conference Series*, **644**, 'Analysis of electron beam damage of crystalline pharmaceutical materials by transmission electron microscopy', 2015, 1-5

S'ari, M, Cattle, J, Hondow, N, Brydson, R, Brown, A, *Micron*, **120**, 'Low dose scanning transmission electron microscopy of organic crystal scanning moiré fringes', 2019, 1-9

Sader, K, Brown, A, Brydson, R, Bleloch, A, *Ultramicroscopy*, **110** (10), 'Quantitative analysis of image contrast STEM for low dose imaging', 2010, 1324-1331

Sagawa, R, Hashiguchi, H, Isabell, T, Ritz, R, Simson, M, Huth, M, Soltau, H, Martinez, GT, Nellist, PD, Kondo, Y, *Microscopy and Microanalysis*, **24**, 'Low Dose Imaging by STEM Ptychography Using Pixelated STEM Detector', 2018

Schenk, H, Peschar, R, *Radiation Physics and Chemistry*, **71**, 'Understanding the Structure of Chocolate', 2004, 829-835

Schultheiss, N, Newman, A, *Crystal Growth & Design*, **16**, 'Pharmaceutical in Cocrystals: A Review and Assessment of its Significance', 2009, 2950-2967

Schultze-Werninghaus, G, Meier-Sydow, J, *Clinical Allergy*, **12**, 'The Clinical and Pharmacological History of Theophylline: First Report on Bronchospasmolytic Action in Man by S. R. Hirsch in Frankfurt (Main) 1922', 1982, 211-215

Seton, L, Khamar, D, Bradshaw, IJ, Hutcheon, GA, *Crystal Growth & Design*, **10**, 'Solid State Forms of Theophylline: Presenting a New Anhydrous Polymorph', 2010, 3879-3886

Shetty, S, Pal, S, Kanhere, DG, Gourshot, A, *Chemistry – A European Journal*, **12** (2), 'Structural, Electronic, and Bonding Properties of Zeolite Sn-Beta: A Periodic Density Functional Theory Study', 2005, 518-523

Smith, DJ, Fryer, JR, *Nature*, **291**, 'Molecular detail in electron micrographs of quaterrylene $C_{40}H_{20}$', 1981, 481-482

Stenn, K and Bahr, GF, *Journal of Ultrastructure Research*, **31** (5-6), 'Specimen damage caused by the beam of the transmission electron microscope, a correlative reconsideration', 1970, 526-550

Stevens, A, Luzi, L, Yang, H, Kovarik, L, Mehdi, BL, Liyu, A, Gehm, ME, Browning, ND, *Applied Physics Letters*, **112**, 'A sub-sampled approach to extremely low-dose STEM', 2018, 043104

Su, D, Zhu, Y, *Ultramicroscopy*, **110** (3), 'Scanning moiré fringe imaging by scanning transmission electron microscopy', 2010, 229-233

Suzuki, E, Shimomura, K, Sekiguchi, K, *Chemical and Pharmaceutical Bulletin*, **37**, 'Thermochemical Study of Theophylline and its Hydrate', 1989, 493-497

Taylor, KA, Glaeser, RM, *Journal of Ultrastructure Research*, **55**, 'Electron Diffraction of Frozen, Hydrated Biological Specimens', 1976, 448-456

Taylor, KA, Glaeser, RM, *Science*, **186**, 'Electron Diffraction of Frozen, Hydrated Protein Crystals', 1974, 1036-1037

Tolborg, S, Katerinopoulou, A, Falcone, DD, Sádaba, I, Osmundsen, CM, Davis, RJ, Taarning, E, Fristrup, P, Holm, MS, *Journal of Materials Chemistry A*, **2**, 'Incorporation of tin affects crystallization, morphology, and crystal composition of Sn-beta', 2014, 20252-20262

Tolborg, S, Sádaba, I, Osmundsen, CM, Fristrup, P, Holm, MS, Taarning, E, *ChemSusChem*, **8** (4), 'Tin-containing silicates: alkali salts improve methyl lactate yield from sugars', 2015, 613-617

Treacy, MMJ, Newsam, JM, *Ultramicroscopy*, **23** (3-4), 'Electron beam sensitivity of zeolite L', 1987, 411-419

Ugurlu, O, Haus, J, Gunawan, AA, Thomas, MG, Maheshwari, S, Tsaptasis, M, Mkhoyan, KM, *Physical Review B*, **83**, 'Radiolysis to Knock-On damage Transition in Zeolites Under Electron Beam Irradiation', 2011, 113408

Unwin, PNT, Henderson, R, *Journal of Molecular Biology*, **94**, 'Molecular Structure Determination by Electron Microscopy of Unstained Crystalline Specimens', 1975, 425-440

Van Genderen , E, Clabbers, MTB, Das, PP, Stewart, A, Nederlof, I, Barentsen, KC, Portillo, Q, Pannu, NS, Nicolopoulos, S, Gruene, T, Abrahams, JP, *Acta Crystallographica*, **72**, 'Ab initio structure determination of nanocrystals of organic pharmaceutical compounds by electron diffraction at room temperature using a Timepix quantum area direct electron detector', 2016, 236-242

Vippagunta, SR, Brittain, HG, Grant, DJW, *Advanced Drug Delivery Reviews*, **48**, 'Crystalline Solids', 2001, 3-26

Wadlinger, RL, Kerr, GT, Rosinski, EJ, US Patent No. 3308069 (assigned to Mobil Oil Corporation), 1967

Wang, C, Qiao, Q, Shokuhfar, T, Klie RF, *Advanced Materials*, **26**, 'High-resolution electron microscopy and spectroscopy of ferritin in biocompatible graphene liquid cells and graphene sandwiches', 2014, 3410-3414

Wang, SX, Wang, LM, Ewing, RC, *Journal of Nuclear Materials*, **278**, 'Electron and ion irradiation of zeolites', 2000, 233-241

Williams, DB, Carter, CB, **2nd Edition** 'Transmission Electron Microscopy: A Textbook for Materials Science', 2009, Springer – Verlag (Berlin)

Wilson, NR, Pandey, PA, Beanland, R, Young, RJ, Kinloch, IA, Gong, L, Liu, Z, Suenaga, K, Rourke, JP, York, SJ, Sloan, J, *ACS Nano*, **3** (9), 'Graphene oxide: Structural analysis and application as a highly transparent support for electron microscopy', 2009, 2547-2556

Yang, G, Pidko, EA, Hensen, EJM, *Journal of Physical Chemistry C*, **117** (8), Structure, Stability, and Lewis Acidity of Mono and Double Ti, Zr, and Sn Framework Substitutions in BEA Zeolites: A Periodic Density Functional Theory Study', 2013, 3976-3986

Zan, M, Ramasse, QM, Jalil, R, Georgiou, T, Bangert, U, Novoselov, KS, *ACS Nano*, **7** (11), 'Control of Radiation Damage in MoS2 by Graphene Encapsulation', 2013, 10167-10174

Zemlin, F, Reuber, E, Beckmann, E, Zeitler, E, Dorset, DL, *Science*, **229**, 'Molecular resolution electron micrographs of monolamellar paraffin crystals', 1985, 461-462

Zhang, D, Zhu, Y, Liu, L, Ying, X, Hsiung, CE, Sougrat, R, Li, K, Han, Y, *Science*, **359**, 'Atomic-resolution transmission electron microscopy of electron beam-sensitive crystalline materials', 2018, 675-679

Appendix A – Lattice Spacings of Stable Anhydrous Theophylline Polymorphs

Theophylline Form I Reflexions		3 4 1	2.326	3 8 0	1.785
h k l	d-spacing	2 5 1	2.278	5 5 1	1.784
1 1 0	10.066	4 5 0	2.266	7 3 0	1.768
0 2 0	7.815	4 3 1	2.255	3 7 1	1.768
1 2 0	6.719	3 6 0	2.240	3 1 2	1.753
2 0 0	6.579	1 7 0	2.201	2 3 2	1.743
2 1 0	6.064	6 0 0	2.193	0 4 2	1.728
2 2 0	5.033	5 4 0	2.183	1 8 1	1.728
1 3 0	4.844	6 1 0	2.172	1 9 0	1.722
3 1 0	4.223	5 1 1	2.153	3 2 2	1.721
2 3 0	4.084	1 6 1	2.130	1 4 2	1.714
0 4 0	3.908	3 5 1	2.124	6 4 1	1.713
3 2 0	3.825	2 7 0	2.114	5 7 0	1.703
1 4 0	3.746	6 2 0	2.111	7 4 0	1.694
0 1 1	3.742	4 4 1	2.107	2 8 1	1.685
1 1 1	3.599	5 2 1	2.094	4 8 0	1.680
2 4 0	3.360	2 6 1	2.051	7 1 1	1.680
3 3 0	3.355	4 6 0	2.042	2 9 0	1.679
1 2 1	3.343	6 3 0	2.021	6 6 0	1.678
2 0 1	3.325	5 5 0	2.013	2 4 2	1.672
4 0 0	3.290	5 3 1	2.006	3 3 2	1.671
2 1 1	3.253	3 7 0	1.990	5 6 1	1.669
4 1 0	3.219	0 8 0	1.954	4 7 1	1.666
0 3 1	3.098	4 5 1	1.953	4 0 2	1.663
2 2 1	3.060	3 6 1	1.936	4 1 2	1.653
1 5 0	3.041	1 8 0	1.933	7 2 1	1.651
4 2 0	3.032	0 7 1	1.932	8 0 0	1.645
1 3 1	3.016	0 0 2	1.927	8 1 0	1.636
3 4 0	2.918	6 4 0	1.912	1 5 2	1.628
3 1 1	2.847	1 7 1	1.912	6 5 1	1.627
2 5 0	2.823	6 0 1	1.906	4 2 2	1.626
2 3 1	2.803	5 4 1	1.899	3 8 1	1.619
4 3 0	2.781	1 1 2	1.893	3 9 0	1.615
3 2 1	2.715	6 1 1	1.892	7 5 0	1.611
1 4 1	2.686	2 8 0	1.873	8 2 0	1.609
0 6 0	2.605	0 2 2	1.871	3 4 2	1.608
5 1 0	2.595	7 1 0	1.866	7 3 1	1.607
1 6 0	2.555	2 7 1	1.854	2 5 2	1.592
3 5 0	2.546	1 2 2	1.852	4 3 2	1.584
2 4 1	2.532	6 2 1	1.852	0 9 1	1.583
3 3 1	2.531	5 6 0	1.851	1 9 1	1.572
4 4 0	2.517	2 0 2	1.849	5 8 0	1.569
4 0 1	2.502	4 7 0	1.847	8 3 0	1.568
5 2 0	2.494	2 1 2	1.837	6 7 0	1.565
4 1 1	2.471	7 2 0	1.828	0 10 0	1.563
0 5 1	2.428	4 6 1	1.805	5 7 1	1.557
2 6 0	2.422	2 2 2	1.800	1 10 0	1.552
1 5 1	2.387	6 5 0	1.795	7 4 1	1.551
4 2 1	2.383	1 3 2	1.791	0 6 2	1.549
5 3 0	2.349	6 3 1	1.790	5 1 2	1.547

Appendix 5.1: The first 148 lattice spacing measurements for anhydrous theophylline form I and their corresponding Miller indices.

Theophylline Form II Reflexions		h k l	d-spacing	h k l	d-spacing
h k l	d-spacing	0 0 4	2.121	6 1 4	1.682
2 0 0	12.165	4 1 3	2.121	2 0 5	1.681
2 0 1	6.959	10 0 2	2.111	13 1 0	1.676
4 0 0	6.083	2 0 4	2.090	6 2 1	1.676
4 0 1	4.944	8 0 3	2.071	4 2 2	1.658
0 0 2	4.243	8 1 2	2.067	7 2 0	1.657
6 0 0	4.055	5 1 3	2.052	10 1 3	1.657
2 0 2	4.006	10 1 0	2.044	12 0 3	1.648
1 1 0	3.726	12 0 0	2.028	12 1 2	1.646
6 0 1	3.659	4 0 4	2.003	13 1 1	1.645
2 1 0	3.602	10 1 1	1.988	4 0 5	1.635
4 0 2	3.480	6 1 3	1.976	7 1 4	1.632
0 1 1	3.446	12 0 1	1.972	7 2 1	1.627
3 1 0	3.419	9 1 2	1.951	5 2 2	1.624
1 1 1	3.412	11 1 0	1.908	14 0 2	1.608
2 1 1	3.315	7 1 3	1.896	8 2 0	1.602
4 1 0	3.205	0 2 0	1.885	10 0 4	1.599
3 1 1	3.171	1 2 0	1.880	6 2 2	1.586
8 0 0	3.041	6 0 4	1.880	11 1 3	1.582
4 1 1	2.998	2 2 0	1.863	8 1 4	1.580
5 1 0	2.981	11 1 1	1.861	14 1 0	1.578
6 0 2	2.931	10 0 3	1.844	8 2 1	1.575
8 0 1	2.863	1 1 4	1.843	1 2 3	1.566
5 1 1	2.812	10 1 2	1.842	6 0 5	1.565
1 1 2	2.800	3 2 0	1.836	13 1 2	1.559
6 1 0	2.761	1 2 1	1.835	2 2 3	1.556
2 0 3	2.755	12 0 2	1.829	14 1 1	1.552
2 1 2	2.746	2 1 4	1.828	0 1 5	1.548
3 1 2	2.662	2 2 1	1.820	9 2 0	1.546
6 1 1	2.626	8 1 3	1.815	1 1 5	1.544
4 0 3	2.565	3 1 4	1.803	7 2 2	1.544
4 1 2	2.557	4 2 0	1.801	3 2 3	1.540
7 1 0	2.556	3 2 1	1.795	2 1 5	1.535
8 0 2	2.472	12 1 0	1.786	9 1 4	1.526
7 1 1	2.447	4 1 4	1.769	9 2 1	1.521
5 1 2	2.439	4 2 1	1.762	16 0 0	1.521
10 0 0	2.433	5 2 0	1.758	3 1 5	1.520
8 1 0	2.367	12 1 1	1.747	4 2 3	1.519
10 0 1	2.339	11 1 2	1.740	12 1 3	1.510
6 0 3	2.320	8 0 4	1.740	4 1 5	1.500
6 1 2	2.314	14 0 0	1.738	8 2 2	1.499
8 1 1	2.280	9 1 3	1.735	16 0 1	1.497
0 1 3	2.263	5 1 4	1.728	5 2 3	1.493
1 1 3	2.253	0 2 2	1.723	10 2 0	1.490
2 1 3	2.224	5 2 1	1.721	15 1 0	1.490
9 1 0	2.197	1 2 2	1.719	8 0 5	1.482
7 1 2	2.189	6 2 0	1.710	14 0 3	1.481
3 1 3	2.179	2 2 2	1.706	14 1 2	1.479
9 1 1	2.127	14 0 1	1.703	5 1 5	1.475
		3 2 2	1.685	10 1 4	1.472

Appendix 5.2: The first 148 lattice spacing measurements for anhydrous theophylline form II and their corresponding Miller indices.

h	k	l	d-spacing	h	k	l	d-spacing	h	k	l	d-spacing
Theophylline Form IV Reflexions				-2	2	2	3.230	0	3	5	2.506
h	k	l	d-spacing	1	3	2	3.229	3	0	0	2.500
0	1	1	9.924	-1	3	3	3.207	-2	3	4	2.497
0	0	2	7.680	0	4	1	3.180	-2	2	5	2.492
1	0	0	7.501	1	0	4	3.139	-2	4	1	2.484
0	1	2	6.613	2	0	2	3.102	0	4	4	2.481
0	2	0	6.501	2	2	1	3.058	1	4	3	2.481
1	1	0	6.497	2	0	-4	3.055	-1	4	4	2.467
-1	1	1	6.461	1	1	4	3.052	0	5	2	2.463
1	0	-2	6.110	-2	2	3	3.028	1	5	0	2.457
0	2	1	5.987	-1	1	5	3.018	2	4	0	2.456
1	1	1	5.599	2	1	2	3.017	3	1	0	2.455
-1	1	2	5.530	0	4	2	2.993	-1	5	1	2.455
0	2	2	4.962	0	1	5	2.990	-2	4	2	2.448
1	2	0	4.913	1	4	0	2.982	1	2	5	2.445
-1	2	1	4.897	-1	4	1	2.979	-3	1	3	2.438
1	0	2	4.841	-2	1	4	2.974	-1	2	6	2.424
0	1	3	4.764	-2	3	1	2.879	2	0	4	2.421
1	1	2	4.537	1	4	1	2.879	1	5	1	2.398
1	2	1	4.488	0	3	4	2.874	-1	5	2	2.393
-1	1	3	4.476	1	3	3	2.874	-3	2	1	2.384
-1	2	2	4.452	-1	4	2	2.870	2	0	-6	2.384
0	3	1	4.171	-1	3	4	2.852	0	2	6	2.382
0	2	3	4.022	2	3	0	2.836	2	1	4	2.380
1	2	2	3.883	1	2	4	2.827	-3	2	2	2.379
-1	2	3	3.844	-2	3	2	2.824	2	4	1	2.371
0	0	4	3.840	-1	2	5	2.800	-2	4	3	2.357
1	0	-4	3.788	2	2	2	2.800	3	0	-4	2.356
0	3	2	3.774	0	2	5	2.778	-2	1	6	2.345
1	3	0	3.752	-2	2	4	2.765	3	1	1	2.344
2	0	0	3.751	0	4	3	2.744	3	2	0	2.334
-1	3	1	3.745	2	3	1	2.707	-3	2	3	2.319
2	0	-2	3.723	1	4	2	2.699	-3	1	4	2.319
-2	1	1	3.694	-2	3	3	2.686	0	5	3	2.318
0	1	4	3.683	-1	4	3	2.685	2	3	3	2.317
1	1	3	3.682	2	1	3	2.682	1	5	2	2.291
-1	1	4	3.637	-2	1	5	2.642	-2	3	5	2.291
2	1	0	3.604	1	0	-6	2.613	-1	5	3	2.283
-2	1	2	3.579	1	1	5	2.586	1	0	6	2.269
1	3	1	3.553	0	5	1	2.564	2	2	4	2.268
-1	3	2	3.535	-1	1	6	2.561	1	4	4	2.258
2	1	1	3.349	0	0	6	2.560	1	3	5	2.254
-2	2	1	3.314	3	0	-2	2.556	-1	4	5	2.244
-2	1	3	3.309	1	3	4	2.542	2	4	2	2.244
0	3	3	3.308	2	2	3	2.526	-2	2	6	2.238
0	2	4	3.306	-1	3	5	2.523	-1	3	6	2.237
1	2	3	3.306	2	3	2	2.522	3	2	1	2.237
-1	2	4	3.273	-3	1	1	2.514	1	1	6	2.236
0	4	0	3.250	0	1	6	2.512	0	4	5	2.233
2	2	0	3.249	-3	1	2	2.508	3	0	2	2.232

Appendix 5.3: The first 148 lattice spacing measurements for anhydrous theophylline form IV and their corresponding Miller indices.

Theophylline Form M Reflexions			1 3 1	3.151	4 3 -1	2.504
h	k	l	d-spacing	1 -3 1	3.151	1 6 0	2.503
1	0	0	13.118	2 3 -1	3.145	4 4 0	2.490
1	1	0	9.959	-2 3 1	3.145	5 2 0	2.482
0	2	0	7.650	2 2 1	3.124	4 0 1	2.451
1	2	0	6.608	2 -2 1	3.124	5 0 -1	2.442
2	0	0	6.559	-3 2 1	3.114	1 5 1	2.432
2	1	0	6.028	3 2 -1	3.114	1 -5 1	2.432
2	2	0	4.979	4 2 0	3.014	-2 5 1	2.429
1	3	0	4.753	1 5 0	2.980	2 5 -1	2.429
0	0	1	4.438	0 4 1	2.897	4 -1 1	2.420
1	0	-1	4.432	0 4 -1	2.897	4 1 1	2.420
3	0	0	4.373	-1 4 1	2.896	5 1 -1	2.411
0	1	-1	4.263	1 4 -1	2.896	-5 1 1	2.411
0	1	1	4.263	3 0 1	2.886	2 6 0	2.377
1	1	-1	4.257	3 4 0	2.879	4 2 1	2.334
-1	1	1	4.257	4 0 -1	2.874	4 -2 1	2.334
3	1	0	4.204	2 3 1	2.842	5 3 0	2.333
2	3	0	4.026	2 -3 1	2.842	5 2 -1	2.326
1	0	1	4.008	3 1 1	2.836	-5 2 1	2.326
2	0	-1	3.995	3 -1 1	2.836	3 4 1	2.304
1	1	1	3.877	3 3 -1	2.834	3 -4 1	2.304
1	-1	1	3.877	-3 3 1	2.834	-4 4 1	2.298
-2	1	1	3.865	4 1 -1	2.825	4 4 -1	2.298
2	1	-1	3.865	-4 1 1	2.825	2 5 1	2.281
0	2	1	3.839	2 5 0	2.773	2 -5 1	2.281
0	2	-1	3.839	1 4 1	2.767	-3 5 1	2.277
-1	2	1	3.835	1 -4 1	2.767	3 5 -1	2.277
1	2	-1	3.835	-2 4 1	2.763	1 0 -2	2.250
0	4	0	3.825	2 4 -1	2.763	4 5 0	2.237
3	2	0	3.796	4 3 0	2.758	1 1 -2	2.226
1	4	0	3.672	3 2 1	2.700	-1 1 2	2.226
1	2	1	3.550	3 -2 1	2.700	0 0 2	2.219
1	-2	1	3.550	-4 2 1	2.690	2 0 -2	2.216
-2	2	1	3.541	4 2 -1	2.690	0 6 1	2.211
2	2	-1	3.541	5 0 0	2.624	0 6 -1	2.211
2	0	1	3.423	5 1 0	2.586	-1 6 1	2.210
3	0	-1	3.409	2 4 1	2.551	1 6 -1	2.210
0	3	1	3.348	2 -4 1	2.551	4 3 1	2.209
0	3	-1	3.348	0 6 0	2.550	4 -3 1	2.209
-1	3	1	3.345	3 4 -1	2.545	3 6 0	2.203
1	3	-1	3.345	-3 4 1	2.545	-5 3 1	2.202
2	1	1	3.340	0 5 -1	2.519	5 3 -1	2.202
2	-1	1	3.340	0 5 1	2.519	0 1 -2	2.196
-3	1	1	3.327	-1 5 1	2.518	0 1 2	2.196
3	1	-1	3.327	1 5 -1	2.518	-2 1 2	2.193
3	3	0	3.320	3 3 1	2.512	2 1 -2	2.193
2	4	0	3.304	3 -3 1	2.512	6 0 0	2.186
4	0	0	3.279	3 5 0	2.507	6 1 0	2.164
4	1	0	3.207	-4 3 1	2.504	5 4 0	2.164

Appendix 5.4: The first 148 lattice spacings measurements for anhydrous theophylline form IV and their corresponding Miller indices.